An *in vivo* MRI and *post-mortem* qIHC study of an APP mouse model

Marilyn Grand'Maison

Department of Neurology and Neurosurgery
McGill University, Montreal
Initial submission: December 2012
Final submission: April 2013

A thesis submitted to McGill University in partial fulfillment of the requirements of the degree of Master in Science

Table of Contents

1. Abstract

This thesis presents studies of the intricate relationship between macroscopic and microscopic changes, respectively measured by magnetic resonance imaging and quantitative immunohistochemistry, underpinning the pathological processes in a well-defined Alzheimer's disease (AD) transgenic (Tg) mouse model. First, we explored the spatio-temporal differences in cortical thickness and perfusion in Tg and wild-type (WT) mice. Then, we interrogated the association between early cortical thickness alterations and amyloid deposition at old age. Finally, we utilized a novel, 3D whole brain *in vivo* MRI acquisition technique to assess the pattern of arterial dysfunction in our AD mouse model.

We determined that there was a heterogeneous spatio-temporal pattern of cortical thickness and perfusion changes in Tg mice. In addition, we identified that the aberrant cortical thickness pattern in early life predicted subsequent regional plaque deposition. Finally, we observed significant regional dysfunction in the arterial vasculature in Tg mice.

2. Résumé

Cette thèse présente l'étude de la relation complexe entre les changements d'échelle macroscopique et microscopique, mesurés respectivement par imagerie par résonnance magnétique et immunohistochimie quantitative, dictant le processus pathologique d'un modèle transgénique (Tg) murin bien caractérisé de la maladie d'Alzheimer. Premièrement, nous avons examiné les différences spatiotemporelles d'épaisseur et de perfusion corticale dans des souris Tg et wild-type (WT). Ensuite, nous avons investigué l'association entre les altérations précoces d'épaisseur corticale et la déposition tardive de plaques amyloïdes. Finalement, nous avons utilisé une technique innovatrice d'acquisition 3D du cerveau complet par imagerie par résonance magnétique pour évaluer l'ampleur de la dysfonction artérielle dans notre modèle murin d'Alzheimer.

Nous avons déterminé que les changements spatiotemporels d'épaisseur et de perfusion corticale étaient hétérogènes dans les souris transgéniques. De plus, nous avons identifié que les changements aberrants d'épaisseur corticale en jeune âge annonçaient la déposition ultérieure de plaques. Finalement, nous avons observé une dysfonction vasculaire significative au niveau artériel des souris transgéniques.

3. Acknowledgements

First, I would like to warmly thank my supervisor, Dr. Barry Bedell, for the great opportunities he offered me, his insightful advices and recommendations, his pedagogic guidance, and his financial support. I would also like to thank my committee, Drs. Alan Evans and Andrea Leblanc, for their meaningful comments and recommendations.

This project involved multi-disciplinary techniques, and I received kind and patient training from several people. I would like to thank Ming-Kai Ho for assistance in carrying out experiments, Rozika Bolovan and Qin Shao for their contribution to the immunohistochemistry data, Kung Yuan Lin and Antonio Aliaga for MRI scanning, Josée Bergeron for helpful discussions, and Edith Hamel for providing the animals. I would like to thank François Hébert, Simone Zehntner, Katherine Leonard, Alex Zijdenbos, and Arnaud Charil for training with the MINC tools and data processing. I would also like to thank Felix Carbonell for assistance with statistical analysis. I would like to thank Angie Giannokopoulos and Tom Hein for administrative assistance.

Importantly, I would like to thank my family and friends. Thank you all for your moral support, endless encouragement, and thoughtful discussions.

4. List of Abbreviations

Aβ	β-amyloid
AD	Alzheimer's disease
AICP	APP-intracellular domain
APOE	Apolipoprotein E
APP	Amyloid precursor protein
ASL	Arterial spin labeling
Au	Austrian
CAA	Cerebral amyloid angiopathy
CBF	Cerebral blood flow
CBV	Cerebral blood volume
CE	Contrast-enhanced
CSF	Cerebrospinal fluid
CTF	C-terminal fragment
DBM	Deformation-based morphometry
DMN	Default mode network
EC	Extracellular domain
FDG	2-[^{18}F]fluoro-2-deoxy-D-glucose
FTD	Frontotemporal dementia
IC	Intracellular domain
Ind	Indiana
ISF	Interstitial fluid
LDF	Laser Doppler flowmetry
MCA	Middle cerebral artery
MCI	Mild cognitive impairment
MRA	Magnetic resonance angiography
MRI	Magnetic resonance imaging
NFT	Neurofibrillary tangle
PCA	Posterior cerebral artery
PD	Proton density
PET	Positron emission tomography
PS	Presenilin
PVE	Partial volume effect
qIHC	quantitative immunohistochemistry
RF	Radiofrequency
ROI	Region-of-interest
SNR	Signal-to-noise ratio
SOD2	Manganese superoxide dismutase
Sw	Swedish
Tg	Transgenic
TM	Transmembrane domain
WT	Wild-type

5. Introduction

Magnetic resonance imaging (MRI) is a non-invasive modality for the investigation of structural and functional changes. Over the past several years, structural MRI has been widely used to study brain alterations in AD. Structural MRI biomarkers, such as cortical thickness and hippocampal volume, allow for the monitoring of patterns of disease progression (Lin et al., 2012).

Assessment of cerebral blood flow (CBF) provides essential information related to the impaired hemodynamic function observed in AD. Regional cerebral hypoperfusion and dysfunction have been widely reported in AD patients (Farkas and Luiten, 2001). Brain hypoperfusion can be detected by arterial spin labeling (ASL) MRI. Moreover, the pattern of CBF deficits is predictive of cognitive decline and has been proposed to identify predisposition for AD (Chao et al., 2010).

Interestingly, disease progression appears to follow the default mode network (DMN). The DMN includes the dorsal and ventral medial prefrontal cortices, the medial and lateral parietal cortices, and some parts of the medial and lateral temporal cortices. DMN activity is downregulated when the brain is engaged in an externally-directed task, and is activated when the brain is not involved in a cognitively demanding task, *e.g.* memory encoding, orientation, and external stimulus processing, which are functions affected in AD. As such, the DMN has become an area of focus in AD research. At the early AD stage, some territories related to the DMN, specifically the medial temporal cortex, including the amygdala, the anterior hippocampus, and the entorhinal cortex, show structural changes and functional anomalies (Shin et al., 2011). Later, the abnormalities progress to the middle temporal gyrus, the entire hippocampus, and, the posterior parietal cortex (Shin et al., 2011).

AD is marked by characteristic neuropathological changes. β-amyloid (Aβ) plaque deposition and the accumulation of hyperphosphorylated tau protein are the most extensively characterized molecular hallmarks of AD (Goate and Hardy, 2012). Since MRI is a translatable modality, AD Tg mouse models allow for comprehensive investigations of specific cellular aspects of the disease by allowing the coupling of temporally-matched imaging and pathological data. These mouse models recapitulate the amyloid plaque deposition, perfusion deficits, structural anomalies, and cognitive impairment observed in AD patients.

Clear evidence of cerebrovascular dysfunction and structural alterations exist in AD. However, the relationship between abnormal vascular function, structural changes, and the underlying AD-associated pathological events remains poorly understood. A primary focus of my thesis is to determine the biological substrates underpinning the structural and CBF changes observed in MRI data from an AD Tg mouse model.

6. Literature Review

6.1 Alzheimer's Disease

6.1.1 Epidemiology and Neuropathology

Dementia is defined by a gradual decline of cognitive abilities affecting social, occupational, and intellectual functioning. AD is the most common form of dementia affecting the elderly. It is characterized by a progressive decline of mental capacity, including memory loss and difficulty performing daily activities. Patients with AD develop language problems, are often disoriented and confused, and present decreased judgment. In addition to cognitive decline, behavioral and mood-related symptoms are common in AD (Lopez, 2011). Figure 6.1 shows the time course of the progressive loss of functions.

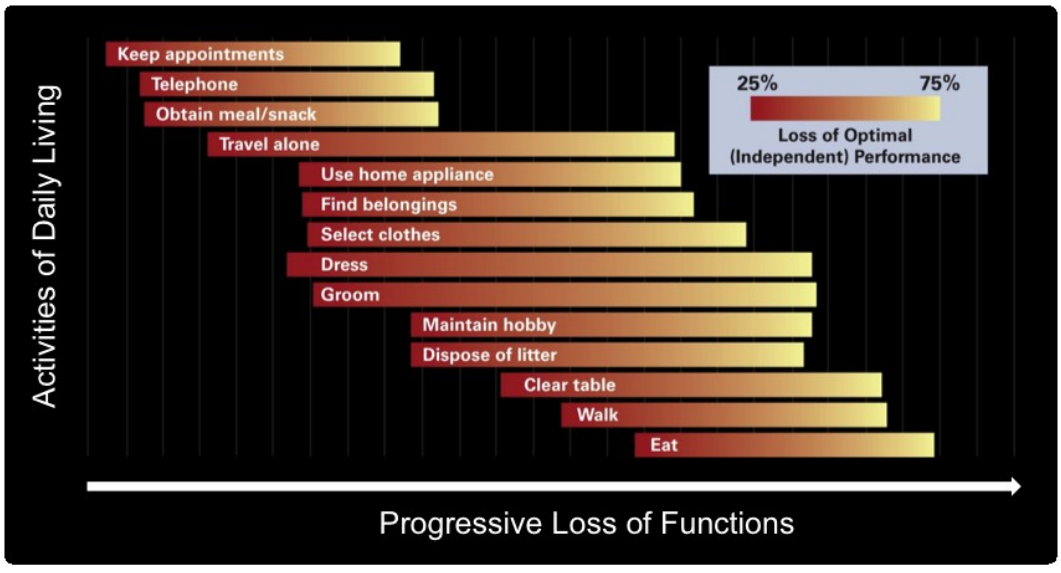

Figure 6.1 Progressive loss of functions related to AD cognitive decline. The color bar represents the extent of independent performance loss. Adapted from Lopez, *Am. J. Manag. Care,* 2011.

In 2010, about 35.6 million people worldwide were affected by AD and the cost of dementia was estimated at $604 billion. Unfortunately, the number of AD cases is expected to increase to 65.7 million by 2030, with an estimated 85% cost increase, reaching $1.1 trillion. More alarming, 115.4 million people are expected to suffer from AD in 2050, along with associated medical/care costs (Alzheimer's Disease International, 2010). The expected worldwide prevalence of AD subjects for the next 40 years is presented in Figure 6.2.

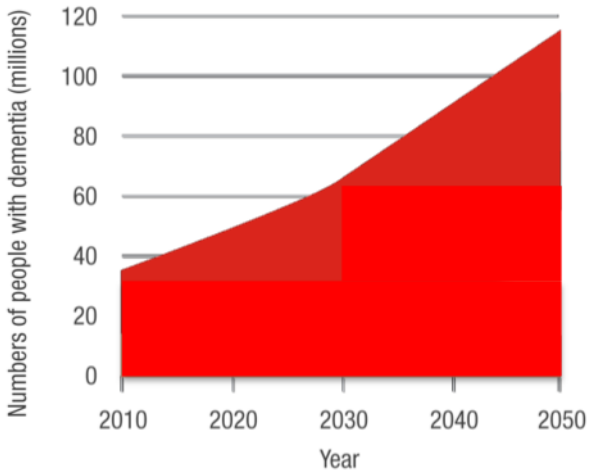

Figure 6.2 Expected prevalence of AD patients worldwide from 2010 to 2050. Adapted from World Alzheimer Report, *Alzheimer's Disease International,* 2010.

In Canada, approximately 500,000 people live with AD, and this number is expected to double in 20 years, thereby taxing an economic burden of $153 billion for dementia care. The incidence of new AD cases was estimated at 103,700 per year in 2008. In 2038, the projected incidence is expected to reach 257,800 new dementia cases per year (Alzheimer Society of Canada, 2010). Figure 6.3 shows the incidence and the prevalence predictions of AD cases for the next 20 years in Canada.

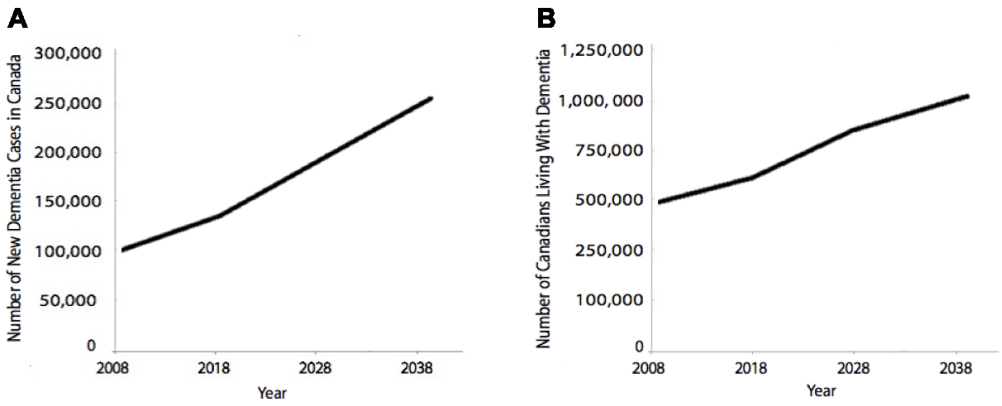

Figure 6.3 Expected number of new AD cases **(A)** and total number of AD patients **(B)** per year in Canada from 2008 to 2038. Adapted from Rising Tide: The impact of Dementia on Canadian Society, *Alzheimer Society of Canada,* 2010.

Aging is the most significant risk factor for AD. The predisposition for AD is relatively low under 65 years-old. However, after that age, the likelihood of developing dementia doubles every 5 years, reaching approximately 50% at 85 years-old (Lopez, 2011).

In addition, the presence of the apolipoprotein E (APOE) ε4 allele is a major genetic risk factor. Although the pathological mechanisms underlying this increased AD risk remain unknown, individuals carrying the APOE ε4 allele are more susceptible to develop AD (Kim et al., 2009). Other risk factors include family history of dementia, cerebrovascular diseases and associated risk factors (*e.g.* hypertension), head trauma, and female gender.

The diagnosis of AD is primarily made on a symptomatic basis, supported by clinical assessment of cognitive decline. However, definitive diagnosis can only be confirmed at autopsy. Furthermore, there is currently no effective pharmacological therapy to treat AD. Given that aging is the most important risk factor, there is an urgent need to untangle the pathological processes

underlying the AD clinical symptoms in order to accelerate the development of disease-modifying therapeutic agents.

6.1.2 Disease Mechanism

The etiology of AD remains indeterminate. However, neurodegenerative processes have been reported to start 20-30 years before noticeable signs of the pathology (Morris et al., 1996; Delacourte et al., 1999). As stated above, definitive AD diagnosis can currently only be made at autopsy based on the neuropathological hallmarks thought to be involved in the cellular disease mechanism. Amyloid peptide and tau protein aggregates are the major aberrations found in AD brains. Their postulated role in the disease progression at the cellular level is described below.

6.1.2.1 Amyloid Cascade Hypothesis

The amyloid cascade hypothesis posits that the central step leading to dementia is the deposition of Aβ peptides, leading to plaque formation in the brain parenchyma with subsequent neuronal dysfunction and death (Hardy and Higgins, 1992; Karran et al., 2011). Aβ peptides are 39-43 amino acids long, with the predominant forms being Aβ40 and Aβ42. They are derived from the cleavage of amyloid precursor protein (APP) by two proteolytic enzymes: the β- and γ-secretases. Figure 6.4 illustrates APP and its proteolytic cleavages.

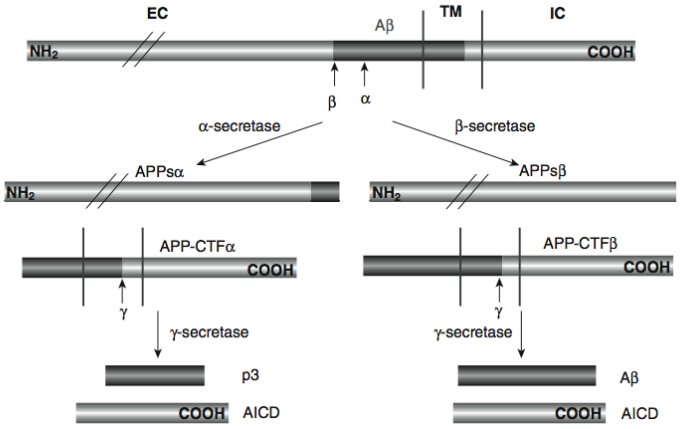

Figure 6.4 The amyloidogenic pathway leading to Aβ production is driven by the β- and γ-secretase action. EC = extracellular domain, TM = transmembrane domain, IC = intracellular domain, CTF = C-terminal fragment, AICP = APP-intracellular domain. From Abraham, *The Handbook of Alzheimer's Disease and Other Dementias,* 2011.

APP is localized at the cellular membrane. β-secretase cleaves at the N-terminus extracellular portion of APP, while γ-secretase action is located at the transmembrane domain, releasing amyloid peptides into the extracellular space. Overproduction of amyloid peptides results in a high peptide concentration in the brain parenchyma, which leads to peptide oligomerization and aggregation (Figure 6.5).

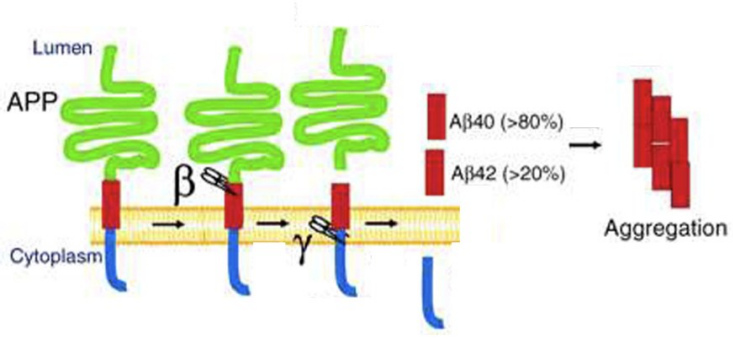

Figure 6.5 Amyloid plaque formation. Adapted from Golde, *J. Clin. Invest.,* 2003.

Aberrant amyloid peptide production leads to a disturbed physiological ratio between Aβ40 and Aβ42 peptides (Abraham, 2011). At autopsy, AD brains contain an extensive amyloid plaque burden following a specific pattern of deposition (Braak and Braak, 1991). Whether the plaque deposition is the primary cause or a consequence of AD remains a controversial issue.

6.1.2.2 Tau Pathology

The other neuropathological hallmark associated with AD is the accumulation of neurofibrillary tangles (NFT). NFTs are composed of hyperphosphorylated tau protein, a microtubule-associated protein. Tau hyperphosphorylation is due to unbalanced activity of intracellular kinases and phosphatases. Hyperphosphorylated tau aggregation is intraneuronal and compromises the microtubule structure leading to NFT and cytoskeletal disruption (Blennow et al., 2006). NFT formation is illustrated in Figure 6.6. The precise aggregation mechanism of hyperphosphorylated tau proteins is not well understood, and whether or not NFT has a causative role in AD is still a matter of debate.

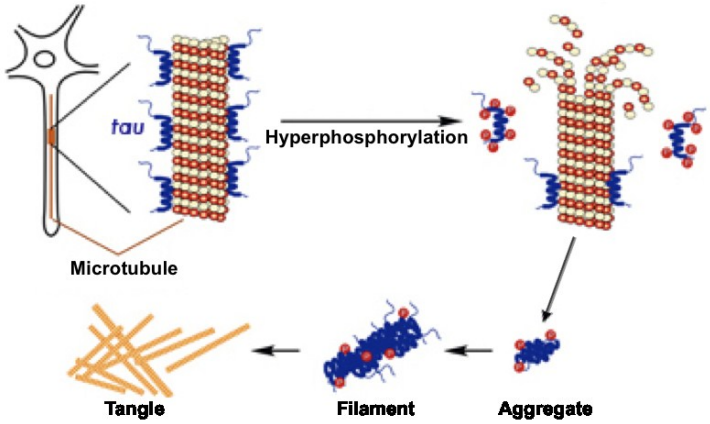

Figure 6.6 Suggested mechanism of NFT formation. Adapted from Sawchenko and Rissman, *Salk Institute for Biological Studies,* 2007.

6.1.2.3 Cerebral Blood Flow Regulation and Dysfunction

The brain receives 15% of the cardiac output and 20% of the total body oxygen consumption to accomplish normal function, despite the fact that it represents only 2% of the body weight (Quastel and Wheatley, 1932; Magistretti and Pellerin, 1996). As such, tight regulation of the cerebral blood supply is critical for structural and functional brain integrity and overall, survival. Under normal physiological conditions, highly controlled mechanisms assure that the blood flow remains constant despite changes in cerebral pressure, and that the blood supply distribution is well-matched to the metabolic demand. These mechanisms are respectively called CBF autoregulation and functional hyperemia (Cipolla, 2009; Peterson et al., 2011). CBF autoregulation does not involve metabolic factors and is limited to vascular tone (Peterson et al., 2011). The endothelium is thought to play an important role in CBF autoregulation because of its production of large amount of vasomodulatory molecules and its mechanoreceptor properties (Edvinsson et al., 1993). Functional hyperemia relies on the neurovascular unit to regulate blood flow, control the blood-brain barrier (BBB) exchange and provide neuronal trophic support. The neurovascular unit consists of the close association between astrocytes, neurons, pericytes, and endothelial cells (Iadecola, 2004). Astrocytes are a main component of the neurovascular unit and act as a physical and functional link between neurons and endothelium, since they surround and can stimulate both synapses and blood vessels (Iadecola, 2004; Attwell et al., 2010). In addition, some evidence suggests the involvement of peripheral nerves to modulate CBF regulation, a phenomenon called neurogenic regulation (Chillon and Baumbach, 2002; Goadsby and Edvinsson, 2002). The CBF regulation is a complex process and coordinated flow response is critical to maintain brain homeostasis. Disruption of these mechanisms can lead to severe cerebrovascular pathologies and, ultimately, to neurodegeneration..

An increasing body of evidence suggests that cerebrovascular dysfunction is tightly related to AD pathophysiology. Cerebrovascular diseases, such as hypertension and stroke, are risk factors for AD, profoundly impair CBF regulation, and may initiate or aggravate the pathology (Kalaria, 2009; Claassen, 2008; Claassen and Zhang, 2011). The intricate relationship between AD and cerebrovascular pathologies is supported by several studies that demonstrate the vasoconstrictor effect of the beta-amyloid peptide on the vessels, as well as the modulatory effect of a hypoxic or ischemic state on amyloidogenesis (reviewed by Iadecola, 2004). In AD patients and Tg AD mouse models, hypoperfusion and impaired endothelial-dependent responses have been reported (Jagust et al., 1998; Johnson and Albert, 2000; Niwa et al., 2002a; Wu et al., 2004; Tong et al., 2005; Bateman et al., 2006; Ongali et al., 2010). Alterations in the structure and function of the neurovascular unit through vascular oxidative stress and inflammation are key factors in cerebrovascular dysfunction. Chronic inflammation is a neuropathological hallmark of AD characterized by reactive astrocytes, which stop providing trophic support to neurons, and produce inflammatory mediators. The abundant production of pro-inflammatory cytokines promotes oxidative stress and increased reactive oxygen species (ROS) and reactive nitrogen species (RNS) production, which leads to protein misfolding and lipid/DNA damage (Attwell et al., 2010; Dasuri et al., 2012; Rubio-Perez and Morillas-Ruiz, 2012). Because of its high oxygen consumption, its high content of polyunsaturated acids and its low antioxidant mechanisms, the brain is highly vulnerable to oxidative stress (Leuner et al., 2012). The additive effect of all the previously mentioned altered cerebrovascular functions is thought to promote neuronal disruption underlying the impaired cognition in AD.

Ultimately, the ability of the brain to maintain homeostasis is dramatically impaired in AD and multiple deregulated cellular pathways are involved in

neurodegeneration. The exact sequence of pathological events remains unknown, and active research activities are currently ongoing to investigate the disease etiology, possible therapeutic agents, and potential biomarkers.

6.2 Magnetic Resonance Imaging

Multiparametric MRI techniques are powerful tools to investigate the structural and functional brain changes that occur during the course of AD development. A comprehensive description of the MRI principles is beyond the scope of this thesis. As such, a simple, high-level overview of the method is provided below.

6.2.1 Structural MRI

Structural MRI relies on the contrast between gray matter, white matter, and cerebrospinal fluid (CSF). Fundamentally, conventional MR images are maps of proton density altered by the surrounding chemical environment and are based on the absorption and emission of radio frequency (RF) energy. Basic structural MRI data includes proton density (PD), T_1-and T_2-weighted images, and the two fundamental parameters of image quality are signal-to-noise ratio (SNR) and spatial resolution.

In MR imaging, the PD images are a function of the mobile hydrogen atom concentration in a given tissue under the influence of a magnetic field. The longitudinal relaxation time (T_1) is the time required for the longitudinal magnetization to fully recover following an RF pulse, and is driven by the thermal interactions between the resonating nuclei and the other nuclei in the lattice. The transverse relaxation time (T_2) is the phase coherence time, which is affected by the magnetic interactions between the spins (Roth, 2011). Examples of PD, T_1- and T_2-weighted images are shown in Figure 6.7.

Spatial resolution is dictated by frequency-encoding, phase-encoding, and slice thickness. SNR is a function of numerous parameters, including voxel size, number of averages, and pulse sequence (Symss et al., 2004).

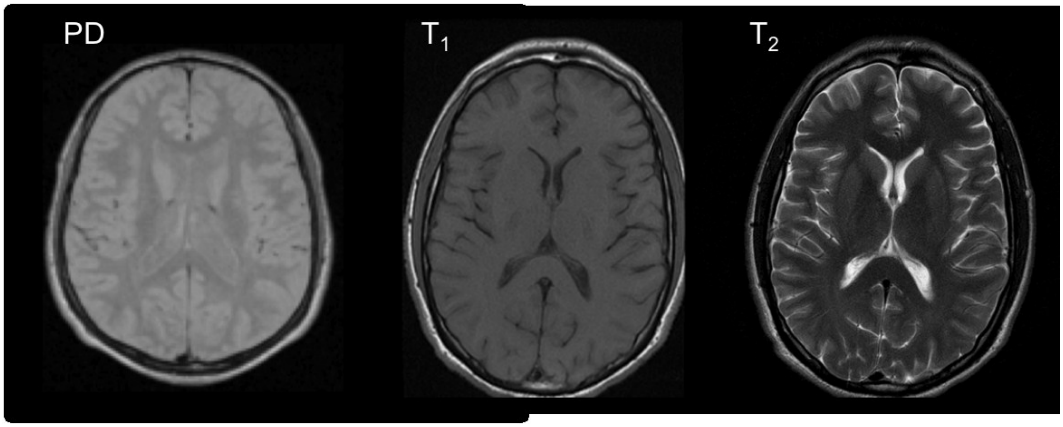

Figure 6.7 Representative axial views of PD, T_1- and T_2-weighted MR images from a human brain. Note the contrast difference between the images. Adapted from Pachai *et al., Int. Conf. Med. Image Comput. Comput. Assist. Interv.,* 2001 and Halterman *et al.*, *University of Rochester Medical Center,* 2009.

6.2.2 Perfusion MRI

Quantification of CBF and cerebral blood volume (CBV) allows for monitoring and assessment of hemodynamic dysfunction. Sophisticated MRI methods of CBF/CBV measurement have been developed, including contrast-enhanced (CE) and ASL MRI.

6.2.2.1 Contrast-Enhanced MRI

It is possible to use MRI to study CBV via the injection of intravascular paramagnetic contrast agents. The presence of the contrast agent in the vasculature alters the local magnetic field and modulates the T_1 and T_2 values. When the tracer reaches a steady-state and a uniform distribution in the vasculature, the CBV can be estimated using the modified T_1 and/or T_2

value. However, CBV evaluation by CE MRI suffers from a quantification issue when vascular permeability is not well-defined (Belliveau et al., 1990; Rosen et al., 1990).

6.2.2.2 Arterial Spin Labeling MRI

ASL perfusion MRI is a non-invasive method to measure CBF, which utilizes blood as an endogenous tracer. The inflowing blood is magnetically labeled by RF pulses, where the labeling plane is positioned inferiorly to the acquisition slice/volume. The magnetically labeled blood flows into the brain and exchanges with tissue blood, which reduces the observable tissue signal. The transit time is the period of time needed for the labeled blood to flow into the complete imaging volume. The acquisition of this *tag image* is interleaved with acquisition of a *control image*, in which the blood is not labeled. The CBF can be calculated based on the tag and control images using a quantitative model. Figure 6.8 illustrates the ASL MRI principles (Detre et al., 1992; Alsop and Detre, 1998).

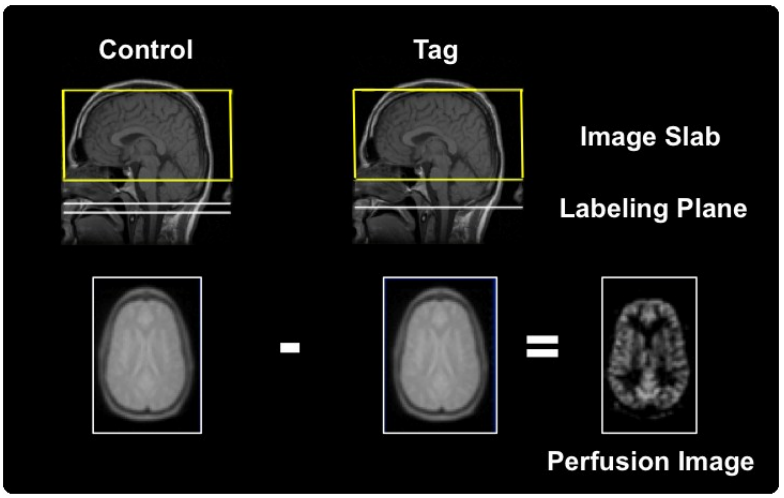

Figure 6.8 ASL MRI principles. Adapted from Alsop and Detre, *Radiology,* 1998.

6.3 Imaging Alzheimer's Disease in Human Brain

MRI has been utilized as a useful tool for diagnosis, disease progression monitoring, and evaluation of drug therapeutic efficacy in AD. The establishment of imaging biomarkers is an active area of research and specific structural and functional patterns of neurodegeneration are currently being explored in order to provide insights into the spatio-temporal pathophysiological changes associated with AD.

6.3.1 Structural MRI

MRI can be used to identify structural alterations because of its high spatial resolution and excellent soft-tissue contrast. Volumetric decline of particular subcortical regions and cortical atrophy are characteristic features of AD neuropathology. While a comprehensive literature review of the structural changes observed in AD patients is beyond the scope of this thesis, Shin *et al.* and Lin *et al.* have provided excellent reviews covering this subject (Shin et al., 2011; Lin et al., 2012). The work presented in this thesis focused on cortical thickness measures and, as such, I will briefly review studies of cortical thickness in human AD.

A "cortical signature" of brain atrophy has been associated with AD. At the early stage of the disease, in very mild demented patients and mild cognitive impairment (MCI) converters, atrophy has been detected in the precuneus and the medial temporal lobe (Buckner et al., 2005). As the severity of dementia increased, the extent of atrophy spread through the cortical areas, including the posterior cingulate, retrosplenial, and lateral posterior parietal cortices. In addition, the rate of cortical atrophy was considerably accelerated in AD patients relative to healthy controls, where the regions mentioned above simply showed normal age-related atrophy (Buckner et al.

2005; Dickerson et al., 2009a; Dickerson et al., 2009b). Progressive cortical atrophy in AD patients can be appreciated in Figure 6.9.

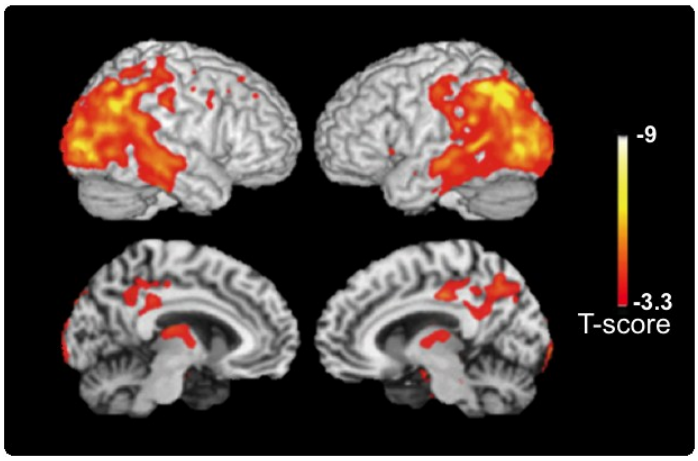

Figure 6.9 Statistical parametric maps of cortical atrophy in AD patients relative to normal controls. Prominent gray matter loss can be appreciated in the parietal and temporal lobes. Adapted from Zhang *et al., J. Alzheimers Dis.,* 2011.

The particular pattern of atrophy detected in AD can be utilized as a diagnostic tool to distinguish AD patients from normal controls, for neurodegenerative staging, and as a predictive indicator of dementia. Lerch *et al.* used the mean thickness measures from cortical regions-of-interest (ROIs) to separate AD patients from healthy controls (Lerch et al., 2008a). They found that AD subjects could be discriminated from normal subjects by using mean cortical thickness across the entire cortex with 75% accuracy. In addition, the combination of two ROIs, always including the parahippocampal gyrus as one of the two structures, improved the group separation, reaching an accuracy of 100%. Cortical thickness assessment has been utilized as an early diagnostic marker for AD. Decreased baseline cortical thickness in progressive MCI patients, relative to stable MCI patients and controls, predicted their conversion to AD (Querbes et al., 2009). Subtle thinning in vulnerable cortical regions, *e.g*. the medial temporal lobe, was detectable in cognitively normal amyloid-positive patients and was a

predictive factor for AD. Moreover, the extent of the cortical thinning pattern was related to dementia severity over the timecourse of the neurodegenerative process (Dickerson et al., 2009a; Dickerson et al., 2009b; Dickerson et al., 2011). The specific pattern of atrophy progression in AD has been used to improve diagnosis accuracy between AD and frontotemporal dementia (FTD), which present overlapping clinical symptoms (Zhang et al., 2011).

Structural MRI is a widely available imaging modality providing quantitative measures of neuroanatomical abnormalities. Cortical thickness assessment has been proven to be a highly reliable imaging biomarker for prediction and staging in AD.

6.3.2 CBF Measurement Techniques

Quantitative CBF measurements in human brain have emerged in the 1950's and primarily relied on inert indicator techniques. These approaches are based on the principle that following indicator injection into the bloodstream, the blood flow can be measured by the rate of the indicator clearance, either directly from the tissue or by arterial blood sampling (reviewed by Ingvar and Lassen, 1965). Kety and Schmidt (Kety and Schmidt, 1948) developed the nitrous oxide inhalation method, which derived a CBF measure by sampling the arterial and venous nitrous oxide concentrations at the jugular bulb during a 10-minute period of its inhalation. This technique has been widely used (Schmidt, 1950; Pierce et al., 1962) and modified to improve its accuracy (Lassen and Munck, 1955; McHenry, 1964). The intra-arterial isotope injection method has been used for quantitative, regional CBF measurement (Lassen and Ingvar, 1961). Briefly, following internal carotid injection of ^{85}Kr or ^{133}Xe, one brain hemisphere is labeled by the isotope and its uptake and clearance can be

recorded by β-ray detectors positioned over the skull (Lassen and Ingvar, 1961; Lassen et al., 1963; Hoedt-Rasmussen, 1965).

Derived from the intra-arterial isotope injection method, the ^{133}Xe inhalation procedure has been developed in order to satisfy the need for a non-invasive technique for CBF measurement (Mallett and Veal, 1963; Obrist et al., 1975). Rather than being injected, the isotope is inhaled via a facemask and the signal is recorded by detectors surrounding the skull. This technique has been extensively used to investigate CBF impairment in AD. Using this method, Barclay *et al.* (Barclay et al., 1984) reported a progressive CBF decline in AD patients. Furthermore, reduced regional CBF in frontal and temporal cortices of AD patients has been demonstrated (Tachibana et al., 1984). CBF measurement by ^{133}Xe inhalation has also been used to discriminate AD patients from multi-infarct dementia patients (Deutsch and Tweedy, 1987).

More recently, tomographic imaging techniques that detect ionizing radiations, *i.e.* γ-rays, have been used to assess CBF, including single-photon emission computed tomography (SPECT) and PET. SPECT imaging relies on the direct detection of a γ-emitting tracer from multiple angles to compute a 3D image of the tissue of interest (Massoud and Gambhir, 2007; Herholz, 2011). ^{99m}Tc –hexamethylpropyleneamine oxime (^{99m}Tc –HMPAO) and ^{99m}Tc-ethyl cysteinate dimer (^{99m}Tc-ECD) are used as SPECT perfusion imaging agents, since their distribution in the brain can be approximated proportionally to the CBF (van Dyck et al., 1996).

In contrast to SPECT, PET tracers are radiolabeled ligands which emit positrons. The emitted positrons annihilate with nearby electrons to produce two high-energy photons 180° apart. The PET scanner records these two simultaneous emissions and reconstructs an image based on the frequency and localization of these events (Jones, 1996; Massoud and Gambhir, 2007). Imaging CBF by PET is performed indirectly, assuming that

regions with high radioligand uptake are associated with high brain activity. As such, ^{15}O-H_2O and ^{18}F-FDG have been extensively used for CBF measurement (Jacobs et al., 2002; Jones and Rabiner, 2012). Altered global and regional CBF in MCI and AD subjects has been widely reported using SPECT and PET imaging (Johnson and Albert, 2000; Schuff and Zhu, 2007; Herholz, 2011).

The previously mentioned techniques for CBF evaluation are either invasive, use ionizing radiation, or both. Near-infrared spectroscopy (NIRS) is a non-invasive technique, which probes the changes in optical properties of a given tissue. For CBF assessment, the changes in light absorption are converted into changes in cerebral oxy- and deoxyhemoglobin from which the CBF measure can be derived. An induced change in arterial oxyhemoglobin concentration can also be used as perfusion tracer. However, NIRS perfusion assessment is limited to superficial cerebral cortex (Elwell et al., 1994; Owen-Reece et al., 1996). NIRS, however, offers some advantages over other techniques, mainly concerning the environment. The subject sits in a comfortable chair wearing a helmet and does not experience scanner noise or feel confined in the scanner apparatus. As such, NIRS has been used to assess CBF in patients with neurodegenerative /psychiatric conditions. An altered hemodynamic response in the parietal cortex has been reported in AD patients (Zeller et al., 2010). Furthermore, using NIRS, van Beek *et al.* described AD-related abnormalities in the cerebral microvasculature of demented subjects (van Beek et al., 2012). Therefore, multiple techniques for CBF assessment have been developed over the past decades and are useful tools to monitor and characterize AD.

6.3.3 Perfusion MRI

Neurovascular function is profoundly impaired in AD and is known as a critical, dysregulated neurophysiological process (Iadecola, 2004; Nicolakakis and Hamel, 2011). CBF measurement can be achieved using ASL

MRI. Since this technique does not require the injection of a contrast agent or the use of ionizing radiation, it is an attractive modality to investigate vascular alterations (Detre et al., 1992). ASL MRI has been utilized to characterize, predict, and monitor AD.

Alsop *et al.* reported the first quantitative CBF evaluation by ASL MRI in AD patients (Alsop et al., 2000). They observed a profound hypoperfusion in AD subjects relative to age-matched healthy controls in the temporal, parietal, frontal, and posterior cingulate cortices. By accounting for partial volume effect (PVE) resulting from cortical atrophy, regional hypoperfusion in more restricted areas, specifically the inferior parietal lobe, posterior cingulate, and middle frontal gyrus, was observed in AD patients (Johnson et al., 2005). Figure 6.9 shows the profound CBF alteration in AD patients.

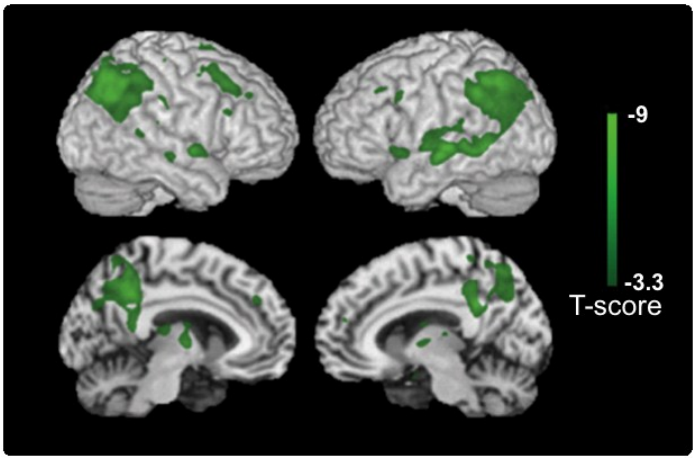

Figure 6.10 Statistical parametric maps of hypoperfusion in AD subjects relative to healthy controls. The perfusion reduction was localized to the temporal and parietal lobes. Adapted from Zhang *et al., J. Alzheimers Dis.,* 2011.

Characteristic hypoperfusion patterns have been described as a specific signature for cognitive decline. The spatial distribution of hypoperfusion allowed improved classification between FTD and AD (Du et al., 2006). MCI and AD patients have been shown to present a sequential pattern of altered

CBF reflecting the dynamic process of neurodegeneration (Dai et al., 2009). Hypoperfusion in specific regions was reported in AD and has been suggested to be predictive of subsequent cognitive decline and conversion to AD (Chao et al., 2010). Chen *et al.* compared the pattern of hypoperfusion by ASL MRI and glucose hypometabolism by 2-[^{18}F]fluoro-2-deoxy-D-glucose (FDG) positron emission tomography (PET), and found that ASL perfusion data recapitulated FDG PET data, further emphasizing ASL MRI as a valuable tool for functional abnormality evaluation in AD (Y. Chen et al., 2011). As such, ASL MRI has become a powerful tool to assess cerebrovascular dysfunction in AD, identify potential AD sufferers prior cognitive decline, and differentiate AD from other types of dementia.

6.4 Transgenic Alzheimer's Disease Mouse Models

6.4.1 Overview

The development of animal models of neurodegenerative disorders is critical to elucidate disease mechanisms and translate experimental therapeutic approaches. They allow for the assessment of patterns of metabolic and cellular disruption related to the underlying neuropathology. However, the validity of an animal model relies on its ability to mimic multiple aspects of a given pathology. In the case of AD, the emphasis has been on the development of Tg mice models expressing AD pathological markers, as well as progressive cognitive decline.

The identification of genetic factors contributing to disease progression lead to the engineering of mouse models recapitulating characteristic molecular patterns of neurodegeneration. Many Tg models overexpress a mutant APP protein, leading to high amyloid plaque burden. The spatial pattern of plaque deposition roughly corresponds to the affected areas in human AD, with related cognitive impairment. Also, mutations leading to increased secretase activity are often associated with APP mutations in these models. As

reported in AD patients, mutations within the presenilin (PS) sequence, an enzyme involved in secretase activity, lead to increase soluble amyloid production and plaque deposition, as well as to cognitive decline. In addition, mouse models recapitulating tau pathology are being explored. Current mouse lines, however, are more associated with a FTD or Parkinson disease phenotypes, rather than AD. Mouse models expressing human APOE isoform transgenes have also been extensively studied to investigate the role of APOE mutations in Aβ pathology. As such, numerous models recapitulating one or multiple aspects of AD exist, and excellent reviews are available (Higgins and Jacobsen, 2003; Kim et al., 2009; Waerzeggers et al., 2010). A summary of the most extensively studied AD Tg mouse models is presented in Table 1.

Mouse lines	Transgene (Mutation)
PDAPP	$APP_{(V717F)}$
Tg2576	$APP_{695(K670N,M671L)}$
APP23	$APP_{751(K670N,M671L)}$
APP/PS1	$APP_{695(K670N,M671L)}$ + $PS1_{(M146L)}$
JNPL3	$TAU_{(P301L)}$
TAPP	$TAU_{(P301L)}$ + $APP_{695(K670N,M671L)}$
mApoE	$APP_{(V717F)}$ + mouse APOE
ApoE4	$APP_{(V717F)}$ + human APOE4

Table 1 Summary of AD mouse models and their associated transgene.

6.4.2 J20 Line

In our lab, intensive work on a Tg mouse model of amyloidogenesis has been performed. This mouse model has an early amyloid-related pathology with plaque deposition starting around 6 months-of-age. This mouse line also models the cerebral amyloid angiopathy (CAA) and vascular impairments found in AD patients. The J20 line was created in 2000 and

bears the Swedish (Sw) and Indiana (Ind) mutations of the APP sequence (Figure 6.10), resulting in a heavy plaque burden (Mucke et al., 2000).

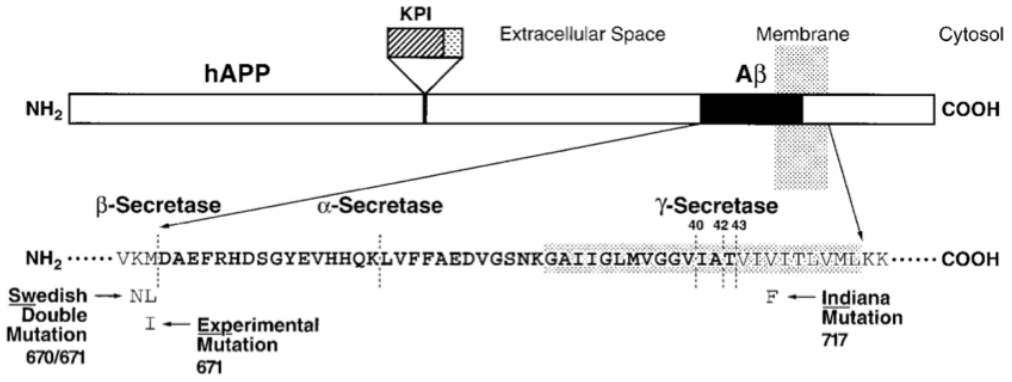

Figure 6.11 Mutation sites of human APP expressed in J20 line. The Aβ sequence is indicated in bold. Adapted from Mucke *et al., J. Neurosci.,* 2000.

This Tg mouse line is a well-characterized AD model and presents some of the critical aspects of the pathology. It produces a high level of Aβ42 and the age-dependent pattern of plaque deposition has been well-described (Mucke et al., 2000). In addition, the J20 line has a loss of synaptic density related to soluble Aβ levels and cognitive impairment, especially with respect to the spatial component of learning and memory (Mucke et al., 2000; Palop et al., 2003). Moreover, cerebrovascular dysfunction following vasodilatory challenges, and oxidative stress associated to manganese superoxide dismutase (SOD2) upregulation have been studied in this mouse model (Tong et al., 2005). The hippocampal CBV deficit linked to Aβ neurotoxicity over time has been mapped, and the entorhinal cortex has been identified as the most vulnerable neuroanatomical region (Moreno et al., 2007). Also, the dynamics of the amyloid peptide concentration between the brain interstitial fluid (ISF) and the amyloid dense plaques has been investigated (Hong et al., 2011).

In conclusion, the J20 line provides powerful tool to investigate the mechanisms underpinning the neurodegenerative processes linked to AD. This Tg mouse model recapitulates a broad range of the pathological events observed in AD patients and, thus, offers an advantageous opportunity to investigate the disease etiology related to amyloid deposition.

6.5 Imaging of Transgenic Alzheimer's Disease Mouse Models

MRI is a translatable methodology and, as such, is a powerful tool to link data from mouse models recapitulating AD neuropathology to observations in human AD subjects.

6.5.1 Structural MRI in AD Mouse Models

Accurate evaluation of brain atrophy in mice has been a challenge. While histological and stereological approaches have been reported, they involve brain distortion and tissue shrinkage due to skull removal and tissue processing/sectioning, and, obviously, cannot be used for longitudinal study designs (Dodart et al., 2000; Gonzalez-Lima et al., 2001). During the past 10 years, structural MRI has been used to perform morphometric studies in AD mouse models.

6.5.1.1 Manual and Semi-Automated Image Processing

The first image analysis approach used for structural image processing was a manual delineation of ROIs on successive or selected image slices followed by volume calculation. This strategy is time-consuming and labor-intensive, and focuses on brain structures defined *a priori*. In order to be performed correctly, it requires an expert anatomist, which introduces subjective bias and intra-/inter-rater variability. Nevertheless, this technique has provided insights about neuroanatomical structures well-known to be affected in AD, and confirmed the relevance of AD Tg mice models for investigating neurodegenerative processes.

In 2002, Weiss *et al.* published the first structural MRI study in an AD Tg mouse model (Weiss et al., 2002). They reported a decreased hippocampal-to-brain volume ratio in PDAPP$_{V717F}$ Tg mice relative to WT mice. Reduced

hippocampal volume has been also observed in PDAPP Tg mice at pre-plaque (3.5 month-old) and plaque-deposition (21 month-old) stages. The progression of the volumetric decline over time was stable (Redwine et al., 2003). However, no change in total brain volume in Tg mice relative to WT mice at 3.5 and 21 months-old was detected. Alternatively, a significant reduction in whole brain volume has been described at 2.5 months-of-age in APP/PS1 mice, which also showed a greater atrophy rate over time (Delatour et al., 2006). Oberg *et al.* reproduced the findings mentioned above in an APP/PS1 mouse model (Oberg et al., 2008). Using a longitudinal study design, they found decreased brain and hippocampal volumes at 2.5 and 9 months-of-age in Tg mice. Furthermore, they assessed the lateral ventricle volume and observed a ventricular enlargement in the Tg group compared to the WT group for the same timepoints. Similarly, reduced whole brain and cortical volumes were reported in APP-Austrian (Au) Tg mice at 12 and 20 months-of-age (van Broeck et al., 2008a). Although no volume change was observed in hippocampus, a decreased whole brain volume over time was suggested. The same group further investigated the structural alterations in this mouse model. At 10 days-old, the total brain volume of APP-Au mice was similar to WT mice, ruling out neurodevelopmental impairment as the cause of the volume decrease. A significant brain volume reduction was still observed at 12 and 20 months-of-age (van Broeck et al., 2008b). Profound regional volume alterations have also been reported in the APP/SOD Tg model (Borg and Chereul, 2008). At 12 months-old, the APP/SOD double Tg group had smaller cortical volumes than single Tg SOD, APP, and WT groups, and smaller entorhinal cortex and hippocampal volumes than the WT group, without significant difference in whole brain volume among all groups.

Volumetric assessments based on manual segmentation have provided evidence of whole brain and regional atrophy in multiple AD mouse models, recapitulating the neuroanatomical abnormalities reported in human AD subjects. However, there are significant discrepancies in the reported results

across animal imaging studies. The use of different mouse models can explain some of these discrepancies, since the various genetic backgrounds can account for variability in the observed phenotype. In addition, differences in the image processing can also account for inter-study variability. The manual ROI segmentation introduces analyst-related bias in the structure delineation, which might not be consistent across different studies. Furthermore, in some studies, only few brain slices of the total anatomical scan were selected and averaged to represent the neuroanatomical structure, thereby providing only an approximation of the regional volume instead of a comprehensive evaluation. Further, the manual tracing protocol and the segmentation criteria for ROI definitions were not consistent among studies, and, as such, can explain the lack of consistency of these published reports.

6.5.1.2 Automated Image Processing

High throughput, automated, and unbiased image processing techniques have been developed in order to detect neuroanatomical changes occurring in AD mice models. Two major image processing approaches have been utilized. The first is atlas-based segmentation, which allows regional volumetric comparisons between groups and timepoints on a structure-by-structure basis (ROI-based analysis). The second is deformation-based morphometry (DBM), which interrogates local anatomical differences on a voxel-by-voxel basis.

Using DBM, Lau *et al.* (Lau et al., 2008) observed significant local volumetric decreases in cortical regions, including somatosensory, cingulate and retrosplenial cortices, and volumetric increase in lateral and third ventricles in APP/PS1 mice from 2.5 to 9 months-of-age. Maheswaran *et al.* (Maheswaran et al., 2009a) compared DBM and ROI-based analysis to detect longitudinal structural changes in the APP/PS1 mouse model. They observed

prominent growth over time in whole brain, cerebral cortex, hippocampus, and cerebellum in the Tg group compared to the WT group with both methods. In addition, they provided a comprehensive ROI-based analysis of the same APP/PS1 mouse model using a longitudinal study design (Maheswaran et al., 2009b). Global brain volume increase was observed in APP/PS1 Tg mice. Nonetheless, in the Tg group, the thalamus, cerebellum, cerebral cortex and caudate putamen showed a greater rate of decline, while the total ventricle area was increased. However, in an inducible $APP_{Sw/Ind}$ line, the whole brain, striatum, hippocampal, and cortical volume reduction over time was described in Tg mice (Badea et al., 2010).

Several MRI studies using automated image processing have been reported (Lau et al., 2008; Maheswaran et al., 2009a; Maheswaran et al., 2009b; Badea et al., 2010). As mentioned above, the use of different AD mouse models can lead to variable volumetric data for a particular region. The discrepancies in the result outcomes may be related to differences in the volume measurement process, since no gold-standard or common operating procedures have been established. Most of the reported ROI-based studies used a pre-defined atlas. However, these atlases were not derived from the specific mouse population of the study, and, as such, did not account for the morphological differences of the different mouse groups. A DBM approach detected significant volume differences in smaller anatomical regions than the ROI-based approach, but suffered from a laborious voxel-by-voxel analysis and interpretation (Lau et al., 2008; Maheswaran et al., 2009a).

While volumetric changes have been extensively studied in several AD mouse models, cortical thickness assessment using structural MR images has only recently been explored. Cortical thickness measures were calculated using the average of multiple manual measurements in several cortical regions in Pax6 deficient mice (Boretius et al., 2009). Similarly, cortical thinning at the somatosensory cortex level of APP/PS1 mice was reported by manual

evaluation of the distance along a perpendicular line drawn between the corpus callosum and the cortical surface from selected coronal sections (Badea et al., 2010). These manual measurements had the same disadvantages as the manual segmentation discussed above. Lerch *et al.* reported the first automated cortical thickness measurement algorithm for mouse brain MRI data and applied it to the study of a Huntington's disease mouse model (Lerch et al., 2008b). Application of this image processing approach with AD mouse models would allow for reliable assessment and complete coverage of the cortical mantle, and therefore, provide better translatability to the cortical thickness signature found in human AD patients.

Monitoring structural changes in AD has allowed us to gain substantial insight into the pathological events occurring during the time course of the disease. Approaches for extracting structural data from MRI scans have been intensively developed and are increasingly becoming more sophisticated. Structural MRI is now established as a powerful tool to study neurodegeneration.

6.5.2 Perfusion MRI in AD Mouse Models

Cerebrovascular dysfunction is a characteristic neurophysiological process in AD. Transgenic AD mouse models recapitulating the compromised vascular dysfunction are valuable tools to investigate the dynamics of neurodegeneration. Several techniques have been used to study CBF alterations in AD mouse models.

6.5.2.1 Invasive and Terminal Cerebral Blood Flow Assessment

Deficits in CBF have previously been measured in AD mouse models using highly invasive and terminal procedures, such as quantitative autoradiography and Laser Doppler flowmetry (LDF). Niwa *et al.* were the

first to report CBF alterations in an AD mouse model (Niwa et al., 2002a). They observed a global brain hypoperfusion at the pre-plaque stage (2-3 months-old) in Tg2576 mice, an AD line producing a high level of β-amyloid, while age-matched Tg2123, a line producing lower β-amyloid levels, showed significant hypoperfusion only in telencephalic regions. The same research group described impaired cortical CBF response at 2-3 months-of-age in the Tg2576 model by variation of the mean arterial pressure as hemodynamic challenge (Niwa et al., 2002b). In addition, cortical hypoperfusion, especially in parietal and occipital cortices, has been described in the APP_{Swe} Tg mouse model at 13 and 20 months-of-age (Paris et al., 2004). However, contradictory results were reported in the same model used in the Niwa study (Niwa et al., 2002b). Shin *et al.* (Shin et al., 2007) observed an attenuated hemodynamic response at 19 months-of-age in the Tg2576 model, but not at 8 months-old. Since impaired cerebrovascular function has been reported in the same AD mouse model at 2-3 months-of-age (Niwa et al., 2002b), a similar dysfunction would have been expected at 8 months-old (Shin et al., 2007). Inconsistency between these two studies may be explained by differences in the experimental procedure. The Niwa study (Niwa et al., 2002b) performed a craniotomy and used an open skull preparation, while Shin *et al.* (Shin et al., 2007) executed the LDF experimentation through an intact skull. The intact skull preparation avoided possibility of injury during dural excision, exposure to air, variation of cortical temperature, and inconsistency of intracranial pressure.

Besides being a terminal procedure, LDF allows only the investigation of a restricted region of the cortical surface. In addition, probe position and motion artifacts have a high impact on the reliability of the technique. Non-terminal procedures, which allow whole brain coverage and longitudinal study designs, are now possible to assess CBF.

6.5.2.2 Cerebral Blood Flow Assessment by MRI

MRI is a very suitable modality for vascular function measurement, and multiple approaches have been used to evaluate compromised CBF in AD mouse models. CE MRI has been largely employed to study CBV and cerebrovascular reactivity in AD mouse models. Mueggler *et al.* (Mueggler et al., 2002) described a reduced and delayed hemodynamic response in cortical and thalamic regions of 25 month-old APP23 mice after bicuculline and acetazolamide vasodilatory challenge. They also found an impaired somatosensory response in the APP23 mouse model (Muggler et al., 2003). After electrical paw stimulation, the hemodynamic response of the contralateral somatosensory cortex was reduced in Tg animals relative to WT mice in an age-dependent fashion. Moreover, CBV decrease was observed in the cerebral cortex, hippocampus, and thalamus in 4 month-old $APP_{Sw/Ind}$ Tg mice (Wu et al., 2004). Similarly, global decreases in resting CBV were found in APP/PS1 mice at 15 months-of-age (Hooijmans et al., 2007). Zerbi *et al.* used a longitudinal study design to investigate cerebrovascular dysfunction in APP/PS1 mouse model (Zerbi et al., 2012). At 8 months-old, the Tg group showed impaired CBV in cortical regions and in the thalamus. With aging, the CBV reduced extensively in cortical and subcortical areas, including primary somatosensory areas, secondary motor areas, hypothalamus, hippocampus, and cerebellum. Consequently, CE MRI is a suitable technique to evaluate CBV and hemodynamic responses in AD mouse models. Compared to CE MRI, ASL does not require the injections of contrast agent and is, therefore, more readily transferable to human AD studies.

In 2009, Weidensteiner *et al.* reported the first ASL perfusion MRI study in an AD mouse model (Weidensteiner et al., 2009). They observed hypoperfusion in the occipital cortex in B6.PS2APP mice at 10, 12, and 17 months-of-age. In addition, the temporal pattern of hypoperfusion showed a significant decrease from 10 to 12 months-of-age in the occipital cortex in Tg mice. Also, profound general cortical hypoperfusion has been reported in aged Tg2576

mice (Massaad et al., 2010). Further, perfusion deficits were also measured at 6 months-of-age in posterior cortex, but not in subcortical structures in APP/PS1-Ki mice (Faure et al., 2011). Abnormalities in the vascular system are a common pathological feature of AD. Preliminary CE and ASL MRI studies have reported CBV and CBF defects in AD mouse models.

6.5.2.3 Imaging The Arterial Tree

The techniques mentioned above focus on the CBV/CBF related to the capillary bed and do not assess the microstructural changes in the arterial tree. Cerebrovascular abnormalities, known as CAA, are frequently observed in AD patients. Such abnormalities are caused by Aβ peptide deposition on the vessel walls and lead to vessel narrowing and occlusion, as well as to disruption of the smooth muscle cells (Thal et al., 2008).

In 2001, Christie *et al.* observed vascular impairment in an AD mouse model (Christie et al., 2001). They determined that at 14 months-old, but not at 6 months-old, Tg2576 mice had a decreased reactivity of the pial arteries after acetylcholine and sodium nitroprusside dilatory challenge. The vascular measurements were performed by video microscopy following a closed cranial window preparation. They used a highly invasive technique, which does not allow for longitudinal or repeated study design. Since then, non-invasive imaging modalities, such as magnetic resonance angiography (MRA), have been utilized to complement vascular tree alteration assessment.

By combining MRA and corrosion cast techniques, arterial impairments were observed in the large arteries of the circle of Willis in APP23 mice, namely the carotid, palatine, and pterygopalatine arteries (Beckmann et al., 2003). In addition, at the cortical supply level, flow voids were detected at the anterior, middle, and posterior cerebral arteries. The first vascular alterations occurred at 7 months-of-age for some arteries, but mainly and most

extensively at 20 months-old following an age-related progression in Tg animals (Beckmann et al., 2003). Corroborating these findings, Meyer *et al.* described substantial evidence of age-dependent morphological and architectural vascular alterations starting before plaque deposition in the APP23 mouse model using corrosion casts (Meyer et al., 2008). Han *et al.* investigated the relationship between cerebrovascular dysfunction and CAA in the leptomeningial arteries of young (6 months-old) and old (12 months-old) Tg2576 mice (Han et al., 2008). They found that vasoreactivity was already impaired in young Tg animals at the pre-CAA stage. In old Tg mice having extensive CAA, arterial dysfunction was globally more pronounced, but also, vascular reactivity alteration was further compromised in arterial segments presenting heavier CAA load. Consequently, there was an apparent relationship between local CAA deposition and vascular integrity. Moreover, in 25 month-old APP23 mice exhibiting severe CAA compared to CAA-free WT littermates, additional flow disturbances were described in the thalamoperforating arteries and at the distal section of the posterior cerebral artery (PCA) (Thal et al., 2009). Furthermore, vascular abnormalities were detected in the middle cerebral artery (MCA) of old APP/PS1 mice relative to PS1 controls (El Tayara et al., 2010). Blood flow alterations at the MCA level and in the anterior communicating artery were also reported in TG2576 mouse model (Kara et al., 2012). MRA, a non-invasive tool, has provided useful information to study pathological abnormalities at the arterial level. It has demonstrated severe arterial defects in large- and medium-sized vessels in AD mouse models.

Preface to Chapter 7

The experiments and results from my project are presented in this manuscript-based thesis. The following paper has been published in *Neurobiology of Aging* (Hébert, Grand'Maison et al., 2013). We investigated the spatio-temporal pattern of cortical thickness and perfusion changes in an AD Tg mouse model at 3, 12, and 18 months-of-age.

Contributions of Authors

The following manuscript is entitled "*Cortical atrophy and hypoperfusion in a transgenic mouse model of Alzheimer's disease".* I, Marilyn Grand'Maison (MGM), am first co-author along with François Hébert (FB), the co-authors are Ming-Kai Ho (MKH), Jason P. Lerch (JPL), Edith Hamel (EH) and Barry J. Bedell (BJB). This project was supervised and funded by BJB. EH provided the transgenic animals used for this study as a collaborator at the Montreal Neurological Institute. I was actively involved in the data processing and analysis. FH and I validated the automated data processing pipeline. The manuscript was written by BJB and me. MKH was responsible for coordinating the project. BJB wrote the MRI sequences employed for structural and perfusion scan acquisition. JPL developed the method for extracting the cortical thickness data. BJB is the corresponding author on the manuscript.

Chapter 7

Title: Cortical atrophy and hypoperfusion in a transgenic mouse model of Alzheimer's disease

Authors: François Hébert[a1], Marilyn Grand'Maison[a1], Ming-Kai Ho[a], Jason P. Lerch[c], Edith Hamel[b], Barry J. Bedell[a*]

[a]Small Animal Imaging Lab, McConnell Brain Imaging Centre, and [b]Laboratory for Cerebrovascular Physiology, Department of Neurology & Neurosurgery, Montreal Neurological Institute, McGill University
3801 University Street, Montreal, QC, Canada, H3A 2B4

francoishebert@hotmail.fr

marilyn.grandmaison@mail.mcgill.ca

ming.ho@mcgill.ca

edith.hamel@mcgill.ca

barry.bedell@mcgill.ca

[c]Mouse Imaging Centre, Hospital for Sick Kids

25 Orde Street, Toronto, ON, Canada, M5T 3H7

jason@phenogenomics.ca

[1]These authors contributed equally to this work.

Corresponding Author:

Barry J. Bedell, M.D., Ph.D.
Montreal Neurological Institute, McGill University
3801 University Street, Room NW-111
Montreal, QC, H3A 2B4
Canada
Phone: 1-514-398-8804
Fax: 1-514-398-6547
E-mail: barry.bedell@mcgill.ca

Abstract

Magnetic resonance imaging (MRI) studies have revealed distinct patterns of cortical atrophy and hypoperfusion in Alzheimer's disease (AD) subjects. The relationship between these *in vivo* imaging measures and the corresponding underlying pathophysiological changes, however, remains elusive. As such, recent attention has turned to neuroimaging of mouse models of AD, in which imaging-pathological correlations can be readily performed. In this study, we acquired anatomical and arterial spin labeling (ASL) perfusion MRI scans on APP transgenic and age-matched wild-type mice at 3, 12, and 18 months-of-age. We employed fully-automated image processing methods to derive quantitative measures of cortical thickness and perfusion. These studies revealed increased regional cortical thickness in young transgenic mice relative to age-matched wild-types. However, the transgenic mice generally demonstrated a greater rate of cortical thinning over 15 months. Cortical perfusion was significantly reduced in young transgenic mice in comparison to wild-type mice across most brain regions. We have identified previously unreported regional genotype differences and age-related changes in cortical thickness and cerebral perfusion in APP transgenic and wild-type mice.

Keywords: Alzheimer's disease; APP mouse model; cerebral perfusion; cortical thickness; magnetic resonance imaging

1. Introduction

Non-invasive neuroimaging-based measures of regional cerebral perfusion, metabolism, and structure are increasingly utilized to improve our understanding of the natural evolution of Alzheimer's disease (AD) and to evaluate response to therapeutic intervention. [18F]2-fluoro-2-deoxyglucose (FDG) positron emission tomography (PET) has been extensively utilized in AD studies, and characteristic patterns of AD-associated glucose hypometabolism have emerged (Mosconi et al., 2010; Mosconi and McHugh, 2011). Given the wider availability of magnetic resonance imaging (MRI) compared to PET scanners, it is highly desirable to identify similar, MRI-based measures of brain function. Strong concordance between regional hypoperfusion and glucose hypometabolism measured by arterial spin labeling (ASL) perfusion MRI and FDG PET, respectively, has recently been demonstrated in AD patients (Y. Chen et al., 2011). Regional cerebral hypoperfusion has been suggested to be an early imaging biomarker for AD (Alsop et al., 2010; Chao et al., 2010), and large-scale studies employing ASL MRI, such as ADNI-2 (Jack et al., 2010), are currently underway. These cerebral blood flow (CBF)/metabolism measures are complemented by quantitative, structural information derived from anatomical MR images. Volume- and surface-based morphometry measures have revealed well-defined patterns of brain atrophy across the spectrum of AD progression (reviewed by Lin et al., 2012).

Recent studies have demonstrated that structural and functional brain alterations have distinct spatial patterns. J.J. Chen et al. (2011) found that the regional effects of age on CBF, which was most prominent in the superior frontal, orbitofrontal, superior parietal, middle/inferior temporal, insular, precuneus, supramarginal, lateral occipital and cingulate regions, differed from that of gray matter atrophy in normal aging. Tosun et al. (2010) performed a joint analysis of structural and perfusion MRI data in AD, and determined that structural and physiological brain changes in AD provide complementary information. The analysis performed in this study also indicated that cortical thinning had a greater association with the variability of AD severity than the CBF measures. Based on these studies, an apparent dissociation between structural and cerebral perfusion measures in normal aging and AD exists, but the biological underpinnings of this counterintuitive imaging data remains elusive.

The routine clinical use of quantitative MRI and PET biomarkers for diagnosis, staging, and therapeutic efficacy monitoring in AD has been hampered by a relatively poor understanding of the pathophysiological processes underlying these measures. The ability to tightly link non-invasive imaging measures with microscopic and molecular processes in human subjects is challenging and often impossible to achieve. Alternatively, studies of animal models of AD allow for tight correlation of *in vivo* imaging and invasive and /or post-mortem data. Transgenic (Tg) murine models with targeted expression of mutant human amyloid precursor protein (APP) genes

recapitulate many of the cognitive and neuropathological features of AD, and high-resolution images from the brains of these mice can be obtained with dedicated, high-field, small animal MRI systems.

Several recent studies have identified differences in whole or regional brain volumes between APP Tg and wild-type (WT) mice (Delatour et al., 2006; Lau et al., 2008; Oberg et al., 2008; Maheswaran et al., 2009; Badea et al., 2010). Cortical hypoperfusion has also been observed in mutant APP Tg mice by ASL MRI (Weidensteiner et al., 2009; Massaad et al., 2010; Faure et al., 2011; Poisnel et al., 2012). However, a detailed examination of the relationship between regional cortical surface morphometry and perfusion across the lifespan of APP Tg mice has not been performed.

In this study, we sought to examine the spatio-temporal pattern of altered cortical structure and blood flow over a 15 month period in a well-established mouse model of AD pathology by MRI. We have employed non-invasive, whole brain, 3D MRI acquisition and sophisticated, fully-automated image processing/analysis methods to interrogate the relationship between cortical thickness and perfusion in Tg and age-matched WT mice. We anticipate that the unique observations from this study will provide a basis for further investigation of the complex interplay between macroscale (imaging) and microscale (cellular) processes in AD.

2. Materials and methods

2.1 Animals

Heterozygous transgenic mice with neuronal overexpression of the Swedish ($670/671_{KM\rightarrow NL}$) and Indiana ($717_{V\rightarrow F}$) mutations of human APP driven by the platelet-derived growth factor β (PDGF-β) promoter on a C57BL/6J background (line J20) (Mucke et al., 2000; Tong et al., 2005) were used for these studies. This model has been well-characterized for amyloidosis (Mucke et al., 2000), cognitive/behavioral impairments (Palop et al., 2003), and cerebrovascular dysfunction (Tong et al., 2005).

Separate cohorts of mice at three ages were evaluated in a cross-sectional study design, specifically Young (age = 3.3 ± 0.2 months; n = 19 Tg [9 male, 10 female], 20 WT [10 male, 10 female]), Middle-Aged (age = 12.7 ± 1.3 months; n = 20 Tg [10 male, 10 female], 20 WT [10 male, 10 female]), Old (age = 18.7 ± 0.5 months; n = 17 Tg [9 male, 8 female], 19 WT [9 male, 10 female]). Mice were housed under a 12-hour light:12-hour dark schedule, and fed standard laboratory chow and water *ad libitum*. Experiments were approved by the Animal Ethics Committee of the Montreal Neurological Institute and McGill University, and were conducted in accordance with the guidelines of the Canadian Council on Animal Care.

2.2 *In vivo* MRI acquisition

Mice were anesthetized with an induction dose of 4-5% sevoflurane and secured in an MRI-compatible bed. All MRI studies were performed under ~2.5-3%

sevoflurane in medical air and animals were allowed to breathe spontaneously without mechanical ventilation. Respiration rate and body temperature was continuously monitored using an MR-compatible system (Small Animal Instruments Inc., Stony Brook, NY) and the temperature was maintained at 37 ± 0.2^{o}C throughout the study using a feedback-regulated warming system (Small Animal Instruments Inc., Stony Brook, NY).

All MR images were obtained from a 7T Bruker Pharmascan system (Bruker Biospin, Ettlingen, Germany) using a 28-mm inner-diameter, quadrature volume resonator (RAPID MR International, Columbus, OH). Following the acquisition of scout images, ROI-based shimming (MAPSHIM, Bruker Biospin) was performed to increase the magnetic field homogeneity within the brain. Anatomical images were acquired using a 3D balanced Steady-State Free Precession (b-SSFP) sequence with matrix size = 128×128×64, field-of-view = 1.8×1.8×0.9 cm, spatial resolution = 140x140×140 μm, number of phase-cycles = 4, and number of averages = 4. The phase-cycled images were combined using the sum-of-squares reconstruction method in order to minimize banding artifacts (Bangerter et al., 2004). Perfusion images were acquired with a customized, 3D pseudo-continuous ASL sequence with matrix size = 64×64×32, field-of-view = 1.8×1.8×0.9 cm, spatial resolution = 280×280×280 μm, and 48 averages. Perfusion labeling was achieved by positioning a 2 mm thick inversion slab in the neck region (~7 mm inferior to the level of the brainstem) and inverting inflowing blood within this slab every 14 ms using spatially-selective sinc radiofrequency (RF) pulses. The entire scanning session lasted approximately 2.5 hours per animal.

2.3 MRI processing

An unbiased, symmetric, customized template was generated from anatomical scans from the 115 mice using an iterative process (Lau et al., 2008; Fonov et al., 2011). Prior to template generation, each reconstructed image volume underwent image non-uniformity correction using the N3 algorithm (Sled et al., 1998), brain masking, and linear spatial normalization utilizing a 12-parameter affine transformation (Collins et al., 1994) to map individual images from native coordinate space to reference space. Briefly, the template generation process involved an iterative (coarse-to-fine resolution) estimation of the nonlinear transformation to match each MRI scan to the evolving average of the population. The final anatomical template (population average) was generated with an isotropic voxel resolution of 0.06 mm (Fig. 1A). This customized template was parcellated into an atlas (Fig. 1B) consisting of 14 cerebral cortical regions per hemisphere, specifically anterior cingulate cortex, auditory cortex, barrel cortex, entorhinal cortex, frontal cortex, insula, motor cortex, perirhinal cortex, piriform cortex, posterior cingulate cortex, retrosplenial cortex, somatosensory cortex 1, somatosensory cortex 2, and visual cortex, using the Montreal Neurological Institute (MNI) McConnell Brain Imaging Centre DISPLAY software package (http://www.bic.mni.mcgill.ca). The masks for the 14 cerebral cortical regions were projected onto a standardized cortical surface template for surface-based region-of-interest (ROI) analysis (Fig. 2).

For cortical thickness measurement, the cortical mask with inside, outside, interhemispheric, and resistive boundaries (Fig. 1B) was nonlinearly registered

from the atlas to each subject. Streamlines running from the inner to outer boundaries of the cortex were defined using Laplace's equation and their length was used as the measure of cortical thickness (Lerch et al., 2008). The mean cortical thickness was computed from an intermediate surface for each of the 14 pre-defined ROIs from the spatially normalized thickness maps.

The control perfusion images were linearly registered to the anatomical images for each mouse in order to compensate for potential, slight movement during the scanning session. Parametric perfusion maps based on the fractional ASL signal, defined as the ratio between the difference [control – labeled] and control images (Lu et al., 2010; Borogovac and Asllani, 2012), were calculated on a voxel-by-voxel basis. The perfusion maps were spatially normalized to reference space using the transformations derived from the anatomical image registration. In order to directly compare cortical thickness and perfusion measures, the perfusion data was projected to the cortical surface by averaging the image intensity along each streamline passing through each vertex. The individual, spatially normalized, perfusion maps were averaged to produce group-mean parametric maps. ROI-based perfusion measures were derived utilizing the surface MRI atlas in reference space.

2.4 Statistical analysis

Statistical analysis was performed using Matlab (Mathworks, Natick, MA, USA) and the SurfStat toolbox (http://www.math.mcgill.ca/keith/surfstat) (Worsley et al., 2009). Linear mixed-effects models using the restricted

maximum likelihood (REML) estimation method were employed to assess group differences and cross-sectional changes (Pinheiro and Bates, 2000). Specifically, a one-way analysis of variance (ANOVA) was employed to assess between-group differences (Tg vs. WT) at each age level (Young, Middle-Aged, Old). For each genotype, a one-way ANOVA was also employed to assess across-age (within-groups, cross-sectional) differences. A two-way ANOVA was utilized to assess the genotype-by-age interaction. Quantitative results of the vertexwise analysis are expressed as statistical parametric maps resulting from post-hoc Student's two-tailed t-tests. The statistical parametric maps are presented without thresholding in order to demonstrate the overall pattern of group differences. For the ROI-based analysis, measures from the left and right hemispheres were combined in order to maximize statistical power, and quantitative results are expressed as mean ± standard deviation of the effect of interest (between-groups and cross-sectional within-groups differences). The ROI-based data was adjusted for multiple comparisons using the Bonferroni correction.

3. Results

3.1 APP transgenic and wild-type mice exhibit age-related differences in regional cortical thickness

A globally increased mean cortical thickness was identified in the Young Tg mice compared to Young WT mice (Fig. 3). The ROI-based analysis (Fig. 3) demonstrated that the cortical thickness difference (Tg > WT) in the Young Tg mice was significant ($P < 0.05$) in all regions examined, except for the barrel cortex, motor cortex, and somatosensory cortex 1, which did not survive correction for multiple comparisons. This difference was greatest in the perirhinal cortex (t = 6.2, $P < 0.001$), posterior cingulate cortex (t = 5.1, $P < 0.001$), insula (t = 4.9, $P < 0.001$), and entorhinal cortex (t = 4.4, $P < 0.001$). The vertexwise t-statistic maps (Fig. 4) revealed the spatial heterogeneity of cortical thickness differences between Young Tg and WT mice.

The Tg mice showed greater thinning across the entire cortex over 15 months than the WT mice (Fig. 5A). For both Tg and WT group, minimal change in cortical thickness was observed over the 15 month timeframe in the anterior/posterior cingulate and retrosplenial cortical regions (Fig. 6 and 7A). The remaining cortical regions demonstrated cortical thinning in both groups with greater reduction in cortical thickness (*i.e.* atrophy) in the Tg relative to WT mice (Fig. 6 and 7A). While most of these regions demonstrated significant differences in the age-by-genotype interaction at 15 months without Bonferroni correction (entorhinal cortex: $P_{\text{uncorrected}} = 0.004$; perirhinal cortex: $P_{\text{uncorrected}} = 0.016$; motor cortex: $P_{\text{uncorrected}} = 0.008$;

piriform cortex: $P_{uncorrected} = 0.024$), the significance did not survive multiple comparisons. The Tg group had a higher variability than the WT group likely resulting from the heterogeneity of disease progression in this model.

3.2 Transgenic mice demonstrate profound regional cortical hypoperfusion and distinct spatio-temporal patterns relative to wild-type mice

The Young Tg mice demonstrated statistically significant ($P < 0.05$) hypoperfusion in all cortical regions (Fig. 4B and 8). The most significant differences were observed in perirhinal cortex ($t = 6.8$, $P < 0.001$), retrosplenial cortex ($t = 6.0$, $P < 0.001$), entorhinal cortex ($t = 5.8$, $P < 0.001$), and posterior cingulate cortex ($t = 5.7$, $P < 0.001$), which are the same regions that demonstrated the greatest differences in cortical thickness. All cortical regions remained significantly hypoperfused in the Middle-Aged and Old Tg mice relative to the age-matched WT mice.

The change in cortical perfusion over 15 months across the whole cortex did not demonstrate a significant difference between genotypes (Fig. 5B). However, analysis of the vertexwise and regional changes revealed striking differences between Tg and WT mice (Fig. 7B and 9), indicating the importance of examining loco-regional changes which are often obscured in global measures. The regions along the rhinal fissure, including insula ($P_{uncorrected} = 0.007$), perirhinal cortex ($P_{uncorrected} = 0.004$), and entorhinal cortex ($P_{uncorrected} = 0.036$), displayed an increasing level of perfusion over 15 months in the Tg mice, while stable or decreasing perfusion was observed in

the WT mice. While these regions demonstrated significant differences prior to Bonferroni correction, this significance did not survive multiple comparisons. Although significant group differences were not identified in the other ROIs, regional heterogeneity was readily apparent.

4. Discussion

In this work, we have examined the spatio-temporal patterns of cortical thickness and resting perfusion derived from *in vivo* MRI scans of APP Tg and age-matched WT mice. This study represents the first demonstration of the regional effects of APP overexpression on both cortical structure and cerebrovascular physiology across the mouse lifespan derived from non-invasive MRI data. A striking feature of our data is the spatial and temporal heterogeneity of morphometric and functional alterations. Regional differences in cortical thickness and CBF are well-documented in human MRI studies of AD subjects (Lerch et al., 2005; Tosun et al., 2010; J.J. Chen et al., 2011), which motivated our approach to explore pathological alterations in mouse brain using fully-automated processing and vertexwise/ROI-based analysis.

The observation of increased cortical thickness in the young Tg was unexpected and seemingly counterintuitive. However, several studies support potential mechanisms for this finding. Plaschke et al. (1997) demonstrated that long-term cerebral hypoperfusion resulted in increased regional concentrations of APP in a rat model. Oh et al. (2009) demonstrated that overexpression of mutant (APP_{swe}) or wild-type APP in transgenic mice can induce hypertrophy of cortical neurons. Iacono et al. (2009) identified hypertrophic cortical neurons in human autopsy material from the Nun Study and postulated that neuronal hypertrophy may constitute an early cellular response to AD pathology and/or reflect compensatory mechanisms

that prevent cognitive impairment despite substantial AD-associated pathological changes. Astrogliosis is also prominent in AD and has been associated with a specific cortical laminar pattern (Beach et al., 1989). Hence, APP/β-amyloid-driven neuronal hypertrophy and/or astrogliosis could potentially explain the apparent increase in cortical thickness in the Tg mice. Future studies could assess cortical structure in even younger (*e.g.* 1 month-old) mice in order to investigate the age-of-onset of these pathological processes.

The regions along the interhemispheric and rhinal fissures demonstrated the most significant differences in cortical thickness between young Tg and WT mice. These areas are associated with limbic, memory, and human default-mode network (DMN)-type functions, which are affected in AD. It is possible that the high constitutive activity of these regions may result in early pathological changes (Buckner et al., 2009; Bero et al., 2011). Although all of these spatially remote regions demonstrate increased thickness in young Tg mice, the regions along the interhemispheric fissure do not appear to appreciably atrophy over time, while the areas along the rhinal fissure display the greatest rate of cortical thinning. It is possible that the midline regions are more resilient than other brain regions (Driscoll and Troncoso, 2011).

Our cortical perfusion data also demonstrated heterogeneous spatial and temporal patterns. Most areas of the brain were hypoperfused in the young Tg mice. Our data from *in vivo* ASL MRI is consistent with the

observations of Niwa et al. (2002) who identified reduced CBF in young (2-3 month-old) APP Tg 2123 and 2576 mice by quantitative autoradiography. Given that mice in the Niwa study and our study do not yet exhibit amyloid plaques, soluble β-amyloid may be responsible for altered blood flow. Han et al. (2008) utilized digital video microscopy to demonstrate that soluble β-amyloid is a major contributor to age-dependent cerebrovascular dysfunction in Tg2576 mice. Future studies could employ BACE1 or γ-secretase inhibitors to support the role of soluble β-amyloid in the perfusion deficits observed in the young mice (without plaques and cerebral amyloid angiopathy) in our study.

In addition to differences in the temporal evolution of changes in cortical thickness between the regions along the interhemispheric and rhinal fissures, these two groups of structures also demonstrated distinct patterns of age-related perfusion changes. While the anterior/posterior cingulate and retrosplenial cortical areas showed perfusion changes (decreases) similar to WT mice, the insula and perirhinal/entorhinal regions demonstrated increased perfusion over time in Tg mice. A potential mechanism that would explain this observation includes increased local vascular density resulting from long-term angiogenesis (Desai et al., 2009). Dai et al. (2009) observed increases in regional CBF in portions of the limbic system in mild cognitive impairment (MCI) and AD subjects using ASL MRI, and suggested a compensatory cellular and/or vascular process. The apparent inverse relationship between temporal changes in cortical thickness and perfusion in

these regions is particularly intriguing and it warrants further investigation into the mediators of these processes. As suggested by Dai et al. (2009), brain structural and functional changes may be asynchronous during disease evolution. To this end, animal model studies should provide new insights into findings in human AD multi-modality neuroimaging studies.

A potential confound of the perfusion data in this study is the use of anesthesia during MRI scanning. Inhaled anesthetic agents are known vasodilators and increased CBF has been demonstrated in rats under isoflurane (Sicard et al., 2003). Lenz et al. (1998) demonstrated that sevoflurane produces less CBF increase than isoflurane, and Flores et al. (2008) determined that sevoflurane is preferred for physiologic imaging in mice. Based on the literature and our own experience, we performed these studies under sevoflurane. To date, all ASL MRI and the majority of other, non-terminal, cerebrovascular physiology (*e.g.* laser Doppler flowmetry [LDF]) studies in mice have been performed under anesthesia and it is unknown if our observed genotype- and age-related group differences in cortical perfusion are influenced by the anesthetic agent. Although imaging of awake animals may be preferable from a physiological perspective, minimizing the effects of motion is a primary concern for these sensitive MRI scans. While Desai et al. (2010) recently reported the feasibility of optogenetic fMRI studies in awake mice, and Mizuma et al. (2010) described PET studies in conscious mice, the use of a head-post for immobilization is impractical for long-term studies and the requirements for customized

surface RF coils may limit accurate assessment of subcortical structures. Our group is currently investigating non-invasive methods for head restraint which will facilitate perfusion and functional MRI studies of conscious mice.

A limitation of this study is the cross-sectional design. This particular strategy was employed given that the ultimate objective of our work is correlation between temporally-matched neuroimaging and neuropathology data. Longitudinal studies, which may potentially reveal more subtle group (genotype, age) differences, are being initiated in our lab. This study, like most AD mouse model studies, also focused on a single mouse line. Future studies should examine other APP Tg mouse models in order to better assess the generalizability of our results.

Substantial insight into the pathophysiological processes driving the distinct patterns of abnormal neuroanatomical structure and cerebrovascular physiology can potentially be gained by intervention with putative "disease-modifying" therapeutic agents with different mechanisms-of-action (*e.g.* amyloid-clearing biologics, amyloid-lowering secretase inhibitors, neuroprotective agents, neuroinflammation modulators). The non-invasive nature of 3D MRI scanning provides a distinct advantage over other techniques (*e.g.* autoradiography, LDF) for therapeutic studies, as it allows for longitudinal assessment of structural and physiological changes across the entire brain. Effective translation of knowledge gleaned from such pre-clinical imaging studies should facilitate the development of effective treatments to delay, slow, halt, and/or reverse the progression of AD.

5. Funding

This work was supported by the Canadian Institutes of Health Research (Operating Grant MOP-93795 to B.J.B.).

6. Disclosure statement

The authors have no conflicts of interest relevant to the subject of this manuscript, including no institutional contracts relating to this research or any other agreements of the authors or their institutions that could be seen as involving a financial interest in this work.

7. Acknowledgements

We are grateful to Drs. Simone Zehntner and Alex Zijdenbos (Biospective Inc., Montreal, QC, Canada) for their invaluable contributions to the MR image processing, and Dr. Felix Carbonell (Biospective Inc., Montreal, QC, Canada) for assistance with the statistical analysis. We thank Dr. Lennart Mucke and the Gladstone Institutes for use of the J20 APP mice. We also thank Antonio Aliaga and Kung-Yuan Lin for acquisition of the MRI data.

8. References

Alsop, D.C., Dai, W., Grossman, M., Detre, J.A., 2010. Arterial spin labeling blood flow MRI: its role in the early characterization of Alzheimer's disease. J. Alzheimer Dis. 20, 871-80.

Badea, A., Johnson, G.A., Jankowsky, J.L., 2010. Remote sites of structural atrophy predict later amyloid formation in a mouse model of Alzheimer's disease. NeuroImage. 50, 416-27.

Bangerter, N.K., Hargreaves, B.A., Vasanawala, S.S., Pauly, J.M., Gold, G.E., Nishimura, D.G., 2004. Analysis of multiple-acquisition SSFP. Magn. Reson. Med. 51, 1038-47.

Beach, T.G., Walker, R., McGeer, E.G., 1989. Patterns of gliosis in Alzheimer's disease and aging cerebrum. Glia. 2, 420-36.

Bero, A.W., Yan, P., Roh, J.H., Cirrito, J.R., Stewart, F.R., Raichle, M.E., Lee, J.M., Holtzman, D.M., 2011. Neuronal activity regulates the regional vulnerability to amyloid-B deposition. Nat. Neurosci. 14, 750-6.

Borogovac, A., Asllani, I., 2012. Arterial spin labeling (ASL) fMRI: advantages, theoretical constrains and experimental challenges in neurosciences. Int. J. Biomed. Imaging, 2012: 818456, doi:10.1155/2012/818456.

Buckner, R.L., Sepulcre, J., Talukdar, T., Krienen, F.M., Liu, H., Hedden, T., Andrews-Hanna, J.R., Sperling, R.A., Johnson, K.A., 2009. Cortical hubs revealed by intrinsic functional connectivity: mapping, assessment of stability, and relation to Alzheimer's disease. J. Neurosci. 29, 1860-73.

Chao, L.L., Buckley, S.T., Kornak, J., Schuff, N., Madison, C., Yaffe, K., Miller, B.L., Kramer, J.H., Weiner, M.W., 2010. ASL perfusion MRI predicts cognitive decline and conversion from MC to dementia. Alzheimer Dis. Assoc. Disord. 24, 19-27.

Chen, J.J., Rosas, H.D., Salat, D.H., 2011. Age-associated reductions in cerebral blood flow are independent from regional atrophy. NeuroImage. 55, 468-78.

Chen, Y., Wolk, D.A., Reddin, J.S., Korcykowski, M., Martinez, P.M., Musiek, E.S., Newberg, A.B., Julin, P., Arnold, S.E., Greenberg, J.H., Detre, J.A., 2011. Voxel-level comparison of arterial spin-labeled perfusion MRI and FDG-PET in Alzheimer disease. Neurology. 77, 1977-95.

Collins, D.L., Neelin, P., Peters, T.M., Evans, A.C., 1994. Automatic 3D inter-subject registration of MR volumetric data in standardized Talairach Space. J. Comput. Assist. Tomogr. 18, 192-205.

Dai, W., Lopez, O.L., Carmichael, O.T., Becker, J.T., Kuller, L.H., Gach, H.M., 2009. Mild cognitive impairment and Alzheimer disease: patterns of altered cerebral blood flow at MR imaging. Radiology. 250, 856-66.

Delatour, B., Guegan, M., Volk, A., Dhenain, M., 2006. In vivo and histological evaluation of brain atrophy in APP/PS1 transgenic mice. Neurobiol. Aging. 27, 835-47.

Desai, B.S., Schneider, J.A., Li, J.L., Carvey, P.M., Hendy, B., 2009. Evidence of angiogenic vessels in Alzheimer's disease. J. Neural. Transm. 116, 587-97.

Desai, M., Kahn, I., Knoblich, U., Bernstein, J., Atallah, H., Yang, A., Kopell, N., Buckner, R.L., Graybiel, A.M., Moore, C.I., Boyden, E.S., 2010. Mapping brain networks in awake mice using combined optical neural control and fMRI. J. Neurophysiol. 105, 1393-1405.

Driscoll, I., Troncoso, J., 2011. Asymptomatic Alzheimer's disease: a prodrome or a state of resilience. Curr. Alzheimer. Res. 8, 330-5.

Faure, A., Verret, L., Bozon, B., El Tannir El Tayara, N., Ly, M., Kober, F., Dhenain, M., Rampon, C., Delatour, B., 2011. Impaired neurogenesis, neuronal loss, and brain function deficits in the APPxPS1-Ki mouse model of Alzheimer's disease. Neurobiol. Aging. 32, 407-18.

Flores, J.E., McFarland, L.M., Vanderbilt, A., Ogasawara, A.K., Williams, S-P., 2008. The effects of anesthetic agent and carrier gas on blood glucose and tissue uptake in mice undergoing dynamic FDG-PET imaging: sevoflurane and isoflurane compared in air and in oxygen. Mol. Imaging. Biol. 10, 192-200.

Fonov, V., Evans, A.C., Botteron, K., Almli, C.R., McKinstry, R.C., Collins, D.L., 2011. Unbiased average age-appropriate atlases for pediatric studies. NeuroImage. 54, 313-27.

Han, B.H., Zhou, M-L., Abousaleh, F., Brendza, R.P., Dietrich, H.H., Koenigsknecht-Talboo, J., Cirrito, J.R., Milner, E., Holtzman, D.M., Zipfel, G.J., 2008. Cerebrovascular dysfunction in amyloid precursor protein transgenic mice: contribution of soluble and insoluble amyloid-B peptide, partial restoration via γ -secretase inhibition. J. Neurosci. 28, 13542-50.

Iacono, D., Markesbery, W.R., Gross, M., Pletnikova, O., Rudow, G., Zandi, P., Troncoso, J.C., 2009. The Nun Study: clinically silent AD, neuronal hypertrophy, and linguistic skills in early life. Neurology. 73, 665-73.

Jack, C.R. Jr., Bernstein, M.A., Borowski, B.J., Gunter, J.L., Fox, N.C., Thompson, P.M., Schuff, N., Krueger, G., Killiany, R.J., DeCarli, C.S., Dale, A.M., Weiner, M.W., and the Alzheimer's Disease Neuroimaging Initiative, 2010. Update on the MRI core of the Alzheimer's Disease Neuroimaging Initiative. Alzheimers Dement. 5, 212-20.

Lau, J.C., Lerch, J.P., Sled, J.G., Henkelman, R.M., Evans, A.C., Bedell, B.J., 2008. Longitudinal neuroanatomical changes determined by deformation-based morphometry in a mouse model of Alzheimer's disease. NeuroImage. 42, 19-27.

Lenz, C., Rebel, A., van Ackern, K., Kuschinsky, W., Waschke, K.F., 1998. Local cerebral blood flow, local cerebral glucose utilization, and flow-metabolism coupling during sevoflurane versus isoflurane anesthesia in rats. Anesthesiology. 89, 480-8.

Lerch, J.P., Pruessner, J.C., Zijdenbos, A., Hampel, H., Teipel, S.J., Evans, A.C., 2005. Focal decline of cortical thickness in Alzheimer's disease identified by computational neuroanatomy. Cereb. Cortex. 15, 995-1001.

Lerch, J.P., Carroll, J.B., Dorr, A., Spring, S., Evans, A.C., Hayden, M.R., Sled, J.G., Henkelman, R.M., 2008. Cortical thickness measured from MRI in the YAC128 mouse model of Huntington's disease. NeuroImage. 41, 243-51.

Lin, A.-L., Laird, A.R., Fox, P.T., Gao, J.-H., 2012. Multimodal MRI neuroimaging biomarkers for cognitive normal adults, amnestic mild cognitive impairment, and Alzheimer's disease. Neurol. Res. Int. 2012, 907409, doi:10.1155/2012/907409.

Lu, H., Leoni, R., Silva, A.C., Stein, E.A., Yang, Y., 2010. High field continuous arterial spin labeling (CASL) with long labeling duration: reduced confounds from blood transit time and post-labeling delay. Magn. Reson. Med. 64, 1557-66.

Maheswaran, S., Barjat, H., Rueckert, D., Bate, S.T., Howlett, D.R., Tilling, L., Smart, S.C., Pohlmann, A., Richardson, J.C., Hartkens, T., Hill, D.L., Upton, N., Hajnal, J.V., James, M.F., 2009. Longitudinal regional brain volume changes quantified in normal aging and Alzheimer's APP x PS1 mice using MRI. Brain. Res. 1270, 19-32.

Massad, C.A., Amin, S.K., Hu, L., Mei, Y., Klann, E., Pautler, R.G., 2010. Mitochondrial superoxide contributes to blood flow and axonal transport deficits in the Tg2576 mouse model of Alzheimer's disease. PLoS ONE. 5, e10561, doi:10.1371/journal.pone.0010561.

Mizuma, H., Shukuri, M., Hayashi, T., Watanabe, Y., Onoe, H,. 2010. Establishment of in vivo brain imaging method in conscious mice. J. Nucl. Med. 51, 1068-75.

Mosconi, L., Berti, V., Blodzik, L., Pupi, A., De Santi, S., de Leon, M.J., 2010. Pre-clinical detection of Alzheimer's disease using FDG-PET, with or without amyloid imaging. J. Alzheimer Dis. 20, 843-54.

Mosconi, L., McHugh, P.F., 2011. FDG- and amyloid-PET in Alzheimer's disease: is the whole greater than the sum of the parts? Q. J. Nucl. Mol. Imaging. 55, 250-64.

Mucke, L., Masliah, E., Yu, G.Q., Mallory, M., Rockenstein, E.M., Tatsuno, G., Hu, K., Kholodenko, D., Johnson-Wood, K., McConlogue, L., 2000. High-level neuronal expression of Aβ1–42 in wild-type human amyloid protein precursor Tg mice: synaptotoxicity without plaque formation. J. Neurosci. 20, 4050–8.

Niwa, K., Kazama, K., Younkin, S.G., Carlson, G.A., Iadecola, C., 2002. Alterations in cerebral blood flow and glucose utilization in mice overexpressing the amyloid precursor protein. Neurobiol. Dis. 9, 61-8.

Oberg, J., Spenger, C., Wang, F.-H., Andersson, A., Westman, E., Skoglund, P., Sunnemark, D., Norinder, U., Klason, T., Wahlund, L.O., Lindberg, M., 2008. Age related changes in brain metabolites observed by ^{1}H MRS in APP/PS1 mice. Neurobiol. Aging. 29, 1423-33.

Oh, E.S., Savonenko, A.V., King, J.F., Tucker, S.M.F., Rudow, G.L., Xu, G., Borchelt, D.R., Troncoso, J.C., 2009. Amyloid precursor protein increases cortical neuron size in transgenic mice. Neurobiol. Aging. 30, 1238-44.

Palop, J.J., Jones, B., Kekonius, L., Chin, J., Yu, G.Q., Raber, J., Masliah, E., Mucke, L., 2003. Neuronal depletion of calcium-dependent proteins in the dentate gyrus is tightly linked to Alzheimer's disease-related cognitive deficits. Proc. Natl. Acad. Sci. USA. 100, 9572-77.

Pinheiro, J.C., Bates, D.M., 2000. Mixed-effects models in S and S-PLUS. Springer, New York.

Plaschke, K., Ranneberg, T., Bauer, J., Weigand, M., Hoyer, S., Bardenheuer, H.J., 1997. The effect of stepwise cerebral hypoperfusion on energy metabolism and amyloid precursor protein (APP) in cerebral cortex and hippocampus in the adult rat. Ann. NY Acad. Sci. 826, 502-6.

Poisnel, G., Hérard, A-S., El Tannir El Tayara, N., Bourrin, E., Volk, A., Kober, F., Delatour, B., Delzescaux, T., Debeir, T., Rooney, T., Benavides, J., Hantraye, P., Dhenain, M., 2012. Increased regional cerebral glucose uptake in an APP/PS1 model of Alzheimer's disease. Neurobiol. Aging. 33, 1995-2005.

Sicard, K., Shen, Q., Brevard, M.E., Sullivan, R., Ferris, C.F., King, J.A., Duong, T.Q., 2003. Regional cerebral blood flow and BOLD responses in conscious and anesthestized rats under basal and hypercapnic conditions: implications for functional MRI studies. J. Cereb. Blood Flow Metab. 23, 472-81.

Sled, J.G., Zijdenbos, A.P., Evans, A.C., 1998. A nonparametric method for automatic correction of intensity nonuniformity in MRI data. IEEE Trans. Med. Imaging. 17, 87-97.

Tong, X.-K., Nicolakakis, N., Kocharyan, A., Hamel, E., 2005. Vascular remodeling versus amyloid β-induced oxidative stress in the cerebrovascular dysfunctions associated with Alzheimer's disease. J. Neurosci. 25, 11165-74.

Tosun, D., Mojabi, P., Weiner, M.W., Schuff, N., 2010. Joint analysis of structural and perfusion MRI for cognitive assessment and classification of Alzheimer's disease and normal aging. NeuroImage. 52, 186-97.

Weidensteiner, C., Metzger, F., Bruns, A., Bohrmann, B., Kuennecke, B., von Kienlin, M., 2009. Cortical hypoperfusion in the B6.PS2APP mouse model for Alzheimer's disease: comprehensive phenotyping of vascular and tissular parameters by MRI. Magn. Reson. Med. 62, 35-45.

Worsley, K.J., Taylor, J.E., Carbonell, F., Chung, M.K., Duerden, E., Bernhardt, B., Lyttelton, O., Boucher, M., Evans, A.C., 2009. SurfStat: a Matlab toolbox for the statistical analysis of univariate and multivariate surface and volumetric data using linear mixed effects models and random field theory. Proceedings of the 15th Annual Meeting of the Organization for Human Brain Mapping, San Francisco, CA, USA.

Figures

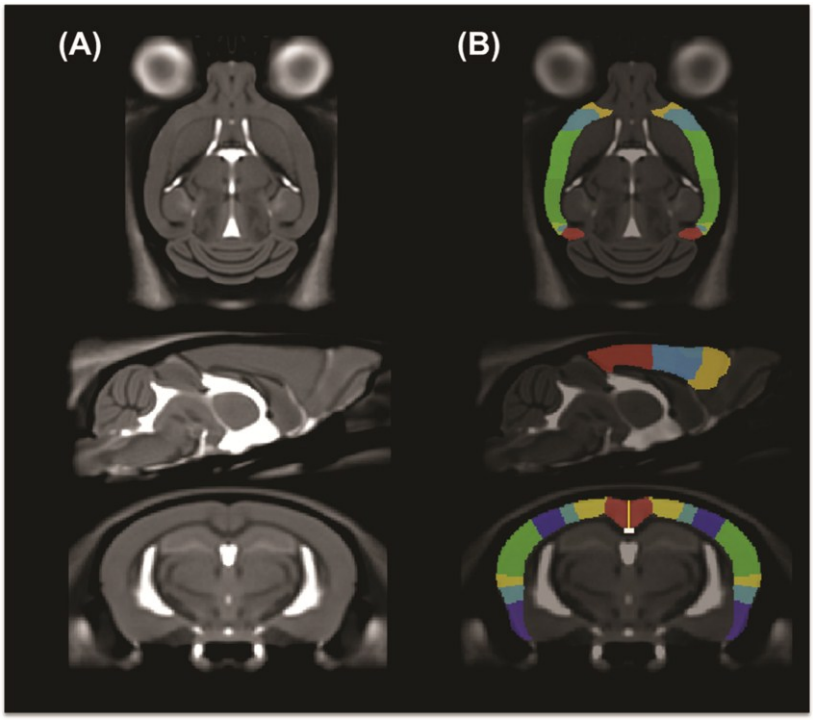

Figure 1 Orthogonal views (axial, sagittal, and coronal, top-to-bottom, respectively) of the anatomical template (**A**) and the parcellated cortical atlas (B). Note the interhemispheric boundary (yellow line) and resistive boundary (white line) used for cortical thickness measurement in (B). The anatomical template was derived from all 115 available scans and the atlas included 14 cortical regions.

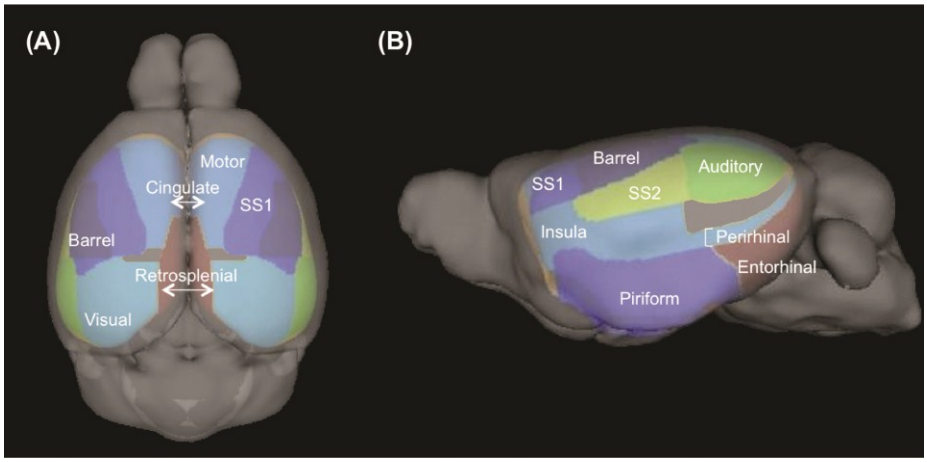

Figure 2 Superior (A) and lateral (B) views of the cortical surface atlas with 14 ROI labels.

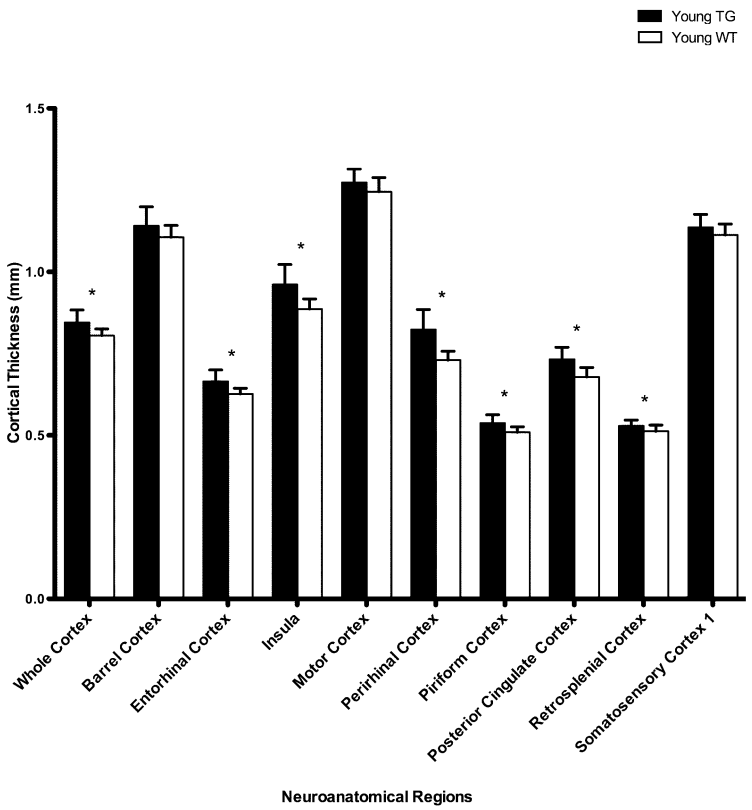

Figure 3 MRI cortical thickness measures from representative ROIs in Young Tg and WT mouse groups. Note that the whole cortex and the majority of regions demonstrated a greater cortical thickness in Tg mice compared to age-matched WT mice. For the sake of clarity, not all ROIs have been included. The remaining ROIs demonstrated the following behavior: anterior cingulate cortex was similar to posterior cingulate cortex, auditory and visual cortices were similar to motor cortex, somatosensory cortex 2 was similar to somatosensory cortex 1, and frontal cortex was similar to entorhinal cortex. * indicates $P < 0.05$.

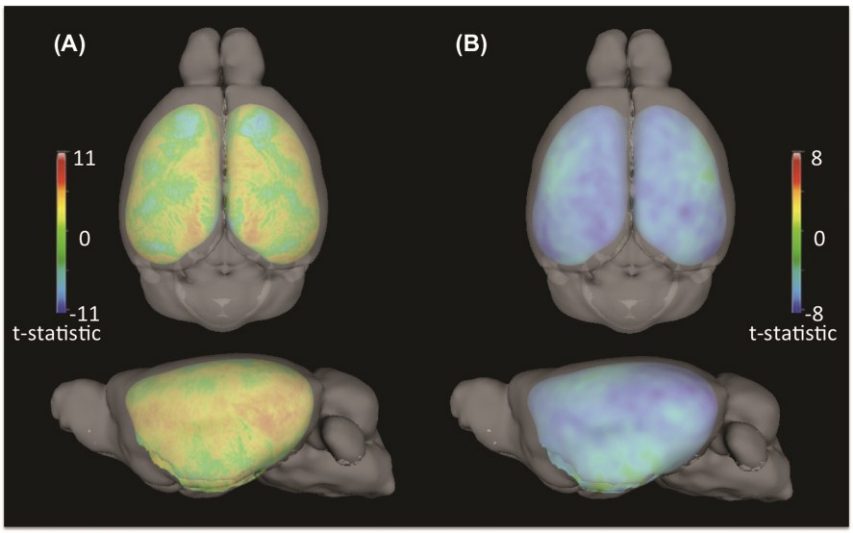

Figure 4 Genotype group differences (Tg - WT) in cortical thickness (**A**) and perfusion (**B**) in young (~3 month-old) mice. These t-statistic maps demonstrate that the young Tg mice have increased regional cortical thickness (positive values) and decreased cerebral perfusion (negative values) relative to WT mice prior to β-amyloid deposition. Note the relative symmetry in the cortical thickness and perfusion data between the left and right hemispheres. While these maps suggest a potential negative association between loco-regional thickness and perfusion data, a significant relationship was not found.

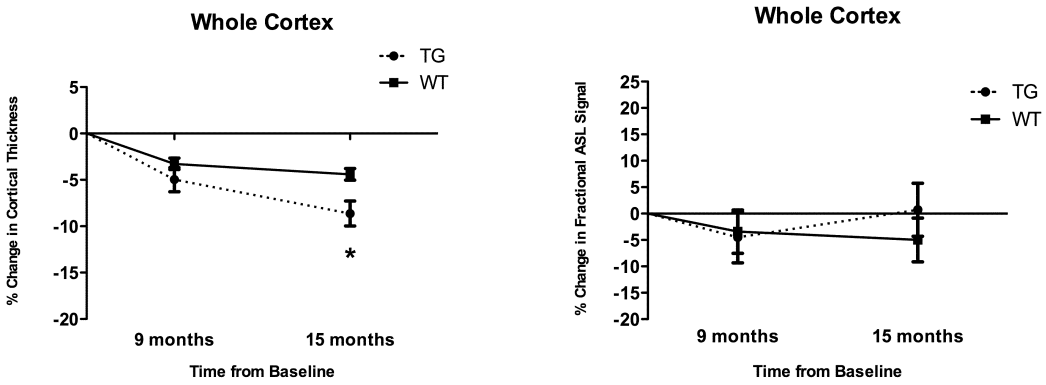

Figure 5 Cortical thickness (A) and cortical perfusion (B) change (% change relative to Young mouse group) of whole cortex over 15 months in Tg and WT mice. The whole cortex showed increased cortical thinning rate in Tg mice relative to WT mice, which was statistically significant over 15 months. There was no significant difference in the rate of whole cortex perfusion change across genotypes. * indicates $P < 0.05$.

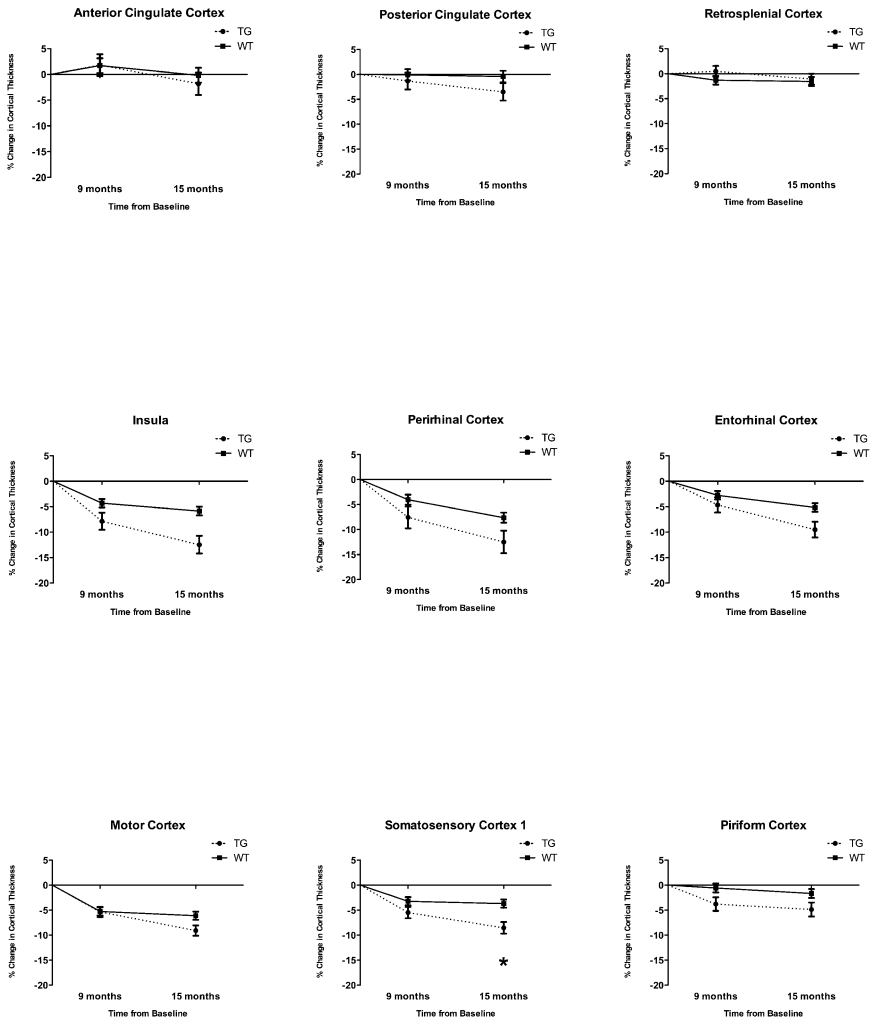

Figure 6 Cortical thickness change (% change relative to Young mouse group) over 15 months in Tg and WT mice. The anterior/posterior cingulate and retrosplenial cortical regions did not show appreciable change over time. In contrast, Tg mice demonstrated a greater rate of cortical thinning than age-matched WT mice in the remaining regions. For the sake of clarity, not all ROIs have been included. The remaining ROIs demonstrated the following behavior: auditory, barrel, and somatosensory 2 cortices were similar to somatosensory cortex 1, visual cortex was similar to motor cortex, and frontal cortex was similar to entorhinal cortex. * indicates $P < 0.05$.

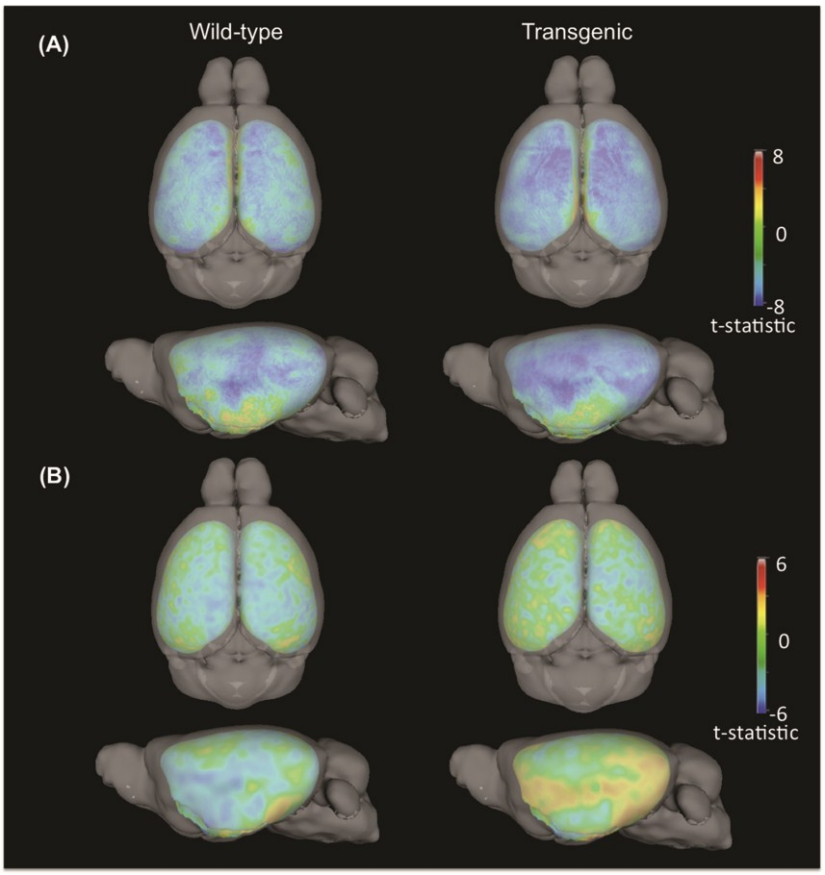

Figure 7 Changes in cortical thickness (**A**) and perfusion (**B**) between Young (~3 month-old) and Old (~18 month-old) mice. These t-statistic maps demonstrate that Tg mice underwent a greater rate of local cortical thinning (negative values), relative to WT mice, over a 15 month period (A). The maps of change in cortical perfusion (B) reveal increasing blood flow (positive values) along the rhinal fissure, including insular, perirhinal, and entorhinal cortex, in the Tg mice, while decreasing perfusion (negative values) in these regions was apparent in the WT mice.

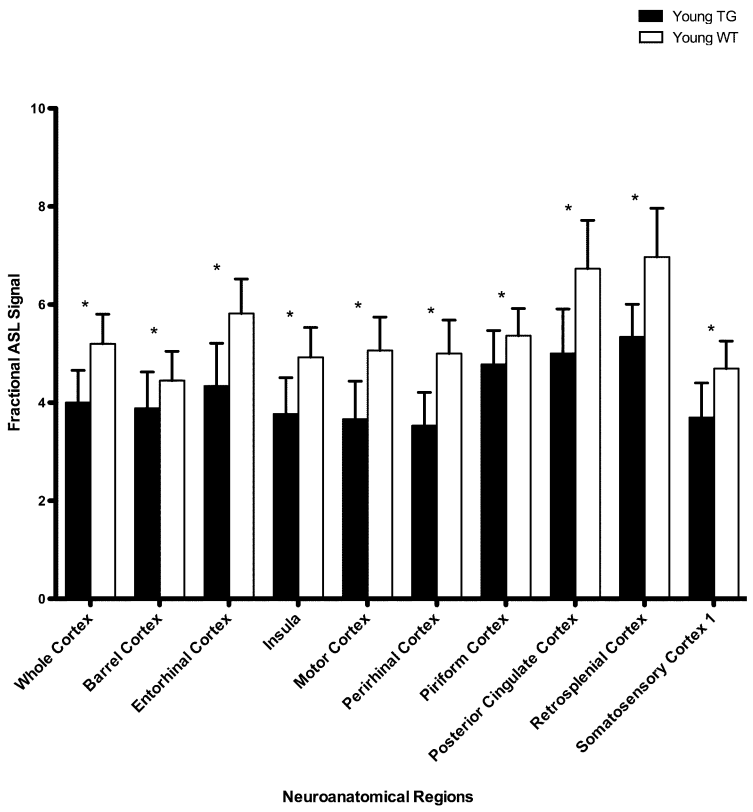

Figure 8 ASL perfusion MRI measures from representative ROIs in Young Tg and WT mice. Note that the whole cortex and the majority of regions demonstrated significantly lower perfusion in Tg mice compared to age-matched WT mice. For the sake of clarity, not all ROIs have been included. The remaining ROIs demonstrated the following behavior: sensory regions (auditory, visual and somatosensory 2 cortices) were similar to motor cortex, anterior cingulate was similar to posterior cingulate cortex, and frontal cortex was similar to entorhinal cortex. * indicates $P < 0.05$.

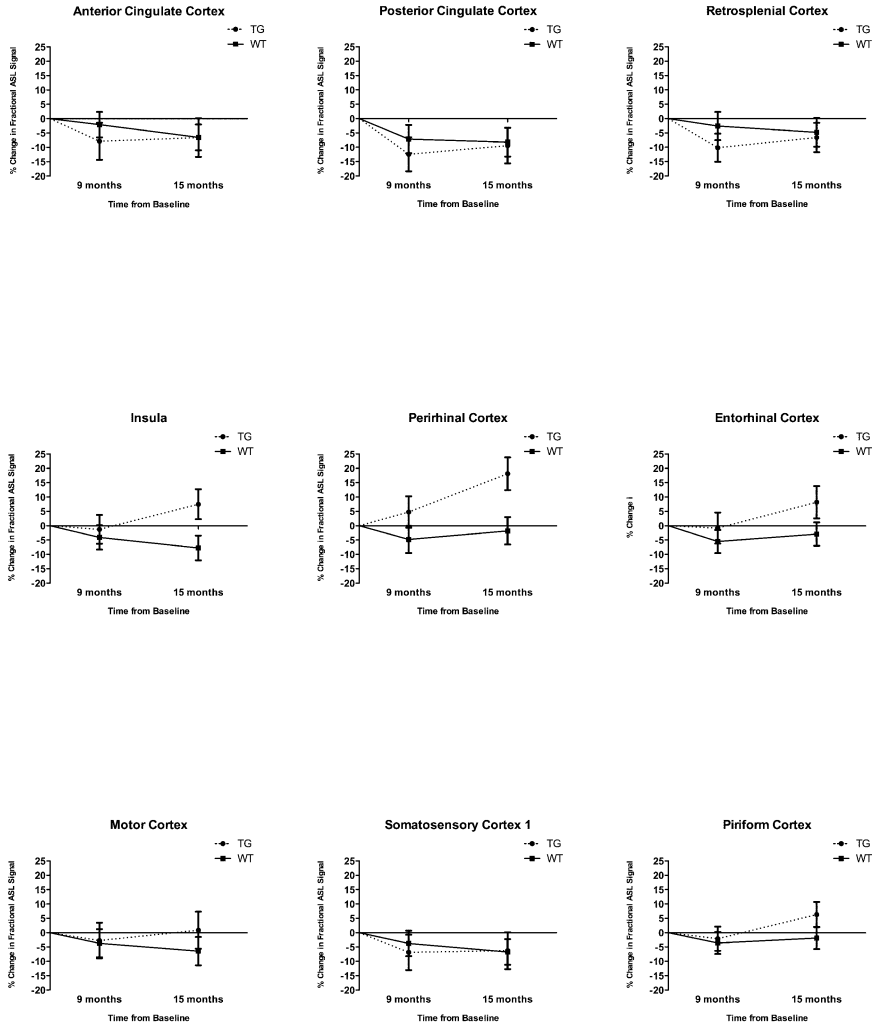

Figure 9 Cortical perfusion change (% change relative to Young mouse group) over 15 months in Tg and WT mice. The midline regions (anterior/posterior cingulate and retrosplenial cortices) and somatosensory 1 cortex showed similar decreases in perfusion over time in Tg and WT groups. In the insular, perirhinal, and entorhinal cortical regions, the Tg mice showed increasing perfusion over time in contrast to the WT group. For the sake of clarity, not all ROIs have been included. The remaining ROIs demonstrated the following behavior: auditory cortex was similar to motor cortex, barrel, somatosensory 2 and visual cortices were similar to somatosensory cortex 1, and frontal cortex was similar to entorhinal cortex. * indicates $P < 0.05$.

Preface to Chapter 8

In the article described in the previous chapter, we found an intriguing and unexpected cortical thickness difference between the Tg and WT groups at 3 months-old, where the cortex of Tg animals was regionally thicker. These findings motivated us to assess cortical thickness at an earlier time point in order to investigate possible aberrant cortical thickness changes. We acquired structural MRI scans at 1 and 3 months-of-age. We then correlated the *in vivo* MRI-derived cortical thickness measures with *post-mortem* quantitative maps of amyloid plaque deposition from a cohort of 18 month-old Tg mice. The following paper has been published to *Neurobiology of Disease* (Grand'Maison et al., 2013).

Contributions of Authors

In the following manuscript, *"Early cortical thickness changes predict beta-amyloid deposition in a mouse model of Alzheimer's disease"*, I, Marilyn Grand'Maison (MGM), am first author, with co-authors Simone P. Zehntner (SPZ), Ming-Kai Ho (MKH), François Hébert (FH), Andrew Wood (AW), Felix Carbonell (FC), Alex P. Zijdenbos, Edith Hamel (EH) and Barry J. Bedell (BJB). This project was supervised and funded by BJB. EH provided the required transgenic animals as a collaborator at the Montreal Neurological Institute. SPZ, AW, FH, MKH, APZ and I produced the reconstructed amyloid 3D maps and surface projections. BJB wrote the MRI sequences employed for structural MRI acquisition. MH and I coordinated the project. FC and I performed the statistical analysis. BJB and I wrote the manuscript, and BJB is the corresponding author.

Chapter 8

Title: Early cortical thickness changes predict beta-amyloid deposition in a mouse model of Alzheimer's disease

Running Title: Cortical thickness and beta-amyloid in AD mice

Authors: Marilyn Grand'Maison[a], Simone P. Zehntner[b], Ming-Kai Ho[a], François Hébert[b], Andrew Wood[b], Felix Carbonell[b], Alex P. Zijdenbos[b], Edith Hamel[a], Barry J. Bedell[a, b]

[a]Department of Neurology & Neurosurgery, Montreal Neurological Institute, McGill University, 3801 University Street, Montreal, QC, Canada H3A 2B4
marilyn.grandmaison@mail.mcgill.ca
ming.ho@mcgill.ca
edith.hamel@mcgill.ca
barry.bedell@mcgill.ca

[b]Biospective Inc., 6100 avenue Royalmount, Montreal, QC, Canada H4P 2R2

simone@biospective.com
francois@biospective.com
andrew@biospective.com
felix@biospective.com
alex@biospective.com

Corresponding Author:

Barry J. Bedell, M.D., Ph.D.
Montreal Neurological Institute, McGill University
3801 University Street
Montreal, Quebec, H3A 2B4
Canada
Phone: 514-398-8804
Fax: 514-398-6547
E-mail: barry.bedell@mcgill.ca

Abstract

Magnetic resonance imaging (MRI) studies have identified aberrant cortical structure in Alzheimer's disease (AD). The association between MRI-derived cortical morphometry measures and β-amyloid, however, remains poorly understood. In this study, we explored the potential relationship between early alterations in cortical thickness and later stage β-amyloid deposition, using a novel approach, in a transgenic AD mouse model. We acquired longitudinal anatomical MRI scans from mutant amyloid precursor protein (APP) transgenic mice and age-matched wild-type mice at 1 and 3.5 months-of-age, and employed fully-automated image processing methods to derive objective, quantitative measures of cortical thickness on a region-of-interest basis. We also generated 3D quantitative immunohistochemistry (qIHC) volumes of deposited β-amyloid burden from 18 month-old transgenic mice using an automated, production-level process. These studies revealed thinner cortex in most regions in the 1 month-old transgenic mice relative to age-matched wild-types, with the exception of the frontal, perirhinal/entorhinal, posterior cingulate, and retrosplenial cortical regions. Betweeen 1 and 3.5 months-of-age, the transgenic mice demonstrated stable or increasing cortical thickness, while the wild-type mice showed cortical thinning. Based on data from co-registered 3D MRI and qIHC volumes, we identified an association between abnormal, early, regional cortical thickness change over 2.5 months and later β-amyloid deposition. These observations suggest that the spatio-temporal pattern of early (pre-plaque) alterations in cerebral cortical structure is indicative of regional predisposition to later β-amyloid pathology in a transgenic AD mouse model.

Keywords: Magnetic resonance imaging; cortical thickness; Alzheimer's disease; beta-amyloid; quantitative immunohistochemistry; transgenic mouse model

Introduction

Cortical thickness measures derived from anatomical magnetic resonance imaging (MRI) data are increasingly utilized in neuroimaging studies of Alzheimer's disease (AD). Lerch et al. (2005) reported regional differences in cortical thickness between AD and age-matched healthy control (HC) subjects using a fully-automated approach. Other groups have, subsequently, utilized automated cortical thickness measures to distinguish mild cognitive impairment (MCI) from HC and AD subjects (Singh et al., 2006; Bakkour et al., 2009; Desikan et al., 2009; Querbes et al., 2009; Li et al., 2012), discriminate AD from frontotemporal dementia (Du et al., 2007), and differentiate cognitive phenotypes (Dickerson and Wolk, 2011). Cortical thickness has also been used to identify aberrant structural brain networks in AD (He et al., 2008). While measurement of cortical thickness allows for objective, quantitative assessment of altered brain structure, the relationship between thickness and β-amyloid deposition, a pathological hallmark of AD, remains obscure.

Becker et al. (2011) recently explored regional cortical thickness alterations in clinically normal, β-amyloid-positive subjects identified by positron emission tomography (PET) imaging using Pittsburgh Compound B (PiB). This cross-sectional study found local cortical thickness reductions, particularly in parietal and posterior cingulate regions, in subjects with high PiB retention, indicating the occurrence of abnormalities in cortical structure at an earlier stage than previously thought. PiB PET, however, is not sensitive to soluble, prefibrillar, or polymorphic forms of β-amyloid (Lockhart et al., 2007; Rosen et al., 2010; Leinonen et al., 2008). As such, the earliest structural manifestations of β-amyloid-associated pathology remain elusive. Large-scale, longitudinal MRI and PET studies beginning at the pre-deposition stage and extending over long intervals (*e.g.* decades) will be necessary to assess these potential

early alterations. While these long-term clinical studies are underway (*e.g.* Baltimore Longitudinal Study of Aging) or planned, animal models of AD, with well-characterized progression of β-amyloid pathology, currently offer the opportunity to interrogate the potential relationship between β-amyloid and structural MRI measures, such as cortical thickness.

Transgenic (Tg) murine models with targeted expression of mutant human amyloid precursor protein (APP) genes recapitulate many of the cognitive and neuropathological features of AD, and high-resolution images from the brains of these mice can be obtained with dedicated, high-field, small animal MRI systems. Several recent studies have identified differences in whole or regional brain structure between APP Tg and wild-type (WT) mice (Delatour et al., 2006; Lau et al., 2008; Oberg et al., 2008; Maheswaran et al., 2009; Badea et al., 2010; Hébert et al., 2013). Determination of the association between early pathological changes in brain structure and β-amyloid requires establishment of a strict spatial correspondence between structural and molecular measures. Ideally, this multi-parametric assessment could be achieved via co-registration of non-invasive mouse brain MRI and amyloid PET images. While amyloid PET in mice has been reported (Maeda et al., 2007; Manook et al., 2012), the relatively poor spatial resolution of animal PET scanners precludes accurate regional measures of β-amyloid burden in the mouse cerebral cortex. An alternate approach is to relate gold-standard, post-mortem, quantitative immunohistochemistry (IHC) data to the *in vivo* MRI measures.

Quantitative IHC (qIHC) has been used to validate *in vivo* molecular imaging studies, including amyloid PET tracers (Clark et al., 2011; Clark et al., 2012). Although IHC only allows for visualization and quantification of deposited, fibrillar amyloid, and does not directly provide quantitative measures of soluble forms, Bero et al. (2011)

recently demonstrated that the degree of regional amyloid plaque in aged mice corresponds to regional interstitial fluid (ISF) β-amyloid levels in young mice. Rigorous correlation between *in vivo* and post-mortem measures, such as qIHC, can be achieved through three-dimensional (3D) reconstruction of tissue sections. Lebenberg et al. (2011) demonstrated that 3D-reconstructed mouse brain autoradiographic volumes could be constructed, mapped to an MRI-based neuroanatomical atlas, and used to analyze metabolic changes in AD mice. Chakravarty et al. (2008) have described methods for 3D reconstruction of histological mouse brain sections and mapping the resulting histological volume to an MRI template.

In this study, we sought to interrogate the relationship between early alterations in cortical thickness and late-stage β-amyloid deposition in a well-established mouse model of AD. We acquired non-invasive, whole brain, 3D anatomical MRI data and employed fully-automated image processing/analysis to generate cortical thickness measures. We produced 3D qIHC volumes of β-amyloid deposition and correlated this post-mortem data with the *in vivo* MRI measures. We have determined that an aberrant temporal pattern of cortical thickness change at a young age predicts regional β-amyloid burden in later life. This data suggests a role for soluble β-amyloid in early pathological changes, and supports the need to assess brain morphology prior to deposition of fibrillar amyloid in clinical studies in order to identify the initial signatures of AD.

Materials and Methods

Animals

Heterozygous transgenic mice with neuronal overexpression of the Swedish ($670/671_{KM\rightarrow NL}$) and Indiana ($717_{V\rightarrow F}$) mutations of human APP driven by the platelet-derived growth factor β (PDGF-β) promoter on a C57BL/6J background (line J20) (Mucke et al., 2000; Tong et al., 2005) were used for these studies. This model has been well-characterized for amyloidosis (Mucke et al., 2000), cognitive/behavioral impairments (Palop et al., 2003), and cerebrovascular dysfunction (Tong et al., 2005).

Tg (n = 10 [5 male, 5 female]) and age-matched wild-type (WT) (n = 13 [7 male, 6 female]) mice underwent longitudinal MRI scans at 1.2 ± 0.2 months-of-age and 3.5 ± 0.1 months-of-age. All mice were scanned at both ages. A separate cohort of aged mice (n = 13 [6 male, 7 female]; 18.5 ± 0.1 months-of-age) were used for the post-mortem IHC studies. Mice were housed under a 12-hour light:12-hour dark schedule and fed standard laboratory chow and water *ad libitum*. Experiments were approved by the Animal Ethics Committee of the Montreal Neurological Institute and McGill University, and were conducted in accordance with the guidelines of the Canadian Council on Animal Care.

In Vivo MRI Acquisition

Mice were anesthetized with an induction dose of 4-5% sevoflurane and secured in an MRI-compatible bed. All MRI studies were performed under 2.5-3% sevoflurane in medical air and animals were allowed to breathe spontaneously without mechanical ventilation. Respiration rate and body temperature was continuously monitored using an MR-compatible system (Small Animal Instruments Inc., Stony Brook, NY) and the temperature was

maintained at 37 ± 0.2°C throughout the study using a feedback-regulated warming system (Small Animal Instruments Inc., Stony Brook, NY).

All MR images were obtained from a 7T Bruker Pharmascan system (Bruker Biospin, Ettlingen, Germany) using a 28-mm inner-diameter, quadrature volume resonator (RAPID MR International, Columbus, OH). Anatomical images were acquired using a 3D balanced Steady-State Free Precession (b-SSFP) sequence with repetition time (TR) = 5.2, echo time (TE) = 2.6, flip angle = 30°, matrix size = 128×128×64, field-of-view = 1.8×1.8×0.9 cm, spatial resolution = 140x140×140 μm, number of phase-cycles = 4, number of averages = 4, and acquisition time = 35 minutes. The phase-cycled images were combined using the sum-of-squares reconstruction method in order to minimize banding artifacts (Bangerter et al., 2004).

MRI Processing

An unbiased, symmetric, customized template was generated from the 1 and 3.5 month-of-age anatomical scans from the 23 mice using an iterative process (Lau et al., 2008; Fonov et al., 2011). Prior to template generation, each reconstructed image volume underwent image non-uniformity correction using the N3 algorithm (Sled et al., 1998), brain masking, and linear spatial normalization utilizing a 12-parameter affine transformation (Collins et al., 1994) to map individual images from native coordinate space to reference space. Briefly, the template generation process involved an iterative (coarse-to-fine resolution) estimation of the nonlinear transformation to match each MRI scan to the evolving average of the population. The final anatomical template (population average) was generated with an isotropic voxel resolution of 0.06 mm. This customized template was parcellated into an atlas, including the following neocortical regions: anterior cingulate cortex, auditory cortex, barrel cortex, entorhinal cortex, frontal cortex, insula, motor cortex, perirhinal cortex,

posterior cingulate cortex, retrosplenial cortex, somatosensory cortex 1, somatosensory cortex 2, and visual cortex, using the Montreal Neurological Institute (MNI) DISPLAY software package (http://www.bic.mni.mcgill.ca). The labels for these cerebral cortical regions were projected onto a standardized cortical surface template for surface-based region-of-interest (ROI) analysis (Fig. 1B).

For cortical thickness measurements, the cortical mask with inside, outside, interhemispheric, and resistive boundaries was nonlinearly aligned with each subject using the template-to-subject transformation. Streamlines running from the inner to outer boundaries of the cortex were defined using Laplace's equation and their length was used as the measure of cortical thickness (Lerch et al., 2008). The mean cortical thickness was computed from an intermediate surface for each of the pre-defined ROIs from the spatially normalized thickness maps. Whole cortical volume was also computed from the transformed cortical mask for each subject.

Immunohistochemistry

The cohort of aged mice were deeply anesthetized with urethane (1 g/kg) and exsanguinated via transcardiac perfusion with phosphate-buffered saline (PBS), followed by transcardiac infusion of 50 mL of 10% neutral-buffered formalin. Following perfusion, the brains were extracted and immersion-fixed in 10% neutral-buffered formalin for 72 hours. The brains were dehydrated through graded ethanol and xylene, and infiltrated with paraffin wax. The whole brains were oriented and embedded in paraffin blocks. Each block was sectioned from olfactory bulb through brainstem (5 µm thickness/section, 120 sections/brain, inter-section distance = 100 µm) onto positively-charged glass slides.

For IHC, the slides were manually de-paraffinized and re-hydrated, incubated in an 80% formic acid epitope-retrieval solution for 5 minutes, and washed twice in deionized

H_2O. All IHC studies were performed at room temperature on a Lab Vision 360 Autostainer (Fisher Scientific, Toronto, ON, Canada). The slides were stained using the REVEAL Polyvalent HRP-AEC detection system (Spring Bioscience, Pleasanton, CA). Briefly, slides were sequentially incubated with hydrogen peroxide for 10 minutes to quench endogenous peroxidase, followed by 10 minutes in Protein Block, then 90 minutes in the 4G8 primary antibody (1:5000 dilution; Covance, Princeton, NJ). The primary antibody binding was amplified using Complement (20 minutes), HRP-Conjugate (30 minutes), and visualized using AEC Single Solution (10 minutes). All sections were counterstained with Acid Blue 129 (Sigma-Aldrich, St. Louis, MO) and mounted with aqueous mounting medium (Zehntner et al., 2008).

qIHC 3D Reconstruction

The IHC sections were digitized using a MIRAX Scan 150 whole slide scanner (Carl Zeiss, Toronto, ON, Canada). The MIRAX images were, subsequently, converted to the Medical Image NetCDF (MINC) file format. 3D reconstruction of the IHC sections was performed using PERMITS™ software (Biospective Inc., Montreal, QC, Canada). PERMITS™ employs a multi-step image registration process to generate a 3D qIHC volume. This process includes: (1) between-section alignment in a coarse-to-fine fashion, proceeding from an initial center-of-mass alignment, through affine alignment, and then several passes of nonlinear between-section alignment, and (2) registration of the resulting 3D volume to the *in vivo* MRI template using a coarse-to-fine multi-resolution nonlinear registration process (Chakravarty et al., 2008). Mapping to the MRI template serves to recapitulate the structure of the mouse brain, as well as transform the qIHC data to MRI reference coordinate space.

Two-dimensional (2D) qIHC maps were generated for each section using an artificial neural network (ANN) classifier (Zijdenbos et al., 2002). The classifier was trained to discriminate between AEC chromogen, Acid Blue 129 counterstain, and background. The same classifier was applied to all sections, in a fully-automated manner, to generate unbiased, binarized (chromogen vs. non-chromogen) images (2D qIHC maps). The concatenated transformations derived from the 3D reconstruction process were then applied to the 2D qIHC maps to generate 3D qIHC volumes of β-amyloid burden. In order to directly compare β-amyloid burden with the surface-based cortical thickness measures, the qIHC data was projected to the cortical surface by averaging the image intensity along each streamline (derived from the cortical thickness analysis) passing through each vertex. The individual, spatially normalized, qIHC volumes were averaged to produce group-mean parametric volumes. The ROI-based qIHC measures were derived utilizing the surface MRI atlas in reference space.

Statistical Analysis

Statistical analysis was performed using Matlab (Mathworks, Natick, MA, USA) and the SurfStat toolbox (http://www.math.mcgill.ca/keith/surfstat) (Worsley et al., 2009). ROI-based measures from the left and right hemispheres were combined, and quantitative results are expressed as mean ± standard deviation of the effect of interest. Linear mixed-effects models using the restricted maximum likelihood (REML) estimation method were employed to assess group differences and cross-sectional changes (Pinheiro and Bates, 2000). Specifically, a one-way analysis of variance (ANOVA) was employed to assess between-groups differences (Tg vs. WT) at each age level (1.5 and 3 months-of-age). A two-way ANOVA with repeated measures was utilized to assess the genotype-by-age interaction. Post-hoc Student's two-tailed t-tests

were used for group comparisons. The data was adjusted for multiple comparisons using the Bonferroni correction and $p < 0.05$ was considered significant.

Results

Longitudinal cortical thickness measures from young mice

The thickness varied across the regions of the mouse cerebral cortex with thicker frontal regions and thinner posterior/inferior regions (Fig. 1A). A globally decreased mean cortical thickness was identified in the 1 month-old Tg mice compared to Young WT mice (Fig. 2), while an increased mean cortical thickness was found at 3.5 months-of-age (Fig. 3). The ROI-based analysis (Fig. 2) demonstrated that the cerebral cortex was significantly thinner in the 1 month-old Tg group relative to the WT group, with the exception of the anterior cingulate, entorhinal/perirhinal, frontal, insula, posterior cingulate, and retrosplenial cortical regions. While the anterior cingulate and insula demonstrated significant group differences without Bonferroni correction (anterior cingulate: $p_{uncorrected} = 0.029$; insula: $p_{uncorrected} = 0.032$), this significance did not survive multiple comparisons. In contrast, the Tg mice had thicker cortex than WT at 3.5 months-of-age (Fig. 3). At this age, several regions demonstrated significant group differences prior to Bonferroni correction (posterior cingulate cortex: $p_{uncorrected} = 0.018$; retrosplenial cortex: $p_{uncorrected} = 0.009$; somatosensory cortex 2: $p_{uncorrected} = 0.034$; visual cortex: $p_{uncorrected} = 0.049$; whole cortex: $p_{uncorrected} = 0.011$), but the significance did not survive multiple comparisons. We did not observe significant outliers in any of the groups (Fig. 4C).

The longitudinal studies revealed stable or increasing cortical thickness in the Tg mice, while the WT mice showed decreasing thickness over the 2.5 month observation period at the whole cortical and regional levels (Fig. 4 and 5). The changes in the whole cortical volume showed similar behavior to the thickness measures (Fig. 4). Most regions demonstrated significant differences in the age-by-genotype interaction, with

the exception of the anterior cingulate ($p_{uncorrected}$ = 0.014) and posterior cingulate ($p_{uncorrected}$ = 0.139).

β-amyloid 3D qIHC volumes and regional measures from aged mice

Representative, digitized 4G8 IHC-stained tissue sections from an individual mouse brain are shown in Fig. 6. The high level of contrast between the red-brown AEC chromogen and the Acid Blue 129 counterstain, as well as the heterogeneous distribution of the β-amyloid deposits across cortical regions, can be readily appreciated on these sections. Orthogonal views of the group-average 3D qIHC volume from all 13 aged Tg mice are shown in Fig. 7. High levels of deposited β-amyloid are readily apparent in the entorhinal cortex, posterior cingulate/retrosplenial cortex, and hippocampus. The surface-projected qIHC data is provided in Fig. 8. The regional heterogeneity of β-amyloid deposition, as well as an anterior-to-posterior gradient, can clearly be seen in this figure. The β-amyloid burden (expressed as % volume occupied) for each of the cortical ROIs is provided in Fig. 9.

Relationship between early cortical thickness changes and late β-amyloid deposition

The regional difference between change in thickness over 2.5 months in young Tg relative to WT mice (*i.e.* difference between slopes) showed a strong negative association with regional β-amyloid burden in aged mice (r = 0.75, p = 0.003) (Fig. 10). A caveat associated with this analysis is that the observations are spatially correlated with respect to the β-amyloid burden. As such, the significance could potentially be inflated. Nevertheless, a clear relationship is evident between the thickness and β-amyloid measures. The anterior/posterior cingulate and retrosplenial cortex

demonstrated little change over time in both genotypes. These regions also did not show any significant differences in cortical thickness between genotypes at 1 month-of-age (Fig. 2). The β-amyloid burden was found to be highest in these regions. The entorhinal cortex and frontal cortical regions demonstrated similar behavior. Conversely, many of the sensory regions showed a substantial groupwise difference in cortical thickness change over the 2.5 months. In these regions, the thickness increased in the Tg mice, while decreasing in the WT animals. These regions had relatively low β-amyloid burdens in aged mice (Fig. 9). Interestingly, the general pattern of β-amyloid burden (Fig. 8) also appeared to be inversely related to that of the baseline cortical thickness (Fig. 1A).

Discussion

In this work, we have explored the relationship between early (pre-plaque) structural MRI alterations and late-stage β-amyloid load in a mouse model of AD. We have employed a novel, automated, production-level method to co-register *in vivo* MRI and post-mortem qIHC volumes, which allowed us to utilize a common coordinate space and neuroanatomical atlas to perform a strict correlation between cortical thickness and β-amyloid burden. Using this approach, we identified a strong relationship between early-stage changes in regional cortical thickness and later β-amyloid deposition.

The cortical thickness in the posterior cingulate/retrosplenial, entorhinal/perirhinal, and frontal regions in one month-old Tg mice was similar to or had a tendency to be thicker than that of the age-matched WT mice, and these regions did not show substantial differences in temporal evolution between the genotypes. The β-amyloid plaque burden was highest in these same regions in the aged mice. These regions correspond to nodes of the default-mode network (DMN) in the human brain. The DMN has been associated with elevated β-amyloid levels, possibly resulting from high constitutive activity, and cortical thinning has been observed in DMN regions in amyloid-positive, clinically-normal human subjects (Buckner et al., 2009; Becker et al., 2011).

In contrast to the DMN-associated regions, the sensory regions in our study were associated with lower levels of β-amyloid deposits. In these areas, the cortex was thinner in Tg compared to WT mice at 1 month-of-age, but increased over the ensuing 2.5 months in the Tg group, while decreasing in the WT group. The underlying cellular processes driving these macroscopic structural changes are currently unknown and further investigation is certainly warranted. Possible mechanisms for the increased cortical thickness in the 3 month-old Tg mice could include neuronal hypertrophy

(Riudavets et al., 2007; Iacono et al., 2008; Iacono et al., 2009) and/or astrogliosis (Beach et al., 1989). Using human autopsy material from the Baltimore Longitudinal Study of Aging, Riudavets et al. (2007) and Iacono et al. (2008) observed neuronal hypertrophy in the cerebral cortex and hippocampus in asymptomatic AD subjects compared with normal control and cognitively-impaired subjects. This observation was replicated in the Nun Study (Iacono et al., 2009). These investigators postulated that neuronal hypertrophy may constitute an early cellular response to AD pathology and/or reflect compensatory mechanisms that prevent cognitive impairment despite substantial AD-associated pathological changes. The distinct temporal changes in cortical architecture between Tg and WT mice could also be potentially explained by differences in neuronal and/or non-neuronal (*e.g.* glial) remodeling during early life.

The negative correlation between regional thickness change and β-amyloid was an unexpected finding. While the basis of this observation currently remains unexplained, our group is actively investigating the cellular processes underpinning this intriguing relationship. One potential mechanism that could account for this negative correlation, as well as the apparent differences between DMN-associated and sensory regions, is the existence of distinct temporal profiles. It is possible that the DMN-associated regions demonstrate similar morphological changes to the sensory regions (*i.e.* early hypertrophy), but these alterations have already occurred prior to one month-of-age. These structural changes may have taken place after birth or during early development given that the PDGF-β promoter, which drives the APP expression in the mouse model employed in this study, is active in neurons of the mouse brain during the mid-to-late stages of embryogenesis (Hutchins and Jefferson, 1992). As such, our "early" timepoint may not have been sufficiently early to capture this process and this potential caveat should be taken into account in the interpretation of our data. Unfortunately, it is

difficult to perform cortical thickness measurements on mice younger than one month-of-age due to the suboptimal gray matter-white matter contrast on anatomical MRI scans.

It is plausible that high levels of soluble β-amyloid may be responsible for the early structural changes. Bero et al. (2011) established a correspondence between regional ISF levels of soluble amyloid and later plaque density. Based on such a relationship, our data would then suggest that the highest levels of soluble amyloid are present in the DMN-associated regions, thereby driving spatio-temporal pattern of structural alterations which we observed.

Bero et al. (2012) performed an elegant study to correlate regional bilateral functional correlation, determined by functional connectivity optical intrinsic signal (fcOIS) imaging, with β-amyloid burden from IHC studies. This group determined that both bilateral functional correlation and age-related decline in functional correlation in young APP/PS1 mice was indicative of subsequent regional β-amyloid deposition. Interestingly, the region that showed the greatest abnormality in functional correlation was the retrosplenial cortex. Badea et al. (2010) identified local/regional alterations in brain volumes of young Tg APP mice by deformation-based morphometry (DBM), and established a qualitative correspondence with later appearance of amyloid plaques. Taken together, the studies by Bero et al. (2012), Badea et al. (2010), and our group suggest that early region-specific structural and functional disruptions are tightly linked with β-amyloid.

We found that the changes in cortical thickness which correlated with amyloid load were more readily apparent at the regional rather than local (*i.e.* vertex) level. A plausible explanation for this observation is that the exact locations of β-amyloid deposition and the downstream effects related to the soluble and fibrillar forms β-

amyloid (*e.g.* structural alterations) may be spatially distinct. Meyer-Luehmann et al. (2003) suggested that soluble β-amyloid aggregates may diffuse over considerable distances in the extracellular space and affect neuronal processes away from the site of production. Badea et al. (2010) demonstrated that structural MRI changes and eventual β-amyloid deposition can even occur in brain regions which are remote from the sites of APP overexpression, presumably through transsynaptic spread via afferent connections, which is supported by recent work by Harris et al. (2010).

The findings from our study indicate that amyloid-associated effects on cerebral cortical morphometry occur in advance of fibrillar peptide deposition. The remarkably similar functional derangements observed by Bero and colleagues (2012) using fcOIS warrant future studies to further explore the relationship between structural and functional measures in AD mouse models, which can readily be performed using MRI. Given the translational nature of MRI, long-term, longitudinal, natural history imaging studies, initiated well before the appearance of plaques and cognitive changes, may reveal similar observations in human subjects. In fact, Dickerson and Wolk (2012) have recently identified an early "cortical signature" of impending AD pathology based on cortical thickness measures derived from MRI data from the Alzheimer's Disease Neuroimaging Initiative (ADNI). As such, MRI-based assessment of cortical thickness may represent a powerful imaging biomarker and facilitate the potential for disease modification at the earliest stages.

Acknowledgements

This work was supported by the Canadian Institutes of Health Research (Operating Grant MOP-93795 to B.J.B.). We thank Dr. Lennart Mucke and the Gladstone Institutes for use of the J20 APP mice. We also thank Antonio Aliaga and Kung-Yuan Lin for acquisition of the MRI data, and Rozica Bolovan and Qin Shao for preparation of the IHC sections.

References

Badea A, Johnson GA, Jankowsky JL. Remote sites of structural atrophy predict later amyloid formation in a mouse model of Alzheimer's disease. Neuroimage 2010;50:416-27.

Bakkour A, Morris JC, Dickerson BC. The cortical signature of prodromal AD: regional thinning predicts mild AD dementia. Neurology 2009;72:1048-55.

Bangerter NK, Hargreaves BA, Vasanawala SS, Pauly JM, Gold GE, Nishimura DG. Analysis of multiple-acquisition SSFP. Magn Reson Med 2004;51:1038-47.

Beach TG, Walker R, McGeer EG. Patterns of gliosis in Alzheimer's disease and aging cerebrum. Glia 1989;2:420-36.

Becker, JA, Hedden T, Carmasin J, Maye J, Rentz DM, Putcha D, et al. Amyloid-β associated cortical thinning in clinically normal elderly. Ann Neurol 2011;69:1032-42.

Bero AW, Yan P, Roh JH, Cirrito JR, Stewart FR, Raichle ME, et al. Neuronal activity regulates the regional vulnerability to amyloid-B deposition. Nat Neurosci 2011;14:750-6.

Bero AW, Bauer AQ, Stewart FR, White BR, Cirrito JR, Raichle ME, et al. Bidirectional relationship between functional connectivity and amyloid-β deposition in the mouse brain. J Neurosci 2012;32:4334-40.

Buckner RL, Sepulcre J, Talukdar T, Krienen FM, Liu H, Hedden T, et al. Cortical hubs revealed by intrinsic functional connectivity: mapping, assessment of stability, and relation to Alzheimer's disease. J Neurosci 2009;29:1860-73.

Chakravarty MM, Bedell BJ, Zehntner SP, Evans AC, Collins DL. Three-dimensional reconstruction of serial histological mouse brain sections. 5th IEEE International Symposium on Biomedical Imaging, Paris, France, May 14-17, 2008.

Clark CM, Schneider JA, Bedell BJ, Beach TG, Bilker WB, Mintun MA, et al. Use of florbetapir-PET for imaging beta-amyloid pathology. JAMA 2011;305:275-83.

Clark CM, Pontecorvo MJ, Beach TG, Bedell BJ, Coleman RE, Doraiswamy PM, et al. Cerebral PET with florbetapir compared with neuropathology at autopsy for detection of neuritic amyloid-β plaques: a prospective cohort study. Lancet Neurol 2012;11:669-78.

Collins DL, Neelin P, Peters TM, Evans AC. Automatic 3D inter-subject registration of MR volumetric data in standardized Talairach Space. J Comput Assist Tomogr 1994;18:192-205.

Delatour B, Guegan M, Volk A, Dhenain M. In vivo and histological evaluation of brain atrophy in APP/PS1 transgenic mice. Neurobiol Aging 2006;27:835-47.

Desikan RS, Cabral HJ, Hess CP, Dillon WP, Glastonbury CM, Weiner MW, et al. Automated MRI measures identify individuals with mild cognitive impairment and Alzheimer's disease. Brain 2009;132:2048–57.

Dickerson BC, Wolk DA. Dysexecutive versus amnestic phenotypes of very mild Alzheimer's disease are associated with distinct clinical, genetic and cortical thinning characteristics. J Neurol Neurosurg Psychiatry 2011;82:45-51.

Dickerson BC, Wolk, DA. MRI cortical thickness biomarker predicts AD-like CSF and cognitive decline in normal adults. Neurology 2012;78:84-90.

Du A-T, Schuff N, Kramer JH, Rosen HJ, Gorno-Tempini ML, Rankin K, et al. Different regional patterns of cortical thinning in Alzheimer's disease and frontotemporal dementia. Brain 2007;130:1159–66.

Fonov V, Evans AC, Botteron K, Almli CR, McKinstry RC, Collins DL. Unbiased average age-appropriate atlases for pediatric studies. Neuroimage 2011;54:313-27.

Harris JA, Devidze N, Verret L, Ho K, Labisky B, Thwin MT, et al. Transsynaptic progression of amyloid-β-induced neuronal dysfunction within the entorhinal-hippocampal network. Neuron 2010;68:428-41.

Hébert F, Grand'Maison M, Ho M-K, Lerch JP, Hamel E, Bedell BJ. Cortical atrophy and hypoperfusion in a transgenic mouse model of Alzheimer's disease. Neurobiol Aging 2013 [Epub ahead of print] doi: 10.1016/j.neurobiolaging.2012.11.022.

He Y, Chen Z, Evans A. Structural insights into aberrant topological patterns of large-scale cortical networks in Alzheimer's disease. J Neurosci 2008;28:4756-66.

Hutchins JB, Jefferson VE. Developmental distribution of platelet-derived growth factor in the mouse central nervous system. Dev Brain Res 1992;67:121-35.

Iacono D, O'Brien R, Resnick SM, Zonderman AB, Plentikova O, Rudow G, et al. Neuronal hypertrophy in asymptomatic Alzheimer disease. J Neuropathol Exp Neurol 2008;67:578-89.

Iacono D, Markesbery WR, Gross M, Pletnikova O, Rudow G, Zandi P, et al. The Nun Study: clinically silent AD, neuronal hypertrophy, and linguistic skills in early life. Neurology 2009;73:665-73.

Lau JC, Lerch JP, Sled JG, Henkelman RM, Evans AC, Bedell BJ. Longitudinal neuroanatomical changes determined by deformation-based morphometry in a mouse model of Alzheimer's disease. Neuroimage 2008;42:19-27.

Lebenberg J, Hérard AS, Dubois A, Dhenain M, Hantraye P, Delzescaux T. A combination of atlas-based and voxel-wise approaches to analyze metabolic changes in autoradiographic data from Alzheimer's mice. Neuroimage 2011;57:1447-57.

Leinonen V, Alafuzoff I, Aalto S, Suotunen T, Savolainen S, Någren K, et al. Assessment of beta-amyloid in a frontal cortical brain biopsy specimen and by positron emission tomography with carbon 11-labeled Pittsburgh Compound B. Arch Neurol 2008;10:1304-09.

Lerch JP, Pruessner JC, Zijdenbos A, Hampel H, Teipel SJ, Evans AC. Focal decline of cortical thickness in Alzheimer's disease identified by computational neuroanatomy. Cereb Cortex 2005;15:995-1001.

Lerch JP, Carroll JB, Dorr A, Spring S, Evans AC, Hayden MR, et al. Cortical thickness measured from MRI in the YAC128 mouse model of Huntington's disease. Neuroimage 2008;41:243-51.

Li Y, Wang Y, Wu G, Shi F, Zhou L, Lin W, et al. Discriminant analysis of longitudinal cortical thickness changes in Alzheimer's disease using dynamic and network features. Neurobiol. Aging 2012;33:427.e15-427.e30.

Lockhart A, Lamb JR, Osredkar T, Sue LI, Joyce JN, Ye L, et al. PIB is a non-specific imaging marker of amyloid-beta (Abeta) peptide-related cerebral amyloidosis. Brain 2007;130:2607-15.

Maeda J, Ji B, Irie T, Tomiyama T, Maruyama M, Okauchi T, et al. Longitudinal, quantitative assessment of amyloid, neuroinflammation, and anti-amyloid treatment

in a living mouse model of Alzheimer's disease enabled by positron emission tomography. J Neurosci 2007;27:10957-68.

Maheswaran S, Barjat H, Rueckert D, Bate ST, Howlett DR, Tilling L, et al. Longitudinal regional brain volume changes quantified in normal aging and Alzheimer's APP x PS1 mice using MRI. Brain Res 2009;1270:19-32.

Manook A, Yousefi BH, Willuweit A, Platzer S, Reder S, Voss A, et al. Small-animal PET imaging of amyloid-beta plaques with [11C]PiB and its multi-modal validation in an APP/PS1 mouse model of Alzheimer's disease. PLoS ONE 2012;7:e31310.

Meyer-Luehmann M, Stalder M, Herzig MC, Kaeser SA, Kohler E, Pfeifer M, et al. Extracellular amyloid formation and associated pathology in neural grafts. Nat. Neurosci. 2003;6:370-7.

Mucke L, Masliah E, Yu GQ, Mallory M, Rockenstein EM, Tatsuno G, et al. High-level neuronal expression of Aβ1–42 in wild-type human amyloid protein precursor Tg mice: synaptotoxicity without plaque formation. J Neurosci 2000;20:4050–8.

Oberg J, Spenger C, Wang F-H, Andersson A, Westman E, Skoglund P, et al. Age related changes in brain metabolites observed by ^{1}H MRS in APP/PS1 mice. Neurobiol Aging 2008;29:1423-33.

Palop JJ, Jones B, Kekonius L, Chin J, Yu GQ, Raber J, et al. Neuronal depletion of calcium-dependent proteins in the dentate gyrus is tightly linked to Alzheimer's disease-related cognitive deficits. Proc Natl Acad Sci USA 2003;100:9572-77.

Pinheiro JC, Bates DM. Mixed-effects models in S and S-PLUS. New York: Springer; 2000.

Querbes O, Aubry F, Pariente J, Lotterie J-A, Démonet J-F, Duret V, et al. Early diagnosis of Alzheimer's disease using cortical thickness: impact of cognitive reserve. Brain 2009;132:2036–47.

Riudavets MA, Iacono D, Resnick SM, O'Brien R, Zonderman AB, Martin LJ, et al. Resistance to Alzheimer's pathology is associated with nuclear hypertrophy in neurons. Neurobiol Aging 2007;28:1484-92.

Rosen RF, Ciliax BJ, Wingo TS, Gearing M, Dooyema J, Lah JJ, et al. Deficient high-affinity binding of Pittsburgh compound B in a case of Alzheimer's disease. Acta Neuropathol 2010;119:221-33.

Singh V, Chertkow H, Lerch J, Evans A, Dorr A, Kabani N. Spatial patterns of cortical thinning in mild cognitive impairment and Alzheimer's disease. Brain 2006;129:2885–93.

Sled JG, Zijdenbos AP, Evans AC. A nonparametric method for automatic correction of intensity nonuniformity in MRI data. IEEE Trans Med Imaging 1998;17:87-97.

Tong X-K, Nicolakakis N, Kocharyan A, Hamel E. Vascular remodeling versus amyloid β-induced oxidative stress in the cerebrovascular dysfunctions associated with Alzheimer's disease. J Neurosci 2005;25:11165-74.

Worsley KJ, Taylor JE, Carbonell F, Chung MK, Duerden E, Bernhardt B, et al. SurfStat: a Matlab toolbox for the statistical analysis of univariate and multivariate surface and volumetric data using linear mixed effects models and random field theory. Proceedings of the 15th Annual Meeting of the Organization for Human Brain Mapping, San Francisco, CA, USA, 2009.

Zehntner SP, Chakravarty MM, Bolovan RJ, Chan C, Bedell BJ. Synergistic tissue counterstaining and image segmentation techniques for accurate, quantitative immunohistochemistry. J Histochem Cytochem 2008;56:873-80.

Zijdenbos AP, Forghani R, Evans AC. Automatic "pipeline" analysis of 3-D MRI data for clinical trials: application to multiple sclerosis. IEEE Trans Med Imaging 2002;21:1280-91.

Figures

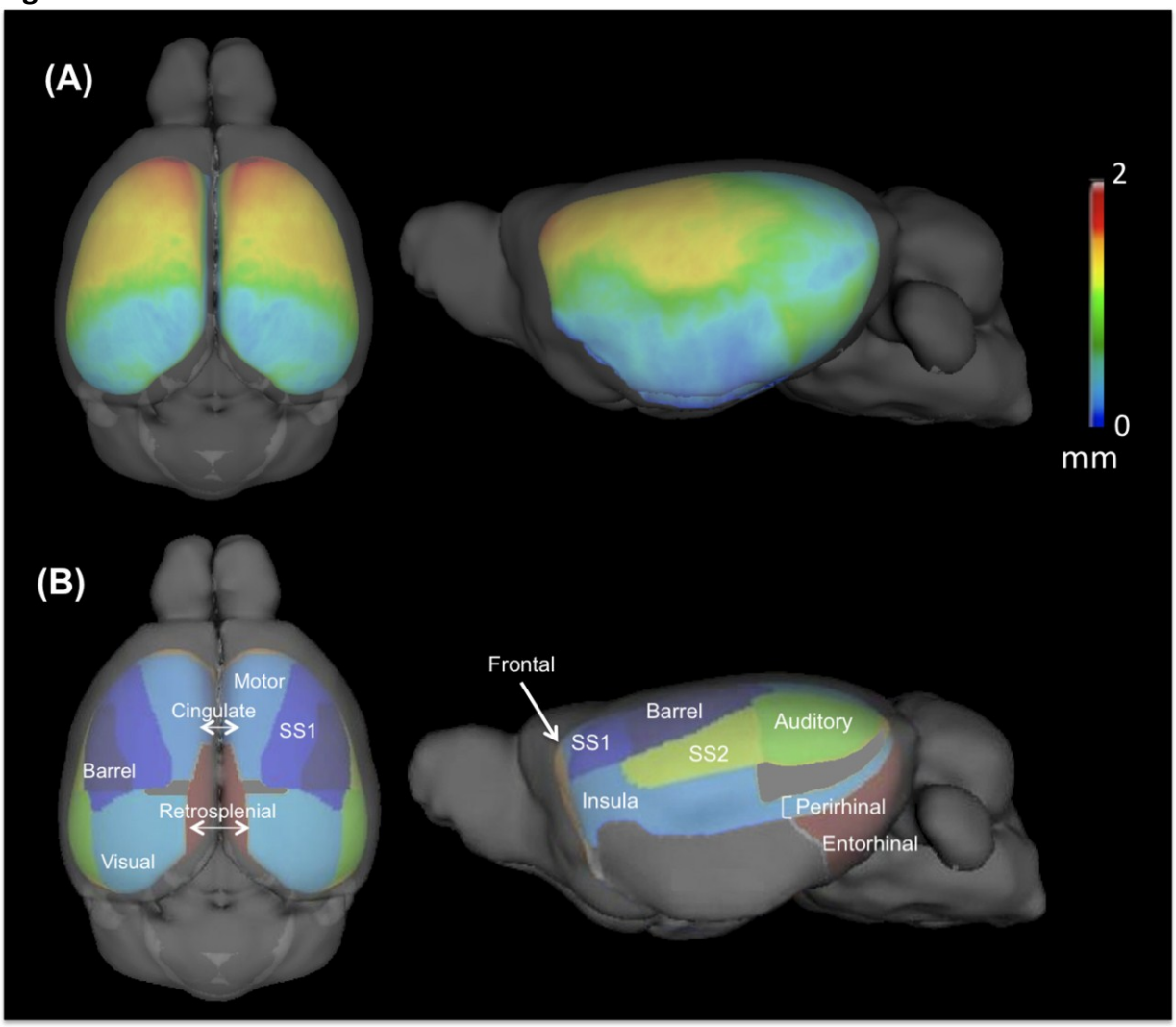

Figure 1 Superior and lateral views of the WT group average (n=13) thickness across the cerebral cortex (A), and the parcellated cortical surface atlas (B).

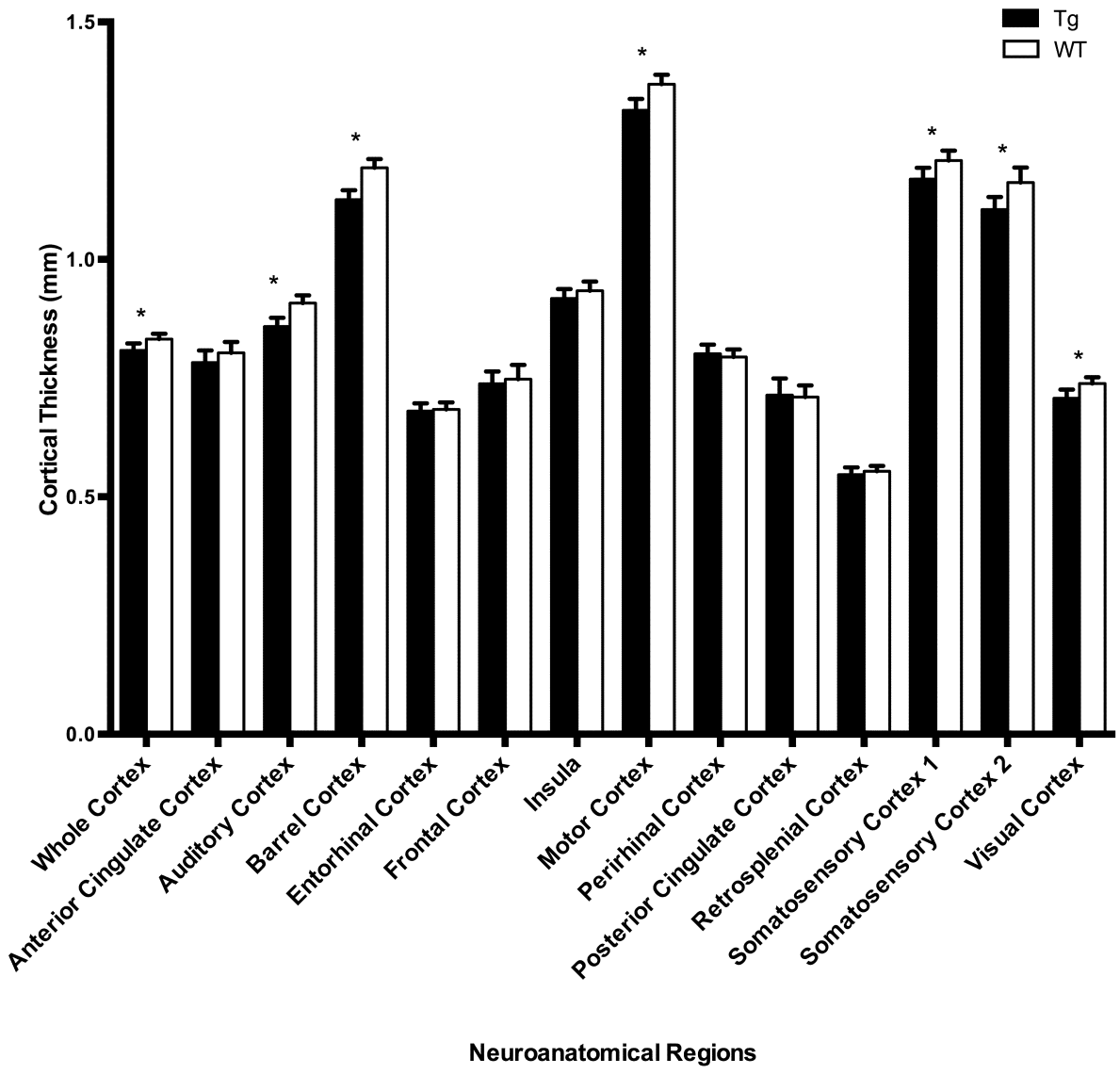

Figure 2 Regional MRI cortical thickness measures from 1 month-old Tg and WT mouse groups. Note that the whole cortex and the majority of regions demonstrated a thinner cortex in Tg mice compared to age-matched WT mice. * indicates $p < 0.05$.

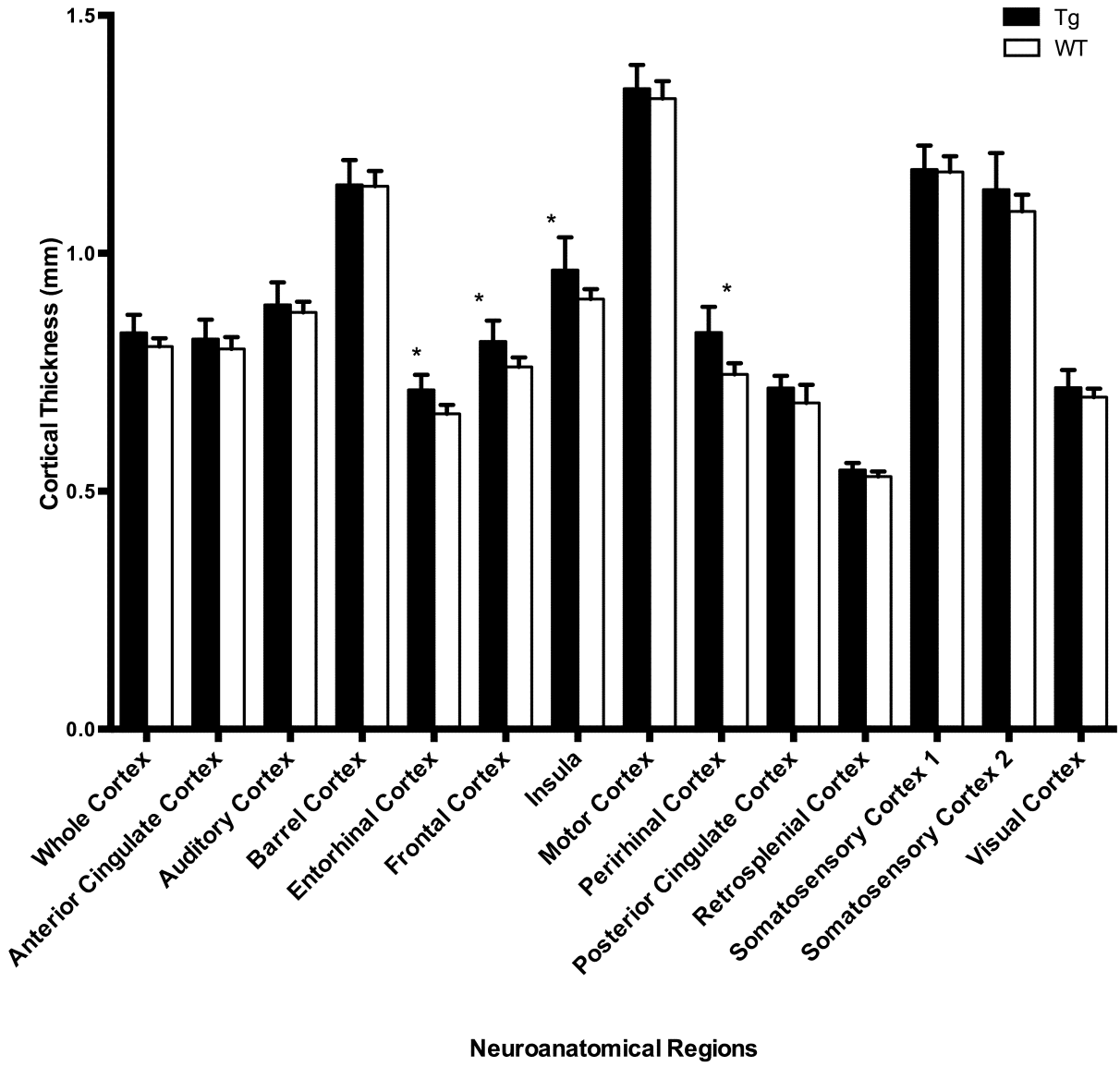

Figure 3 Regional MRI cortical thickness measures from 3.5 month-old Tg and WT mouse groups. Note that the whole cortex and the majority of regions demonstrated a thicker cortex in Tg mice compared to age-matched WT mice. * indicates $p < 0.05$.

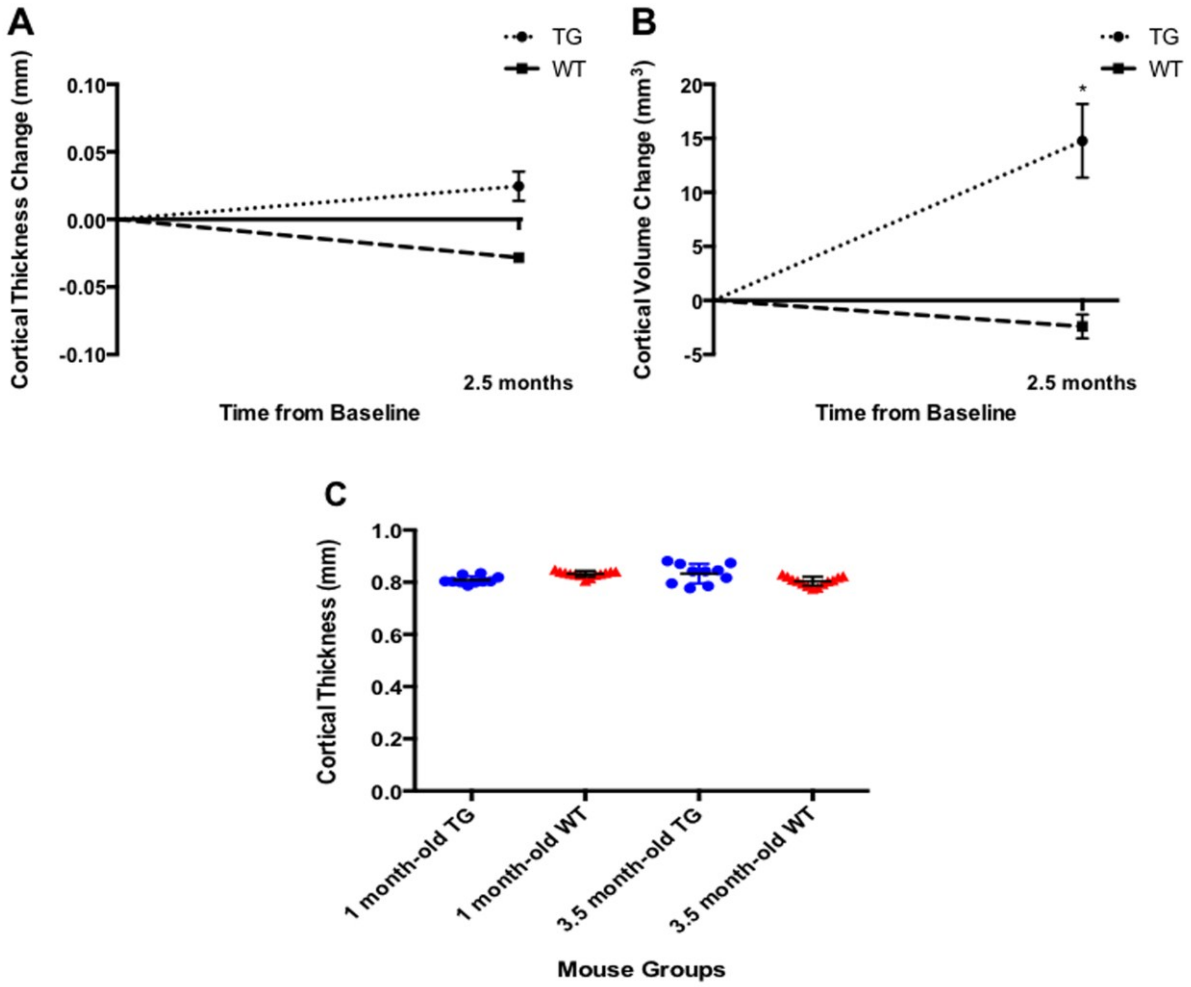

Figure 4 Whole cortex thickness (A) and volume (B) changes (relative to the 1 month-old mouse group) over 2.5 months in Tg and WT mice, and (C) whole cortex thickness data for the individual mice. The Tg mice showed increasing whole cortical thickness and volume in the Tg mice, while the WT mice showed decreasing thickness and volume. Note that there are not any significant outliers (C). * indicates $p < 0.05$.

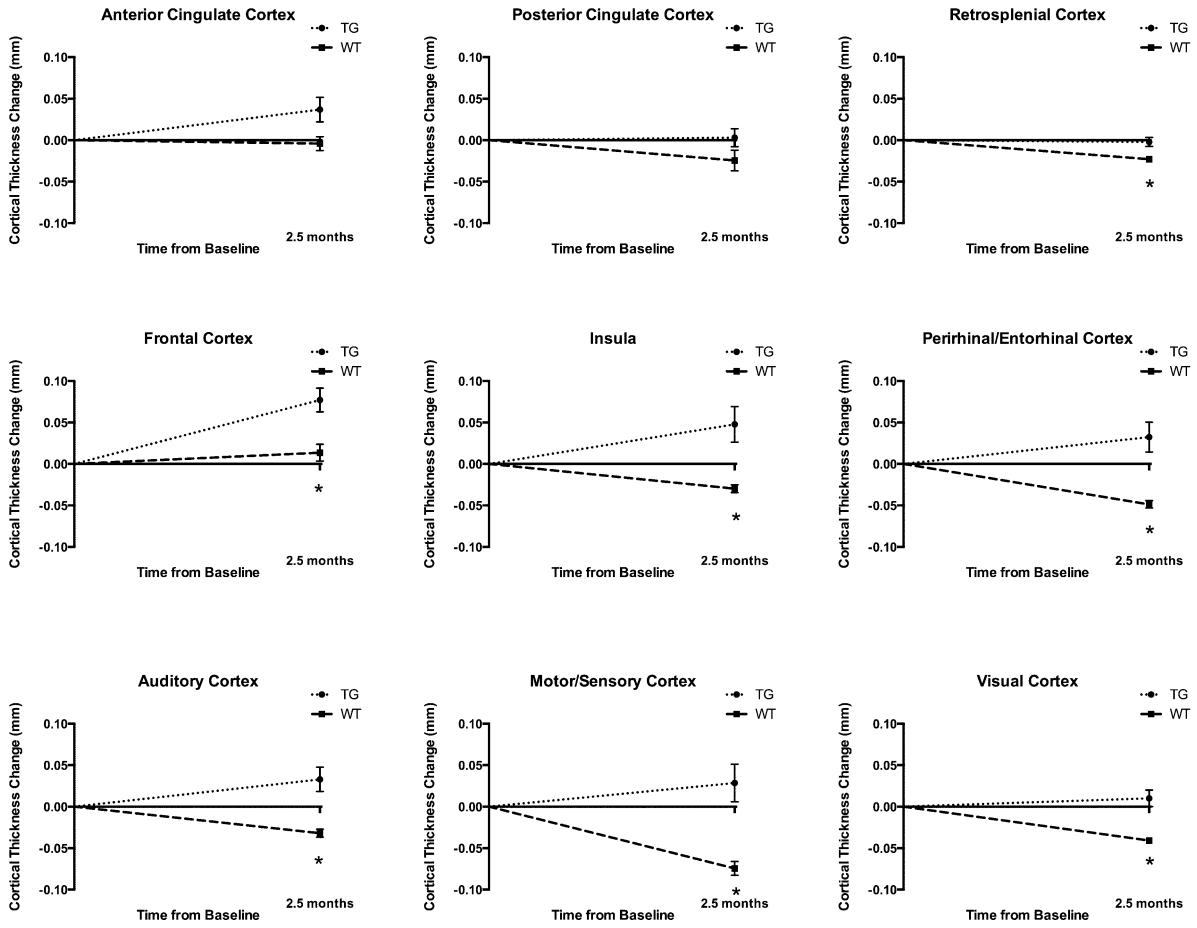

Figure 5 Regional cortical thickness change (relative to 1 month-old mouse group) over 2.5 months in Tg and WT mice. The Tg mice generally had stable or increasing regional cortical thickness in the Tg mice, while the WT mice showed decreasing thickness. * indicates $p < 0.05$.

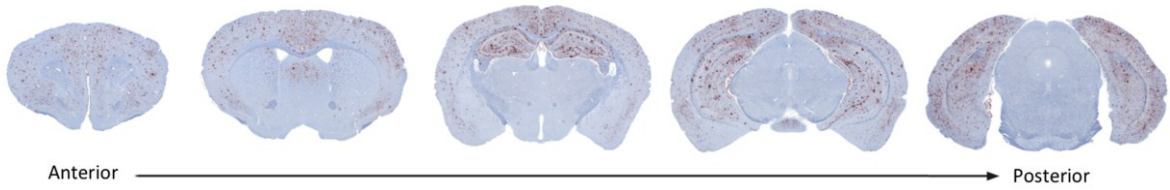

Figure 6 Representative coronal sections of the original 4G8 IHC spanning the cerebral cortex. Note the excellent contrast between the red-brown AEC chromogen and the Acid Blue 129 counterstain, as well as the regional heterogeneity of β-amyloid deposition.

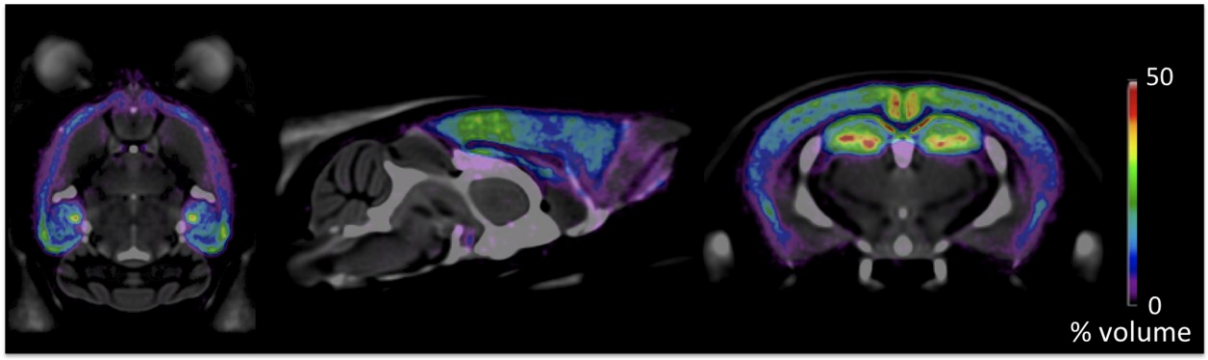

Figure 7 Representative orthogonal views (axial, sagittal, and coronal, left-to-right, respectively) of the group-average β-amyloid 3D qIHC volume from aged mice (n=13) superimposed on the anatomical MRI template. High levels of deposited β-amyloid are apparent in the posterior cingulate/retrosplenial cortex, entorhinal cortex, and hippocampus.

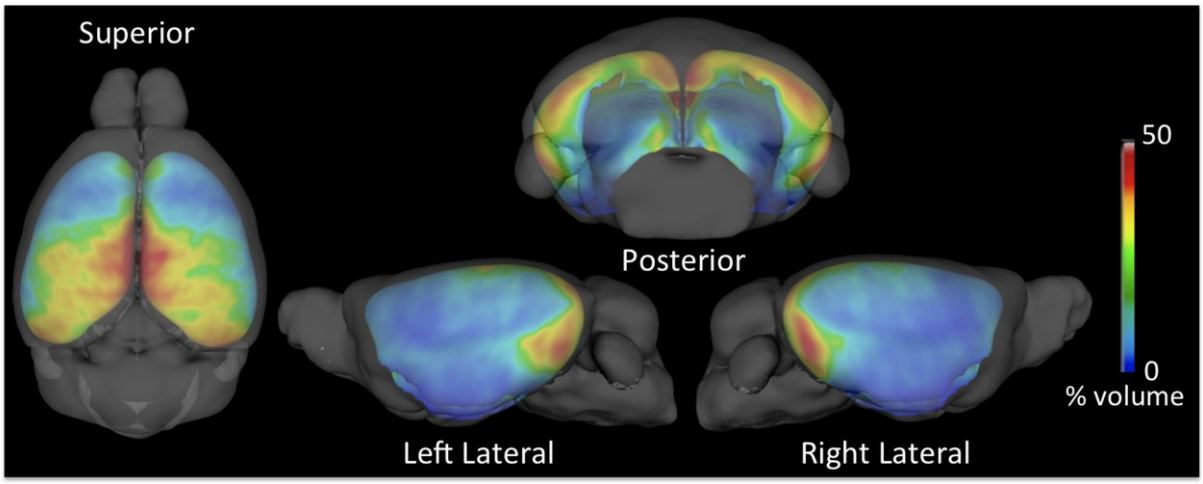

Figure 8 Representative views of the surface-projected β-amyloid qIHC data.

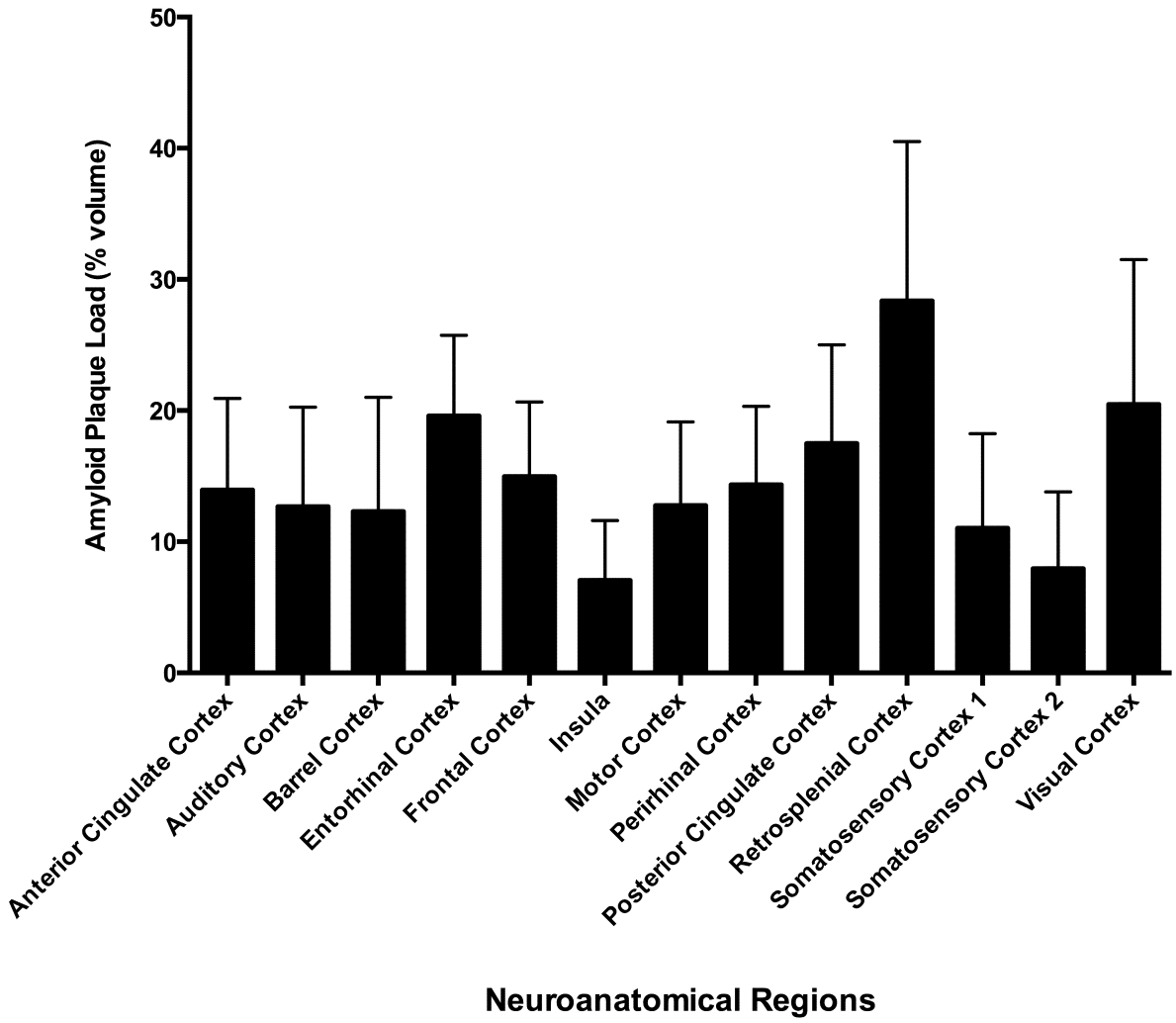

Figure 9 β-amyloid burden (% volume occupied) for each of the cortical ROIs. * indicates $p < 0.05$.

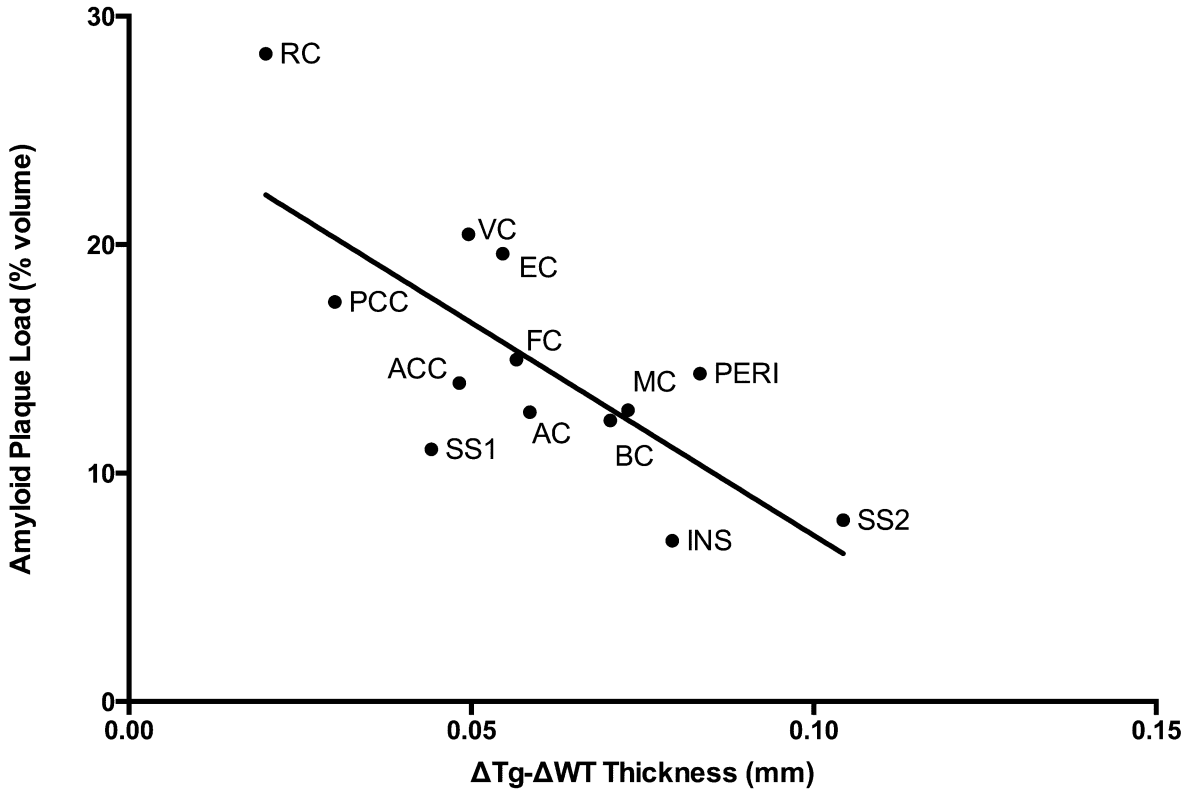

Figure 10 Regional β-amyloid burden plotted against regional differences between cortical thickness changes in Tg and WT mice (r = 0.75, p = 0.003).

.

Preface to Chapter 9

In the paper presented in Chapter 7, we used ASL MRI to assess CBF. However, the assessed changes were at the capillary/tissue level. In AD brains, amyloid peptides deposit on the walls of arteries and arterioles, known as CAA. Since arterial pathology is common in AD, we sought to investigate cerebrovascular alterations at the arterial level. The paper that follows has been submitted to *The Journal of Cerebral Blood Flow and Metabolism* and we are currently awaiting reviewer remarks. As such, the manuscript may not be published as presented here.

Contributions of Authors

The following manuscript is entitled *"Compromised arterial function in a mouse model of Alzheimer's disease"*. I, Marilyn Grand'Maison (MGM), am first author, with co-authors François Hébert (FH), Ming-Kai Ho (MKH), Edith Hamel (EH) and Barry J. Bedell (BJB). This project was supervised and funded by BJB. EH provided the necessary transgenic animals as a collaborator at the Montreal Neurological Institute. BJB wrote the MRI sequence employed for arterial image acquisition. MKH and I coordinated the project. FH, BJB, and I developed the image processing for the arterial images. I performed the statistical analysis. BJB and I wrote the manuscript, and BJB is the corresponding author

Chapter 9

Title: Compromised arterial function in a mouse model of Alzheimer's disease

Running Title: Arterial dysfunction in Alzheimer's disease mice

Authors: Marilyn Grand'Maison, B.Sc.[1], François Hébert, M.Sc.[1], Ming-Kai Ho, M.Sc.[1], Edith Hamel, Ph.D.[2], Barry J. Bedell, M.D., Ph.D.[1]

[1]Small Animal Imaging Lab, McConnell Brain Imaging Centre, and [2]Laboratory for Cerebrovascular Physiology, Department of Neurology & Neurosurgery, Montreal Neurological Institute, McGill University, Montreal, QC, Canada

Corresponding Author:

Barry J. Bedell, M.D., Ph.D.
Montreal Neurological Institute, McGill University
3801 University Street
Montreal, Quebec, H3A 2B4
Canada
Phone: 514-398-8804
E-mail: barry.bedell@mcgill.ca

Funding:

Canadian Institutes of Health Research (Operating Grants MOP-93795 and MOP-119456 to B.J.B.).

Abstract

Arterial spin labeling (ASL) perfusion magnetic resonance imaging (MRI) has demonstrated abnormal cerebral blood flow (CBF) in Alzheimer's disease (AD) patients and murine models of AD. It is well-recognized that cerebral arteries undergo microstructural changes in AD, including deposition of β–amyloid, *i.e.* cerebral amyloid angiopathy (CAA). While conventional ASL MRI is used to study cerebrovascular dynamics at the capillary/tissue level, it does not provide specific information about the cerebral arteries. In order to assess arterial dysfunction in a mouse model of AD, we have employed a novel, non-invasive, quantitative approach based on *in vivo* 3D MRI data. We identified statistically significant differences in arterial function between 19.5 month-old mutant human amyloid precursor protein (APP) transgenic and age-matched wild-type mice in the vascular supply to several regions, including the cingulate cortex, retrosplenial cortex, and parieto-temporal-occipital lobe. The arterial supply to these particular regions demonstrated extensive vascular β-amyloid deposits by immunohistochemistry (IHC). Significant genotype-related differences were not observed in the proximal, large cerebral arteries (*e.g.* internal carotid, basilar), indicating the existence of loco-regional alterations. The compromised, regional arterial function identified in this study warrants further investigation into the relationship between arterial physiology and AD-related, pathological cellular and molecular processes.

[198 words]

Keywords

Magnetic resonance imaging, Alzheimer's disease, arterial dysfunction, transgenic mouse model, amyloid precursor protein

Introduction

Compromised cerebrovascular function is recognized as an important process in the pathophysiology of Alzheimer's disease (AD)[1]. The advent of non-invasive imaging techniques, such as arterial spin labeling (ASL) perfusion magnetic resonance imaging (MRI), has facilitated the evaluation of vascular function in AD patients. Recently, regional cerebral hypoperfusion has been suggested to be an early imaging biomarker for AD[2] and large-scale, multi-center research studies using ASL MRI, such as ADNI-2, are currently underway. Cortical hypoperfusion has also been observed in mutant amyloid precursor protein (APP) transgenic mice by ASL MRI[3,4,5,6].

Imaging of cerebrovascular function, however, is still a field in its infancy. While ASL perfusion MRI provides information regarding cerebral blood flow (CBF) primarily at the capillary/tissue level, other parts of the vascular tree have been implicated in AD. Several groups have demonstrated abnormalities of the arterial tree using magnetic resonance angiography (MRA) studies of animal models of AD. Beckmann *et al.*[7] demonstrated morphological and architectural disturbances of the cerebral arteries in APP23 mice by corrosion casts, while El Tannir El Tayara *et al.*[8] identified arterial abnormalities by qualitative review of MR angiograms from APP/PS1 mice. Lemieux *et al.*[9] found decreased diameters of specific arteries on MR angiograms in cholesterol-fed rabbits with cortical β-amyloid accumulation. Weller *et al.*[10] have suggested that one route of β-amyloid clearance from the brain is along capillary and arterial perivascular pathways, and that

cerebral amyloid angiopathy (CAA) is associated with failure of perivascular elimination. Biochemical studies support this proposed route and have identified the presence of β-amyloid in the walls of middle cerebral and basilar arteries[11].

The interrogation of AD-related arterial dysfunction is facilitated by the study of transgenic (Tg) murine models with targeted expression of mutant APP genes. These mouse models recapitulate many of the cognitive and neuropathological features of AD, and high-resolution images from the brains of these mice can be obtained with dedicated, high-field, small animal MRI systems. The major advantages of MRI over other methods to study cerebrovascular function include: (1) non-invasive data acquisition allowing for longitudinal studies, (2) assessment of the entire vascular tree, rather than focal regions of the cortical surface, and (3) improved translatability to human studies.

In this work, we sought to examine the spatial pattern of arterial dysfunction in a well-established mouse model of AD by *in vivo* MRI. We have employed a novel, 3D whole brain MRI acquisition technique and fully-automated image processing/analysis methods to derive objective, quantitative, regional measures of arterial function. We have identified significant arterial dysfunction in several brain regions, including the posterior cingulate/retrosplenial cortex and hippocampus, which also show extensive vascular β-amyloid pathology by immunohistochemistry (IHC) studies in aged mice. We anticipate that the unique observations from this

neuroimaging study will provide further insights into the role of altered cerebrovascular function in the pathogenesis of AD.

Materials and Methods

Animals

Heterozygous transgenic mice with neuronal overexpression of the Swedish ($670/671_{KM\rightarrow NL}$) and Indiana ($717_{V\rightarrow F}$) mutations of human APP driven by the platelet-derived growth factor β (PDGF-β) promoter on a C57BL/6J background (line J20)[12,13] were used for these studies. This model has been well-characterized for amyloidosis[12], cognitive/behavioral impairments[14], and cerebrovascular dysfunction[13]. Aged Tg (19.4 ± 0.5 months; n = 14 [6 male, 8 female]) and WT mice (19.5 ± 0.6 months; n = 15 [9 male, 6 female]) were used for this study. Mice were housed under a 12-hour light:12-hour dark schedule, and fed standard laboratory chow and water *ad libitum*. Experiments were approved by the Animal Ethics Committee of the Montreal Neurological Institute and McGill University, and were conducted in accordance with the guidelines of the Canadian Council on Animal Care.

Physiological Studies

A cohort of Tg (n=5) and WT (n=5) animals underwent physiological studies in order to ensure that MRI observations were not a consequence of systemic differences between genotypes. The mice had a catheter line placed in the femoral artery to provide access for arterial blood sampling. Briefly, arterial cannulation was performed by resection of the skin of the thigh and exposure of the femoral artery. Under the operating microscope, the femoral artery was isolated and a catheter was inserted and secured using silk sutures.

During the entire procedure animals were monitored for rectal temperature and respiration (Small Animal Instruments Inc., Stony Brook, NY), as well as mean blood pressure (CODA™ Blood Pressure Monitor, Kent Scientific Corporation, Torrington, CT). During surgical preparation, anesthesia was maintained at 4% sevoflurane in medical air. Once the arterial line was established, the animals were allowed to stabilize for 15 minutes under 3% sevoflurane in medical air. The temperature was maintained at 37 ± 0.2°C using a feedback-regulated warming system (Small Animal Instruments Inc., Stony Brook, NY). The first blood sample was removed at this time point. Blood samples (one drop, ~30μL) were withdrawn from the arterial catheter and blood gasses were immediately measured using an i-STAT cartridge blood gas monitor (Abbott Laboratories, Mississauga, Canada). The arterial line was then cleared with warmed, heparinized saline in order to maintain the patency of the catheter, and anesthesia was continued. Blood samples were re-obtained 85 minutes later.

In Vivo MRI Acquisition

Mice were anesthetized with an induction dose of 4-5% sevoflurane and secured in an MRI-compatible bed. All MRI studies were performed under ~2.5-3% sevoflurane in medical air and animals were allowed to breathe spontaneously without mechanical ventilation. Respiration rate and body temperature was continuously monitored using an MR-compatible system (Small Animal Instruments Inc., Stony Brook, NY) and the temperature was maintained at 37 ±

0.2°C throughout the study using a feedback-regulated warming system (Small Animal Instruments Inc., Stony Brook, NY).

All MR images were obtained from a 7T Bruker Pharmascan system (Bruker Biospin, Ettlingen, Germany) using a 28-mm inner-diameter, quadrature volume resonator (RAPID MR International, Columbus, OH). 3D "arteriograms" were acquired with a novel approach which involved the acquisition of two, interleaved imaging volumes, specifically (1) a conventional 3D time-of-flight (TOF) ("bright blood") image volume, and (2) a "dark blood" image volume using the same acquisition parameters, but with suppression of the signal from inflowing blood achieved via saturation RF pulses. The pulse sequence utilized the following parameters: matrix size = 128×128×64, FOV = 1.8×1.8×0.9 cm, spatial resolution = 140×140×280 μm (L-R x S-I x A-P), excitation flip angle = 30°, TR = 60 ms, TE = 1.8 ms, 4 averaged bright/dark blood pairs, and acquisition time = 35 minutes.

MRI Processing

An unbiased, symmetric, customized template was generated from the bright blood scans from the entire study population using an iterative process[15,16]. Prior to template generation, each reconstructed image volume underwent brain masking and linear spatial normalization utilizing a 12-parameter affine transformation[17] to map individual images from native coordinate space to reference space. Briefly, the template generation process involved an iterative (coarse-to-fine resolution) estimation of the nonlinear transformation to match each MRI scan to the evolving average of the population. The final anatomical

template (population average) was generated with an isotropic voxel resolution of 0.06 mm (Figure 1). This customized template was parcellated into an atlas consisting of 10 ROIs using the Montreal Neurological Institute (MNI) DISPLAY software package (http://www.bic.mni.mcgill.ca/software). The specific ROIs consisted of: (1) basilar artery, (2) cingulate cortex, (3) entorhinal/perirhinal cortex, (4) frontal cortex, (5) hippocampus, (6) internal carotid artery, (7) lateral frontal lobe, (8) parieto-temporal occipital lobe, (9) piriform cortex, (10) pterygopalatine artery, and (11) retrosplenial cortex (Supplemental Figure 1).

The bright and dark blood images from each animal were spatially normalized to the anatomical template (reference space) via linear and nonlinear registration[15]. The percent difference between bright and dark blood scans was computed, yielding a measure (the "arterial index") proportional to arterial blood flow. This map was subsequently thresholded with a constant value across animals in order to minimize residual background (*i.e.* non-arterial) signal prior to ROI-based analysis. Representative views of the group-average (Tg + WT) arterial index map are shown in Figure 1. Note the excellent definition of the azygos pericallosal artery and its branches in the sagittal view. The penetrating cortical arteries can be readily visualized in the coronal view.

Immunohistochemistry

Mice were deeply anesthetized with urethane (1 g/kg) and exsanguinated via transcardiac perfusion with phosphate-buffered saline (PBS), followed by

transcardiac infusion of 50 mL of 10% neutral-buffered formalin. Following perfusion, the brains were extracted and immersion-fixed in 10% neutral-buffered formalin for 72 hours. The brains were dehydrated through graded ethanol and xylene, and infiltrated with paraffin wax. The whole brains were oriented and embedded in paraffin blocks. The tissue sections (5 μm thick) were cut onto positively-charged glass slides.

For IHC, the slides were manually de-paraffinized and re-hydrated, incubated in an 80% formic acid epitope-retrieval solution for 5 minutes, and washed twice in deionized H_2O. All IHC studies were performed at room temperature on a Lab Vision 360 Autostainer (Fisher Scientific, Toronto, ON, Canada). The slides were stained using the REVEAL Polyvalent HRP-AEC detection system (Spring Bioscience, Pleasanton, CA). Briefly, slides were incubated sequentially with hydrogen peroxide for 10 minutes to quench endogenous peroxidase, followed by 10 minutes in Protein Block, then 90 minutes in the 4G8 primary antibody (1:5000 dilution; Covance, Princeton, NJ). Primary antibody binding was amplified using Complement (20 minutes), HRP-Conjugate (30 minutes), and visualized using AEC Single Solution (10 minutes). All sections were counterstained with Acid Blue 129 (Sigma-Aldrich, St. Louis, MO) and mounted with aqueous mounting medium[18]. The IHC sections were digitized using a MIRAX Scan 150 whole slide scanner (Carl Zeiss, Toronto, ON, Canada). Immunostained sections were reviewed by a pathologist (B.J.B.).

Statistical Analysis

Two-tailed Student's t-test was employed to assess between-group differences (Tg vs. WT). The MRI ROI-based data was adjusted for multiple comparisons using the Bonferroni correction, and P-values less than 0.05 were considered significant. Statistical analysis was performed using Prism (GraphPad, La Jolla, CA).

Results

The physiological measurements are summarized in Table 1. No significant differences were observed between sevoflurane-anesthetized Tg and WT mice for any of these parameters.

The Tg mice demonstrated reduced arterial indices in several brain regions. Compromised function can be appreciated in the arteries supplying the hippocampus, as well as in the branches of the azygos pericallosal artery (Figure 2). The ROI-based analysis (Figure 3) revealed significant group differences in the cingulate cortex ($P_{corrected} = 0.005$), parieto-temporal-occipital lobe ($P_{corrected} = 0.014$), and retrosplenial cortex ($P_{corrected} = 0.001$). The significance in the frontal cortex ($P_{uncorrected} = 0.007$), lateral frontal lobe ($P_{uncorrected} = 0.011$), and hippocampus ($P_{uncorrected} = 0.01$) did not survive multiple comparisons. Significant group differences in the major arterial supply to the brain, namely the internal carotid and basilar arteries, were not observed. The pterygopalatine artery (PPA) is an extracerebral branch of the carotid artery, and, as such, was expected to serve as an appropriate control between genotypes given the presumably low predisposition for amyloid-related pathology. Although a slightly higher arterial index was noted in the PPA of the Tg mice, this difference was not significant.

The β-amyloid IHC staining demonstrated substantial vascular amyloid pathology in small arteries/arterioles throughout the brain. Extensive deposition was identified in the walls of the azygos pericallosal artery and its branches, as well as in the small arteries supplying the

hippocampus, while variable degrees of staining was observed in the arterial supply to other cortical regions (Figure 4). No staining was observed in the internal carotid, basilar, and pterygopalatine arteries. As such, there appeared to be a relationship between vessels with reduced arterial indices and heavy amyloid burden.

Discussion

In this study, we have explored the spatial pattern of arterial function in APP Tg and age-matched WT mice using a novel, non-invasive, MRI-based approach. The most significant dysfunction was observed in the regions supplied by the azygos pericallosal artery, including the cingulate and retrosplenial cortical regions. These regions are amongst the first brain regions to demonstrate β-amyloid deposits in this mouse model. The posterior cingulate cortex has been shown to demonstrate glucose hypometabolism in Tg APP mice[19, 20, 21], as well as hypometabolism/hypoperfusion in human AD studie[22,23]. Given that the major cerebral arteries (*e.g.* internal carotid, middle cerebral) and the physiological measurements did not demonstrate any significant differences between genotypes, our data supports the existence loco-regional (*i.e.* segmental) arterial abnormalities.

The observed compromised regional arterial function may be related to local concentrations of soluble and insoluble β-amyloid. Buckner *et al.*[24] found that amyloid deposition, identified by [11C]PIB PET imaging, correlated with atrophy and hypometabolism in parts of the default-mode network (DMN), which includes the posterior cingulate cortex. Bero *et al.*[25] have elegantly demonstrated, by *in vivo* microdialysis, that interstitial fluid (ISF) β-amyloid is related to synaptic activity and predicts region-specific plaque deposition in Tg2576 mice. The high intrinsic activity of the posterior

cingulate/retrosplenial regions[26] may support the early and progressive changes observed in this particular region in our study.

It has been well-documented that the cerebrovasculature undergoes a range of microstructural and functional changes in AD[1]. Christie *et al.*[27] identified an age-dependent disruption of smooth muscle cells in leptomeningeal vessels affected by β-amyloid, which interfered with the ability of the vessel to respond to vasodilators. Alterations in smooth muscle actin (SMA) and collagen I, III, and IV have been identified in arterioles from AD brains, which may potentially contribute to arterial dysfunction[28,29,30]. Tong *et al.*[13] demonstrated increased expression of nitrotyrosine, reflecting nitrosative/oxidative stress, in cerebral vessels in transgenic mouse brain tissue. In order to study AD-associated arterial dysfunction, Han *et al.*[31] utilized *in vivo* digital video microscopy of leptomeningeal vessels and demonstrated that soluble β-amyloid is a major contributor to age-dependent cerebrovascular dysfunction in Tg2576 mice. Our demonstration of regional alterations in arterial function in APP Tg mice further supports the importance of amyloid-related cerebrovascular dysfunction.

We observed an interesting, albeit non-statistically significant, trend of an increased arterial index in the pterygopalatine artery of the Tg group. The pterygopalatine artery is known to provide collateral supply to the rodent brain, including the cingulate/retrosplenial cortex[32,33]. This supply may increase in Tg mice where the primary local arterial flow is compromised as a function of β-amyloid induced vascular dysfunction.

Future studies could assess the impact of collateral circulation on regional cerebral blood flow/volume by occlusion of the source(s) of collateral supply.

A potential confounding factor in this study is the use of anesthesia during MRI scanning. Volatile anesthetic agents are vasodilators and increased CBF has been demonstrated in rats under isoflurane[34]. Lenz *et al.*[35] demonstrated that sevoflurane produces less cerebral blood flow (CBF) increase than isoflurane. Flores *et al.*[36] determined that sevoflurane is preferred for physiologic imaging in mice. Based on these previous studies and our own experience, we performed our studies under sevoflurane. MRI studies of the mouse cerebrovasculature have conventionally been performed under anesthesia and it remains unknown at this time if our observations are influenced by the anesthetic agent. While imaging of conscious animals may be advantageous for physiological studies, minimizing motion is a primary concern for these sensitive scans and is challenging in awake mice. Desai *et al.*[37] recently reported the feasibility of optogenetic fMRI studies in awake mice and Mizuma *et al.*[38] described PET studies in conscious mice. However, the use of a head-post for immobilization, as employed in these studies, is not practical for long-term studies and the requirements for customized surface RF coils may limit accurate assessment of the non-superficial parts of the arterial tree. Our group is currently investigating non-invasive methods for head restraint which will facilitate arterial imaging studies of conscious mice.

ASL MRI studies have revealed cerebral hypoperfusion in APP Tg mice[3,4,5,6] and [14C]FDG autoradiography studies have regional glucose hypometabolism in these mice[19,20,21]. However, the relationship between arterial dysfunction, tissue hypoperfusion, and local hypometabolism in AD remain poorly understood. Multi-modality studies which combine all three measures will provide a unique opportunity to interrogate the aberrant neurovascular function. Further, anatomical and functional brain imaging studies have identified an apparent dissociation between structural and cerebral perfusion measures in normal aging and AD[39,40]. Examination of the potential association between regional brain atrophy and arterial dysfunction may provide further insight into structural-functional relationships in AD.

The identification of robust biomarkers (*e.g.* imaging, fluid, cognitive) to identify the earliest stages of AD is an active area of research. The identification of compromised arterial/arteriolar function may serve as an indication of disease and the spatial pattern/extent of arterial tree involvement could provide staging/prognostic information. An essential future aspect of this work will be to understand the pathological changes underlying the functional changes in order to build confidence in this imaging measure as a reliable disease biomarker. We envision that the non-invasive methods employed in these animal studies can be readily translated to human investigations and routinely employed in clinical studies. Finally, while currently available drugs for the treatment of AD provide limited,

short-term, symptomatic effects, drug development pipelines are moving toward disease-modifying therapies which would slow, reverse, or prevent this devastating illness. The development of new therapeutic agents, which target AD-associated cerebrovascular disease, is a promising avenue for effective treatment of AD. The use of appropriate biomarkers should serve to accelerate this drug discovery and development process.

[3,033 words]

Supplementary Information

Supplementary information is available at the Journal of Cerebral Blood Flow & Metabolism website – www.nature.com/jcbfm

Acknowledgements

We are grateful to Dr. Alex Zijdenbos (Biospective Inc., Montreal, QC, Canada) for his contribution to the MR image processing. We thank Dr. Lennart Mucke and the Gladstone Institutes for use of the J20 APP mice. We also thank Antonio Aliaga and Kung-Yuan Lin for acquisition of the MRI data, and Rozica Bolavan and Qin Shao for preparation of the IHC sections.

Disclosure/conflict of interest

The authors declare no conflict of interest.

References

1) Nicolakakis N, Hamel E. Neurovascular function in Alzheimer's disease patients and experimental models. *J Cereb Blood Flow Metab* 2011; 31: 1354-1370.

2) Chao LL, Buckley ST, Kornak J, Schuff N, Madison C, Yaffe K *et al.* ASL perfusion MRI predicts cognitive decline and conversion from MC to dementia. *Alzheimer Dis Assoc Disord* 2010; 24: 19-27.

3) Weidensteiner C, Metzger F, Bruns A, Bohrmann B, Kuennecke B, von Kienlin M. Cortical hypoperfusion in the B6.PS2APP mouse model for Alzheimer's disease: comprehensive phenotyping of vascular and tissular parameters by MRI. *Magn Reson Med* 2009; 62: 35-45.

4) Massad CA, Amin SK, Hu L, Mei Y, Klann E, Pautler RG. Mitochondrial superoxide contributes to blood flow and axonal transport deficits in the Tg2576 mouse model of Alzheimer's disease. *PLoS ONE* 2010; 5: e10561.

5) Faure A, Verret L, Bozon B, El Tannir El Tayara N, Ly M, Kober F *et al.* Impaired neurogenesis, neuronal loss, and brain function deficits in the APPxPS1-Ki mouse model of Alzheimer's disease. *Neurobiol Aging* 2011; 32: 407-418.

6) Poisnel G, Hérard A-S, El Tannir El Tayara N, Bourrin E, Volk A, Kober F *et al.* Increased regional cerebral glucose uptake in an APP/PS1 model of Alzheimer's disease. *Neurobiol Aging* 2012; 33: 1995-2005.

7) Beckmann N, Schuler A, Mueggler T, Meyer EP, Widerhold KH, Staufenbiel M *et al*. Age-dependent cerebrovascular abnormalities and blood flow disturbances in APP23 mice modeling Alzheimer's disease. *J Neurosci* 2003; 23: 8453-8459.

8) El Tannir El Tayara N, Delatour B, Volk A, Dhenain M. Detection of vascular alterations by in vivo magnetic resonance angiography and histology in APP/PS1 mouse model of Alzheimer's disease. *Magn Reson Mater Phy* 2010; 23: 53-64.

9) Lemieux SK, Smith-Bell CA, Wells JR, Ezerioha NM, Carpenter JS, Sparks DL *et al*. Neurovascular changes measured by time-of-flight MR angiography in cholesterol-fed rabbits with cortical amyloid β-peptide accumulation. *J Magn Reson Imaging* 2010; 32: 306-314.

10) Weller RO, Subash M, Preston SD, Mazanti I, Carare RO. Perivascular drainage of amyloid-beta peptides from the brain and its failure in cerebral amyloid angiopathy and Alzheimer's disease. *Brain Pathol* 2008; 18: 253-266.

11) Shinkai Y, Yoshimura M, Ito Y, Odaka A, Suzuki N, Yanagisawa K *et al*. Amyloid beta-proteins 1-40 and 1-42(43) in the soluble fraction of extra- and intracranial blood vessels. *Ann Neurol* 1995; 38: 421-428.

12) Mucke L, Masliah E, Yu GQ, Mallory M, Rockenstein EM, Tatsuno G *et al*. High-level neuronal expression of Aβ1–42 in wild-type human amyloid protein precursor Tg mice: synaptotoxicity without plaque formation. *J Neurosci* 2000; 20: 4050–4058.

13) Tong X-K, Nicolakakis N, Kocharyan A, Hamel E. Vascular remodeling versus amyloid β-induced oxidative stress in the cerebrovascular dysfunctions associated with Alzheimer's disease. *J Neurosci* 2005; 25: 11165-11174.

14) Palop JJ, Jones B, Kekonius L, Chin J, Yu GQ, Raber J *et al*. Neuronal depletion of calcium-dependent proteins in the dentate gyrus is tightly linked to Alzheimer's disease-related cognitive deficits. *Proc Natl Acad Sci USA* 2003; 100: 9572-9577.

15) Lau JC, Lerch JP, Sled JG, Henkelman RM, Evans AC, Bedell BJ. Longitudinal neuroanatomical changes determined by deformation-based morphometry in a mouse model of Alzheimer's disease. *Neuroimage* 2008; 42: 19-27.

16) Fonov V, Evans AC, Botteron K, Almli CR, McKinstry RC, Collins DL. Unbiased average age-appropriate atlases for pediatric studies. *Neuroimage* 2011; 54: 313-327.

17) Collins DL, Neelin P, Peters TM, Evans AC. Automatic 3D inter-subject registration of MR volumetric data in standardized Talairach Space. *J Comput Assist Tomogr* 1994; 18: 192-205.

18) Zehntner SP, Chakravarty MM, Bolovan RJ, Chan C, Bedell BJ. Synergistic tissue counterstaining and image segmentation techniques for accurate, quantitative immunohistochemistry. *J Histochem Cytochem* 2008; 56: 873-880.

19) Reiman EM, Uecker A, Gonzalez-Lima F, Minear D, Chen K, Callaway NL *et al*. Tracking Alzheimer's disease in transgenic mice using fluorodeoxyglucose autoradiography. *Neuroreport* 2000; 11: 987-991.

20) Valla J, Schneider L, Reiman EM. Age- and transgene-related changes in regional cerebral metabolism in PSAPP mice. *Brain Research* 2006; 1116: 194-200.

21) Nicholson RM, Kusne Y, Nowak LA, LaFerla FM, Reiman EM, Valla J. Regional cerebral glucose uptake in the 3xTG model of Alzheimer's disease highlights common regional vulnerability across AD mouse models. *Brain Research* 2010; 1347: 179-185.

22) Villain N, Fouquet M, Baron JC, Mezenge F, Landeau B, de La Sayette V *et al*. Sequential relationships between grey matter and white matter atrophy and brain metabolic abnormalities in early Alzheimer's disease. *Brain* 2010; 133: 3301-3314.

23) Alsop DC, Dai W, Grossman M, Detre JA. Arterial spin labeling blood flow MRI: its role in the early characterization of Alzheimer's disease. *J Alzheimer Dis* 2010; 20: 871-880.

24) Buckner RL, Snyder AZ, Shannon BJ, LaRossa G, Sachs R, Fotenos AF *et al*. Molecular, structural, and functional characterization of Alzheimer's disease: evidence for a relationship between default activity, amyloid, and memory. *J Neurosci* 2005; 25: 7709-7717.

25) Bero AW, Yan P, Roh JH, Cirrito JR, Stewart FR, Raichle ME *et al*. Neuronal activity regulates the regional vulnerability to amyloid-B deposition. *Nat Neurosci* 2011; 14: 750-756.

26) Buckner RL, Sepulcre J, Talukdar T, Krienen FM, Liu H, Hedden T *et al*. Cortical hubs revealed by intrinsic functional connectivity: mapping, assessment of stability, and relation to Alzheimer's disease. *J Neurosci* 2009; 29: 1860-1873.

27) Christie R, Yamada M, Moskowitz M, Hyman B. Structural and functional disruption of vascular smooth muscle cells in a transgenic mouse model of amyloid angiopathy. *Am J Path* 2001; 158: 1065-1071.

28) Tian J, Shi J, Smallman R, Iwatsubo T, Mann DM. Relationships in Alzheimer's disease between the extent of Abeta deposition in cerebral blood vessel walls, as cerebral amyloid angiopathy, and the amount of cerebrovascular smooth muscle cells and collagen. *Neuropathol Appl Neurobiol* 2006; 32: 332-340.

29) Christov A, Ottman J, Hamdheydari L, Grammas P. Structural changes in Alzheimer's disease brain microvessels. *Curr Alzheimer Res* 2008; 5: 392-395.

30) Stopa EG, Butala P, Salloway S, Johanson CE, Gonzalez L, Tavares R *et al*. Cerebral cortical arteriolar angiopathy, vascular beta-amyloid, smooth muscle actin, Braak stage, and *APOE* genotype. *Stroke* 2008; 39: 814-821.

31) Han BH, Zhou M-L, Abousaleh F, Brendza RP, Dietrich HH, Koenigsknecht-Talboo J *et al.* Cerebrovascular dysfunction in amyloid precursor protein transgenic mice: contribution of soluble and insoluble amyloid-B peptide, partial restoration via γ-secretase inhibition. *J Neurosci* 2008; 28: 13542-13550.

32) Chen Y, Ito A, Takai K, Saito N. Blocking pterygopalatine arterial blood flow decreases infarct volume variability in a mouse model of intraluminal suture middle cerebral artery occlusion. *J Neurosci Methods* 2008; 174: 18-24.

33) Popp A, Jaenisch N, Witte OW, Frahm C. Identification of ischemic regions in a rat model of stroke. *PLoS ONE* 2009; 4: e4764.

34) Sicard K, Shen Q, Brevard ME, Sullivan R, Ferris CF, King JA *et al*. Regional cerebral blood flow and BOLD responses in conscious and anesthestized rats under basal and hypercapnic conditions: implications for functional MRI studies. *J Cereb Blood Flow Metab* 2003; 23: 472-481.

35) Lenz C, Rebel A, van Ackern K, Kuschinsky W, Waschke KF. Local cerebral blood flow, local cerebral glucose utilization, and flow-metabolism coupling during sevoflurane versus isoflurane anesthesia in rats. *Anesthesiology* 1998; 89: 480-488.

36) Flores JE, McFarland LM, Vanderbilt A, Ogasawara AK, Williams S-P. The effects of anesthetic agent and carrier gas on blood glucose and tissue uptake in mice undergoing dynamic FDG-PET imaging: sevoflurane and isoflurane compared in air and in oxygen. *Mol Imaging Biol* 2008; 10: 192-200.

37) Desai M, Kahn I, Knoblich U, Bernstein J, Atallah H, Yang A *et al.* Mapping brain networks in awake mice using combined optical neural control and fMRI. *J Neurophysiol* 2010; 105: 1393-1405.

38) Mizuma H, Shukuri M, Hayashi T, Watanabe Y, Onoe H. Establishment of in vivo brain imaging method in conscious mice. *J Nucl Med* 2010; 51: 1068-1075.

39) Tosun D, Mojabi P, Weiner MW, Schuff N. Joint analysis of structural and perfusion MRI for cognitive assessment and classification of Alzheimer's disease and normal aging. *Neuroimage* 2010; 52: 186-197.

40) Chen JJ, Rosas HD, Salat DH. Age-associated reductions in cerebral blood flow are independent from regional atrophy. *Neuroimage* 2011; 55: 468-478.

Figures and Tables

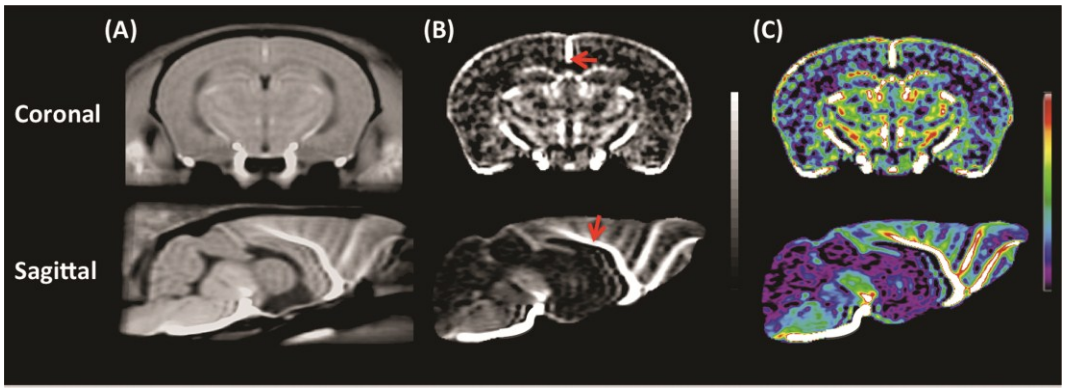

Figure 1 Representative coronal and sagittal views of the anatomical template and corresponding group-average (Tg + WT; n = 29) arterial index map (grayscale and color). The arrows in (B) identify the azygos pericallosal artery.

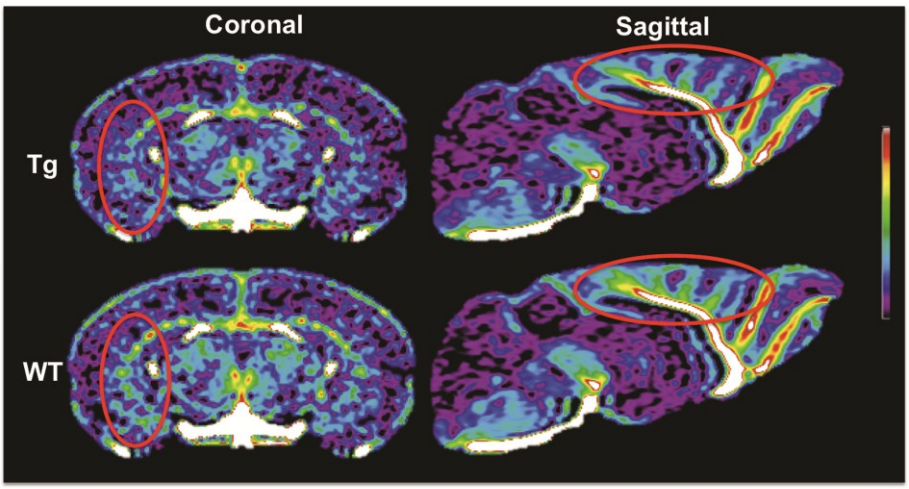

Figure 2 Representative coronal (left) and sagittal (right) views of group-average arterial index maps for Tg (n=14) and WT (n=15) mice. The red ellipses highlight regions with reduced arterial indices in the Tg mice.

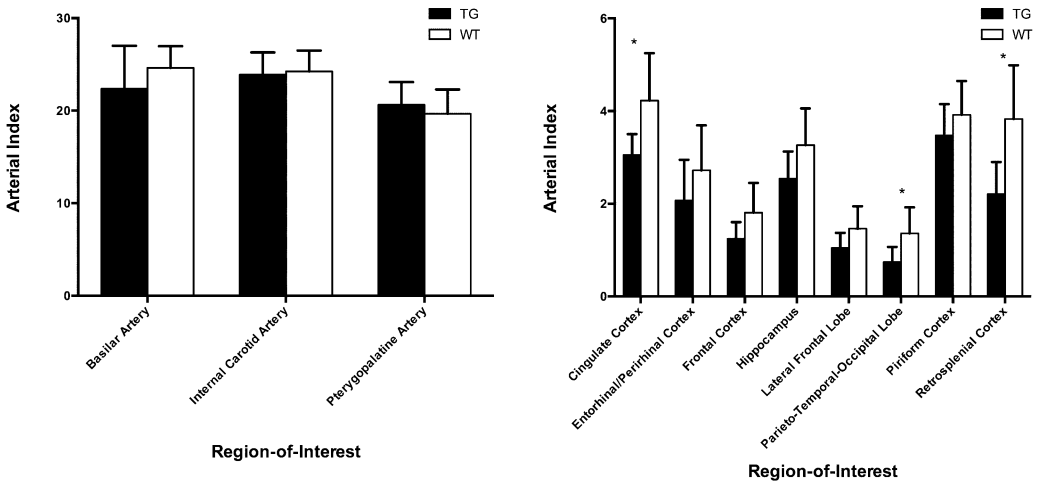

Figure 3 ROI-based arterial index measures from Tg and WT mouse groups.

* indicates $P < 0.05$.

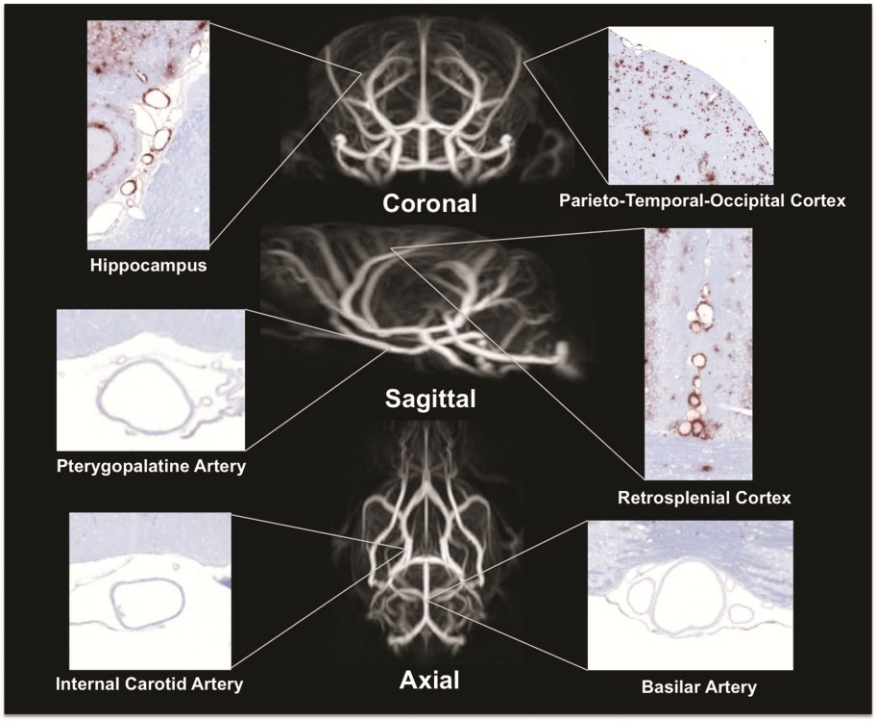

Figure 4 Maximum intensity projections (MIPs) of MRI data and β-amyloid IHC staining (insets) from representative ROIs.

	At 15 min				At 100 min			
Genotype	pH	pCO2	pO2	BP	pH	pCO2	pO2	BP
WT	7.35 ± 0.05	31.9 ± 3.3	92 ± 5	91 ± 6	7.32 ± 0.06	31.5 ± 2.0	91 ± 5	88 ± 4
Tg	7.38 ± 0.05	32.8 ± 3.8	90 ± 4	88 ± 9	7.35 ± 0.06	31.0 ± 2.0	90 ± 4	87 ± 9

Table 1 Summary of physiological measurement from Tg and WT mice. All values represent mean ± s.c. No significant differences were observed between groups.

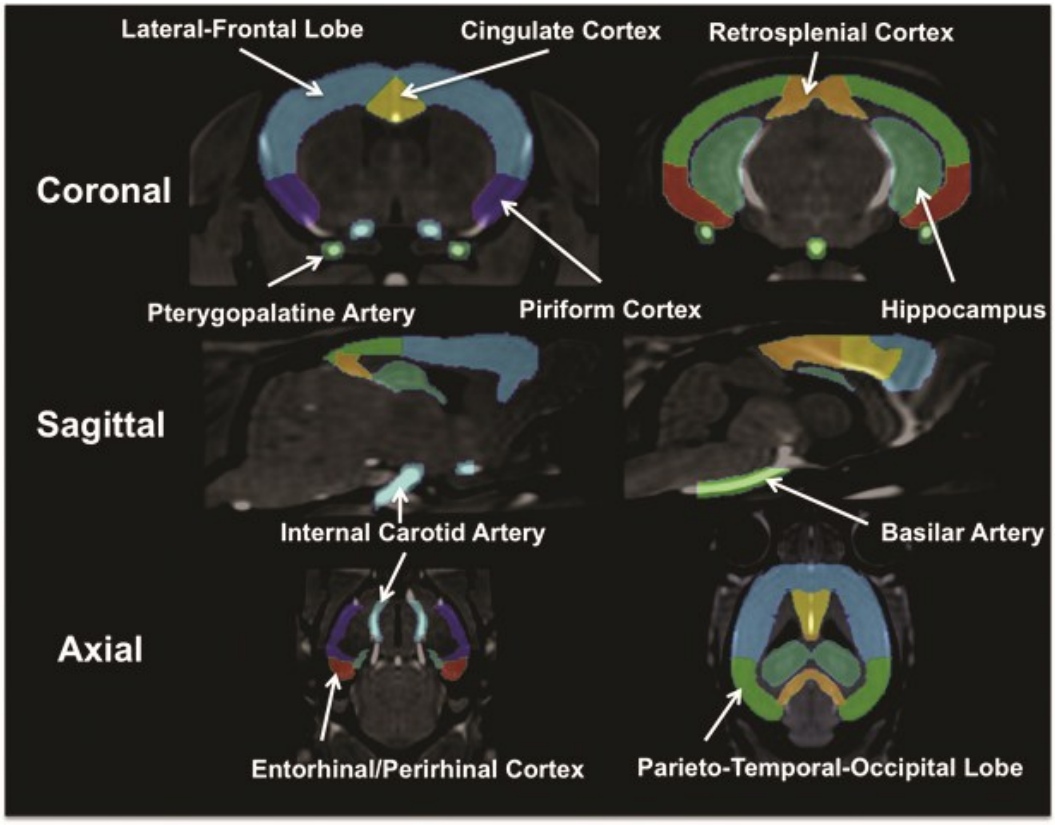

Supplementary Figure 1 Representative views of the atlas used for the ROI-based analysis

10. Conclusion

We have reported the first non-invasive *in vivo* structural and perfusion MRI study over the lifespan of a well-known AD mouse model. We identified heterogeneous, spatio-temporal patterns of cortical thickness and resting perfusion, suggesting asynchronous structural changes and cerebrovascular dysfunctions. Dissociation between cerebrovascular deficits and regional atrophy has been reported in AD patients (JJ Chen et al., 2011). The pathological processes underlying cognitive decline have been thought to follow a time-dependent transition of hemodynamic deficits and structural alterations. In the early stages of AD, regionally increased and reduced CBF can coexist along with characteristic cortical thinning, suggesting the independence of structural and perfusion changes (Dai et al., 2009; Dickerson et al., 2011).

Surprisingly, we found an increased cortical thickness in the young Tg mice. This observation was counterintuitive, given that a specific cortical thinning pattern has been reported in AD patients (Dickerson et al., 2009b; Dickerson et al., 2011). Nevertheless, previous studies suggest potential mechanisms to explain this finding. Neuronal hypertrophy may act as an early compensatory mechanism against AD-related, disturbed cellular events. Increased cortical and hippocampal neuron size has been described in cognitively-normal, amyloid-positive subjects relative to MCI and AD patients (Riudavets et al., 2007; Iacono et al., 2009). In addition, hypertrophic neurons have been observed in both APP_{Swe} and APP_{WT} mouse models (Oh et al., 2009). Alternatively, APP fragments are known to have a neuroprotective effect and trigger neuronal proliferation (Caillé et al., 2004; Chen and Tang, 2006). Furthermore, reactive astrocytes are common in AD and, as such, might be a contributing factor to the increased cortical thickness (Rodriguez et al., 2009; Steele and Robinson, 2012).

We identified a profound hypoperfusion in our Tg mouse model, corroborating data from previous studies (Weidensteiner et al., 2009; Massaad et al., 2010; Faure et al., 2011). However, by monitoring the perfusion over the mouse lifespan, we found a regional cortical CBF increase. Evidence of vascular remodeling has been reported in AD patients, and increased perfusion may be attributable to long-term angiogenesis (Desai et al., 2009).

As such, we have reported novel insights into the spatio-temporal patterns of structural and perfusion changes. Our findings raised questions about the underlying cellular mechanisms of the pathology. Further investigations are necessary to untangle the role of the different pathophysiological constituents. The generation of 3D parametric maps of cellular markers would provide additional and complementary information resulting of these biological processes. Mapping the spatio-temporal patterns of neuronal, astrocytic, and synaptic density would improve our understanding of the regional cortical thickness changes. Furthermore, we could investigate the microscopic events leading to perfusion change by generating vascular density parametric maps.

We next sought to assess the cortical structure at 1 month-of-age, and to follow the subsequent progression in early life. We found that the cortical thickness pattern was different in Tg animals at 1 month-of-age relative to 3 months-old mice. At 1 month-of-age, the regional cortical thickness in our Tg mouse model was thinner or similar to WT. Then, cortical thickness underwent regional increase in the Tg group, while a general cortical thinning was observed in the WT group. The net effect was a thicker cortex in the Tg mice compared to WT mice at 3 months-of-age. The generation of neuronal, astrocytic, and synaptic parametric maps would also provide more complete information about cellular events related to early cortical thickness changes.

We found that the amyloid deposition pattern in this AD mouse model followed an anterior-to-posterior gradient. The highest level of plaque deposits was found in the posterior cingulate/retrosplenial cortex, entorhinal cortex, and hippocampus. Additionally, we identified a strong association between aberrant cortical thickness change at young age and regional amyloid plaque burden later in life. Soluble β-amyloid peptide could be the factor associating these two parameters. The areas showing no substantial cortical thickness change over time between the two genotypes, namely the posterior cingulate, retrosplenial, and entorhinal cortices, are the ones with the highest amyloid burden and are core regions of the DMN. The sensory areas underwent the greater cortical thickness changes between the two genotypes and were associated with lower Aβ deposition. The apparent negative association between early thickness change and late Aβ measures may be explained by distinct temporal patterns. As such, we postulated that the DMN-associated regions experienced morphological changes prior to 1 month-of-age, and we, therefore, did not capture the complete process. Pairing between regional soluble amyloid concentration in the ISF and later plaque density has been demonstrated (Bero et al., 2011). Hence, high plaque burden associated with DMN regions suggests high soluble amyloid level early in life. Moreover, Bero *et al.* determined that early regional disruption of functional connectivity in APP/PS1 AD mouse model was predictive of later amyloid plaque deposition (Bero et al., 2012).

We proposed a possible relationship between the early cortical thickness changes and the amyloid deposition at old age. In a follow-up study, it would be challenging to investigate the possible protective effect of cognitive reserve. Tampellini *et al.* demonstrated that synaptic activity modulates amyloid secretion (Tampellini et al., 2010). They established that chemically-reduced synaptic activity has a detrimental effect on synaptic density and memory. Furthermore, Lerch *et al.* (Lerch et al., 2011) investigated the mechanism of mouse brain structural plasticity associated with learning.

After a specific maze training on five consecutive days, they reported a selective growth in the hippocampus using high-resolution, *post-mortem* MRI. Since the hippocampus is a well-known affected region in AD, it would be interesting to explore the possibility of cognitive rescue by learning-induced plasticity and evaluate the impact on amyloid deposition.

Finally, we explored neurovascular deficits at the arterial level. We observed compromised arterial function in our AD mouse model. The major supplying arteries did not appear to be affected, while the neuroanatomical territories supplied by smaller arteries showed clear arterial deficit. The regions presenting a reduced arterial index were also the areas with the highest CAA. This neurovascular dysfunction in old age may result from CAA-related vessel narrowing/obstruction combined with the vasoconstrictive effects of soluble amyloid (Beckman et al., 2003; Meyer et al., 2008; Han et al., 2008).

The association between arterial dysfunction and CAA was based on a qualitative analysis of the arterial deficit and CAA deposition patterns. The development of a segmentation algorithm for accurate quantification of vascular amyloid staining would allow for a strict quantitative comparison.

Furthermore, arterial impairment has been observed prior to amyloid deposition and may reflect the vasoactive effect of soluble amyloid peptide (Han et al., 2008). Investigations of the arterial deficit in young Tg mice could highlight the possible role of soluble amyloid before significant CAA burden. A longitudinal study could highlight the dynamics of the arterial dysfunction and detect subtle changes in the vasculature.

The work of this thesis provides the foundation for multi-parametric assessments of macroscale and microscale changes occurring during the neurodegenerative process in AD Tg mouse models. The non-invasive nature of MRI scanning provides substantial benefits for longitudinal studies investigating disease-modifying therapies. Moreover, we further improved the characterization of a well-established AD mouse model, validating it as a powerful tool to study potential therapeutic agents targeting amyloid-related dysfunction. Studying AD Tg mouse models by *in vivo* MRI constitutes a major advance for translating knowledge from pre-clinical to human studies. Early therapeutic interventions are necessary to delay the disease course and enhance the quality-of-life of demented patients and their caregivers. As such, a comprehensive understanding of the biological processes related to AD cognitive decline is critical for effective therapy.

11. References

ABRAHAM, C. R. 2011. Amyloid Beta Peptide and the Amyloid Cascade Hypothesis. *In:* KOWALL, A. E. B. A. N. W. (ed.) *The Handbook of Alzheimer's Disease and Other Dementias.* First ed. UK: Blackwell Publishing Ltd.

ALSOP, D. C. & DETRE, J. A. 1998. Multisection cerebral blood flow MR imaging with continuous arterial spin labeling. *Radiology,* 208**,** 410-6.

ALSOP, D. C., DETRE, J. A. & GROSSMAN, M. 2000. Assessment of cerebral blood flow in Alzheimer's disease by spin-labeled magnetic resonance imaging. *Ann Neurol,* 47**,** 93-100.

ALZHEIMER SOCIETY OF CANADA 2010. Rising Tide: The Impact of Dementia on Canadian Society. Toronto, Canada: The Alzheimer Society of Canada.

ATTWELL, D., BUCHAN, A. M., CHARPAK, S., LAURITZEN, M., MACVICAR, B. A., NEWMAN, E. A. 2010. Glial and neuronal control of brain blood flow. *Nature,* 468, 232-43.

BADEA, A., JOHNSON, G. A. & JANKOWSKY, J. L. 2010. Remote sites of structural atrophy predict later amyloid formation in a mouse model of Alzheimer's disease. *Neuroimage,* 50**,** 416-27.

BARCLAY, L., ZEMCOV, A., BLASS, J. P., MCDOWELL, F. 1984. Rates of decrease of cerebral blood flow in progressive dementias. *Neurology,* 34: 1555-60.

BATEMAN, G. A., LEVI, C. R., SCHOFIELD, P., WANG, Y., LOVETT, E. C. 2006. Quantitative measurement of cerebral haemodynamics in early vasclar dementia and Alzheimer's disease. *J Clin Neurosci,* 13, 563-8.

BECKMANN, N., SCHULER, A., MUEGGLER, T., MEYER, E. P., WIEDERHOLD, K. H., STAUFENBIEL, M. & KRUCKER, T. 2003. Age-dependent cerebrovascular abnormalities and blood flow disturbances in APP23 mice modeling Alzheimer's disease. *J Neurosci,* 23**,** 8453-9.

BELLIVEAU, J. W., ROSEN, B. R., KANTOR, H. L., RZEDZIAN, R. R., KENNEDY, D. N., MCKINSTRY, R. C., VEVEA, J. M., COHEN, M. S., PYKETT, I. L. & BRADY, T. J. 1990. Functional cerebral imaging by susceptibility-contrast NMR. *Magn Reson Med,* 14**,** 538-46.

BERO, A. W., BAUER, A. Q., STEWART, F. R., WHITE, B. R., CIRRITO, J. R., RAICHLE, M. E., CULVER, J. P. & HOLTZMAN, D. M. 2012. Bidirectional relationship between functional connectivity and amyloid-β deposition in mouse brain. *J Neurosci,* 32**,** 4334-40.

BERO, A. W., YAN, P., ROH, J. H., CIRRITO, J. R., STEWART, F. R., RAICHLE, M. E., LEE, J. M. & HOLTZMAN, D. M. 2011. Neuronal activity regulates the regional vulnerability to amyloid-β deposition. *Nat Neurosci,* 14**,** 750-6.

BLENNOW, K., DE LEON, M. J. & ZETTERBERG, H. 2006. Alzheimer's disease. *Lancet,* 368**,** 387-403.

BOHNEN, N. I., DJANG, D. S., HERHOLZ, K., ANZAI, Y. & MINOSHIMA, S. 2012. Effectiveness and safety of 18F-FDG PET in the evaluation of dementia: a review of the recent literature. *J Nucl Med,* 53**,** 59-71.

BORETIUS, S., MICHAELIS, T., TAMMER, R., ASHERY-PADAN, R., FRAHM, J. & STOYKOVA, A. 2009. In vivo MRI of altered brain anatomy and fiber connectivity in adult pax6 deficient mice. *Cereb Cortex,* 19**,** 2838-47.

BORG, J. & CHEREUL, E. 2008. Differential MRI patterns of brain atrophy in double or single transgenic mice for APP and/or SOD. *J Neurosci Res,* 86**,** 3275-84.

BRAAK, H. & BRAAK, E. 1991. Neuropathological stageing of Alzheimer-related changes. *Acta Neuropathol,* 82**,** 239-59.

BUCKNER, R. L., SNYDER, A. Z., SHANNON, B. J., LAROSSA, G., SACHS, R., FOTENOS, A. F., SHELINE, Y. I., KLUNK, W. E., MATHIS, C. A., MORRIS, J. C. & MINTUN, M. A. 2005. Molecular, structural, and functional characterization of Alzheimer's disease: evidence for a relationship between default activity, amyloid, and memory. *J Neurosci,* 25**,** 7709-17.

CAILLÉ, I., ALLINQUANT, B., DUPONT, E., BOUILLOT, C., LANGER, A., MÜLLER, U. & PROCHIANTZ, A. 2004. Soluble form of amyloid precursor protein regulates proliferation of progenitors in the adult subventricular zone. *Development,* 131**,** 2173-81.

CHAO, L. L., BUCKLEY, S. T., KORNAK, J., SCHUFF, N., MADISON, C., YAFFE, K., MILLER, B. L., KRAMER, J. H. & WEINER, M. W. 2010. ASL perfusion MRI predicts cognitive decline and conversion from MCI to dementia. *Alzheimer Dis Assoc Disord,* 24**,** 19-27.

CHEN, J. J., ROSAS, H. D. & SALAT, D. H. 2011. Age-associated reductions in cerebral blood flow are independent from regional atrophy. *Neuroimage,* 55**,** 468-78.

CHEN, Y. & TANG, B. L. 2006. The amyloid precursor protein and postnatal neurogenesis/neuroregeneration. *Biochem Biophys Res Commun,* 341**,** 1-5.

CHEN, Y., WOLK, D. A., REDDIN, J. S., KORCZYKOWSKI, M., MARTINEZ, P. M., MUSIEK, E. S., NEWBERG, A. B., JULIN, P., ARNOLD, S. E., GREENBERG, J. H. & DETRE, J. A. 2011b. Voxel-level comparison of arterial spin-labeled perfusion MRI and FDG-PET in Alzheimer disease. *Neurology,* 77**,** 1977-85.

CHILLON, J. M. & G. L. BAUMBACH. 2002. Autoregulation: arterial and intracranial pressure. *Cerebral Blood Flow and Metabolism.* Philadelphia (PA): Lippincott Williams & Wilkins.

CHRISTIE, R., KIMCHI, E., KAJDASZ, S., BACSKAI, B. & HYMAN, B. T. 2001. Multiphoton microscopy and amyloid angiopathy. *Amyloid,* 8 Suppl 1**,** 48-50.

CIPOLLA, M. J. 2009. The cerebral circulation. *Integrated systems physiology: from molecule to function.* First ed. San Rafael (CA): Morgan & Claypool Life Sciences.

CLASSEN, J. A. 2008. Alzheimer's disease: trade-off for increased survival with atherosclerosis? *Ann Neurol,* 64, 475.

CLASSEN, J. A. & R. ZHANG. 2011. Cerebral autoregulation in Alzheimer's disease. *J Cereb Blood Flow Metab,* 31, 1572-7.

DAI, W., LOPEZ, O. L., CARMICHAEL, O. T., BECKER, J. T., KULLER, L. H. & GACH, H. M. 2009. Mild cognitive impairment and alzheimer disease: patterns of altered cerebral blood flow at MR imaging. *Radiology,* 250**,** 856-66.

DASURI, K., ZHANG, L., KELLER, J. N. 2012. Oxidative stress, neurodegeneration, and the balance of protein degradation and protein synthesis. *Free Radic Biol Med,* pii: S0891-5849(12)01141-0.

DELACOURTE, A., DAVID, J. P., SERGEANT, N., BUÉE, L., WATTEZ, A., VERMERSCH, P., GHOZALI, F., FALLET-BIANCO, C., PASQUIER, F., LEBERT, F., PETIT, H. & DI MENZA, C. 1999. The biochemical pathway of neurofibrillary degeneration in aging and Alzheimer's disease. *Neurology,* 52**,** 1158-65.

DELATOUR, B., GUÉGAN, M., VOLK, A. & DHENAIN, M. 2006. In vivo MRI and histological evaluation of brain atrophy in APP/PS1 transgenic mice. *Neurobiol Aging,* 27**,** 835-47.

DESAI, B. S., SCHNEIDER, J. A., LI, J. L., CARVEY, P. M. & HENDEY, B. 2009. Evidence of angiogenic vessels in Alzheimer's disease. *J Neural Transm,* 116**,** 587-97.

DETRE, J. A., LEIGH, J. S., WILLIAMS, D. S. & KORETSKY, A. P. 1992. Perfusion imaging. *Magn Reson Med,* 23**,** 37-45.

DEUTSCH, G. & J. R. TWEEDY. 1987. Cerebral blood flow in severity-matched Alzheimer and multi-infarct patients. *Neurology,* 37, 431-8.

DICKERSON, B. C., BAKKOUR, A., SALAT, D. H., FECZKO, E., PACHECO, J., GREVE, D. N., GRODSTEIN, F., WRIGHT, C. I., BLACKER, D., ROSAS, H. D., SPERLING, R. A., ATRI, A., GROWDON, J. H., HYMAN, B. T., MORRIS, J. C., FISCHL, B. & BUCKNER, R. L. 2009a. The cortical signature of Alzheimer's disease: regionally specific cortical thinning relates to symptom severity in very mild to mild AD dementia and is detectable in asymptomatic amyloid-positive individuals. *Cereb Cortex,* 19**,** 497-510.

DICKERSON, B. C., FECZKO, E., AUGUSTINACK, J. C., PACHECO, J., MORRIS, J. C., FISCHL, B. & BUCKNER, R. L. 2009b. Differential effects of aging and Alzheimer's disease on medial temporal lobe cortical thickness and surface area. *Neurobiol Aging,* 30**,** 432-40.

DICKERSON, B. C., STOUB, T. R., SHAH, R. C., SPERLING, R. A., KILLIANY, R. J., ALBERT, M. S., HYMAN, B. T., BLACKER, D. & DETOLEDO-MORRELL, L. 2011. Alzheimer-signature MRI biomarker predicts AD dementia in cognitively normal adults. *Neurology,* 76**,** 1395-402.

DODART, J. C., MATHIS, C., SAURA, J., BALES, K. R., PAUL, S. M. & UNGERER, A. 2000. Neuroanatomical abnormalities in behaviorally characterized APP(V717F) transgenic mice. *Neurobiol Dis,* 7**,** 71-85.

DU, A. T., JAHNG, G. H., HAYASAKA, S., KRAMER, J. H., ROSEN, H. J., GORNO-TEMPINI, M. L., RANKIN, K. P., MILLER, B. L., WEINER, M. W. & SCHUFF, N. 2006. Hypoperfusion in frontotemporal dementia and Alzheimer disease by arterial spin labeling MRI. *Neurology,* 67**,** 1215-20.

EDVINSSON, L., MACKENZIE, E., MCCULLOCH, J. 1993. *Cerebral blood flow and metabolism*. New York (NY): Raven Press.

EIKELENBOOM, P., VAN EXEL, E., VEERHUIS, R., ROZEMULLER, A. J., VAN GOOL, W. A. & HOOZEMANS, J. J. 2012. Innate immunity and the etiology of late-onset Alzheimer's disease. *Neurodegener Dis,* 10**,** 271-3.

EL TAYARA, N. L. T., DELATOUR, B., VOLK, A. & DHENAIN, M. 2010. Detection of vascular alterations by in vivo magnetic resonance angiography and histology in APP/PS1 mouse model of Alzheimer's disease. *MAGMA,* 23**,** 53-64.

ELWELL, C. E., COPE, M., EDWARDS, A. D., WYATT, J. S., DELPY, D. T., REYNOLDS, E. O. 1994, Quantification of adult cerebral hemodynamics by near-infrared spectroscopy. *J Appl Physiol,* 77, 2753-60.

FARKAS, E. & LUITEN, P. G. 2001. Cerebral microvascular pathology in aging and Alzheimer's disease. *Prog Neurobiol,* 64**,** 575-611.

FAURE, A., VERRET, L., BOZON, B., EL TANNIR EL TAYARA, N., LY, M., KOBER, F., DHENAIN, M., RAMPON, C. & DELATOUR, B. 2011. Impaired neurogenesis, neuronal loss, and brain functional deficits in the APPxPS1-Ki mouse model of Alzheimer's disease. *Neurobiol Aging,* 32**,** 407-18.

GOADSBY, P. J. & L. EDVINSSON. 2002. *Neurovascular control of the cerebral circulation.* Philadelphia (PA): Lippincott Williams & Wilkins.

GOATE, A. & HARDY, J. 2012. Twenty years of Alzheimer's disease-causing mutations. *J Neurochem,* 120 Suppl 1**,** 3-8.

GOLDE, T. E. 2003. Alzheimer disease therapy: can the amyloid cascade be halted? *J Clin Invest,* 111**,** 11-8.

GONZALEZ-LIMA, F., BERNDT, J. D., VALLA, J. E., GAMES, D. & REIMAN, E. M. 2001. Reduced corpus callosum, fornix and hippocampus in PDAPP transgenic mouse model of Alzheimer's disease. *Neuroreport,* 12**,** 2375-9.

GOURAS, G. K., TAMPELLINI, D., TAKAHASHI, R. H. & CAPETILLO-ZARATE, E. 2010. Intraneuronal beta-amyloid accumulation and synapse pathology in Alzheimer's disease. *Acta Neuropathol,* 119**,** 523-41.

HALTERMAN, M., HOLLOWAY, R. G., JOZEFOWICK, R. F. & THOMPSON STONE, R. 2009. *Neuroimaging Laboratory* [Online]. Univerisity of Rochester Medical Center. [Accessed December 6, 2012].

HAN, B. H., ZHOU, M. L., ABOUSALEH, F., BRENDZA, R. P., DIETRICH, H. H., KOENIGSKNECHT-TALBOO, J., CIRRITO, J. R., MILNER, E., HOLTZMAN, D. M. & ZIPFEL, G. J. 2008. Cerebrovascular dysfunction in amyloid precursor protein transgenic mice: contribution of soluble and insoluble amyloid-beta peptide, partial restoration via gamma-secretase inhibition. *J Neurosci,* 28**,** 13542-50.

HARDY, J. A. & HIGGINS, G. A. 1992. Alzheimer's disease: the amyloid cascade hypothesis. *Science,* 256**,** 184-5.

HERHOLZ, K. 2011. Perfusion SPECT and FDG-PET. *Int Psychogeriatr,* Suppl 2, S25-31.

HIGGINS, G. A. & JACOBSEN, H. 2003. Transgenic mouse models of Alzheimer's disease: phenotype and application. *Behav Pharmacol,* 14**,** 419-38.

HOEDT-RASMUSSEN, K. 1965. Regional cerebral flow in man measured externally following intra-arterial adminstration of 85-Kr or 133-Xe dissolved in saline. *Acta Neurol Scand Suppl,* 14, 65-8.

HONG, S., QUINTERO-MONZON, O., OSTASZEWSKI, B. L., PODLISNY, D. R., CAVANAUGH, W. T., YANG, T., HOLTZMAN, D. M., CIRRITO, J. R. & SELKOE, D. J. 2011. Dynamic analysis of amyloid β-protein in behaving mice reveals opposing changes in ISF versus parenchymal Aβ during age-related plaque formation. *J Neurosci,* 31**,** 15861-9.

HOOIJMANS, C. R., RUTTERS, F., DEDEREN, P. J., GAMBAROTA, G., VELTIEN, A., VAN GROEN, T., BROERSEN, L. M., LÜTJOHANN, D., HEERSCHAP, A., TANILA, H. & KILIAAN, A. J. 2007. Changes in cerebral blood volume and amyloid pathology in aged Alzheimer APP/PS1 mice on a docosahexaenoic acid (DHA) diet or cholesterol enriched Typical Western Diet (TWD). *Neurobiol Dis,* 28**,** 16-29.

IACONO, D., MARKESBERY, W. R., GROSS, M., PLETNIKOVA, O., RUDOW, G., ZANDI, P. & TRONCOSO, J. C. 2009. The Nun study: clinically silent AD, neuronal hypertrophy, and linguistic skills in early life. *Neurology,* 73**,** 665-73.

IADECOLA, C. 2004. Neurovascular regulation in the normal brain and in Alzheimer's disease. *Nat Rev Neurosci,* 5**,** 347-60.

INGVAR, D. H. & N. A. LASSEN. 1965. Methods for cerebral blood flow measurements in man. *Br J Anaesth,* 37, 216-24.

JACOBS, A. H., DITTMAR, C., WINKELER, A., GARLIP, G., HEISS, W. D. 2002. Molecular imaging of gliomas. *Mol Imaging,* 1, 309-35.

JAGUST, W. J., HAAN, M. N., REED, B. R., EBERLING, J. L. 1998. Brain perfusion imaging predicts survival in Alzheimer's disease. *Neurology,* 51, 1009-13.

JOHNSON, K. A. & M. S. ALBERT. 2000. Perfusion abnormalities in prodomal AD. *Neurobiol Aging,* 21, 289-92.

JOHNSON, N. A., JAHNG, G. H., WEINER, M. W., MILLER, B. L., CHUI, H. C., JAGUST, W. J., GORNO-TEMPINI, M. L. & SCHUFF, N. 2005. Pattern of cerebral hypoperfusion in Alzheimer disease and mild cognitive impairment measured with arterial spin-labeling MR imaging: initial experience. *Radiology,* 234**,** 851-9.

JONES, T. 1996. The imaging science of positron emission tomography. *Eur J Nucl Med,* 23, 807-13.

JONES, T. & E. A. RABINER. 2012. The development, past achievements, and future directions of brain PET. *J Cereb Blood Flow Metab,* 32, 1426-54.

KALARIA, R. N. 2009. Neurodegenerative disease: Diabetes, microvascular pathology and Alzheimer disease. *Nat Rev Neurol,* 5, 305-6.

KARA, F., DONGEN, E. S., SCHLIEBS, R., BUCHEM, M. A., GROOT, H. J. & ALIA, A. 2012. Monitoring blood flow alterations in the Tg2576 mouse model of Alzheimer's disease by in vivo magnetic resonance angiography at 17.6 T. *Neuroimage,* 60**,** 958-66.

KARRAN, E., MERCKEN, M. & DE STROOPER, B. 2011. The amyloid cascade hypothesis for Alzheimer's disease: an appraisal for the development of therapeutics. *Nat Rev Drug Discov,* 10**,** 698-712.

KETY, S. S. & C. F. SCHMIDT. 1948. The nitrous oxide method for the quantitative determination of cerebral blood flow in man: theory, procedure and normal values. *J Clin Invest,* 27, 476-83.

KIM, J., BASAK, J. M. & HOLTZMAN, D. M. 2009. The role of apolipoprotein E in Alzheimer's disease. *Neuron,* 63**,** 287-303.

LANDAU, S. M., HARVEY, D., MADISON, C. M., KOEPPE, R. A., REIMAN, E. M., FOSTER, N. L., WEINER, M. W., JAGUST, W. J. & INITIATIVE, A. S. D. N. 2011. Associations between cognitive, functional, and FDG-PET measures of decline in AD and MCI. *Neurobiol Aging,* 32**,** 1207-18.

LASSEN, N. A. & O. MUNCK. 1955. The cerebral blood flow in man determined by the use of radioactive kryption. *Acta Physiol Scand,* 33, 30-49.

LASSEN, N. A. & D. H. INGVAR. 1961. The blood flow of the cerebral cortex determined by radioactive krypton. *Experientia,* 17, 42-3.

LASSEN, N. A., HOEDT-RASMUSSEN, K., SORENSEN, S. C., SKINHOJ, E., CRONQUIST, S., BODFORSS, B., INGVAR, D. H. 1963. Regional cerebral blood flow in man determined by krypton. *Neurology,* 13, 719-27.

LAU, J. C., LERCH, J. P., SLED, J. G., HENKELMAN, R. M., EVANS, A. C. & BEDELL, B. J. 2008. Longitudinal neuroanatomical changes determined by deformation-based morphometry in a mouse model of Alzheimer's disease. *Neuroimage,* 42**,** 19-27.

LERCH, J. P., PRUESSNER, J., ZIJDENBOS, A. P., COLLINS, D. L., TEIPEL, S. J., HAMPEL, H. & EVANS, A. C. 2008a. Automated cortical thickness measurements from MRI can accurately separate Alzheimer's patients from normal elderly controls. *Neurobiol Aging,* 29**,** 23-30.

LERCH, J. P., CARROLL, J. B., DORR, A., SPRING, S., EVANS, A. C., HAYDEN, M. R., SLED, J. G. & HENKELMAN, R. M. 2008b. Cortical thickness measured from MRI in the YAC128 mouse model of Huntington's disease. *Neuroimage,* 41**,** 243-51.

LERCH, J. P., YIU, A. P., MARTINEZ-CANABAL, A., PEKAR, T., BOHBOT, V. D., FRANKLAND, P. W., HENKELMAN, R. M., JOSSELYN, S. A. & SLED, J. G. 2011. Maze training in mice induces MRI-detectable brain shape changes specific to the type of learning. *Neuroimage,* 54**,** 2086-95.

LEUNER, K., MÜLLER, W. E., REICHERT, A. S. 2012. From mitochondrial dysfunction to amyloid beta formation: novel insights into the pathogenesis of Alzheimer's disease. *Mol Neurobiol,* 46, 186-93.

LIN, A. L., LAIRD, A. R., FOX, P. T. & GAO, J. H. 2012. Multimodal MRI neuroimaging biomarkers for cognitive normal adults, amnestic mild cognitive impairment, and Alzheimer's disease. *Neurol Res Int,* 2012**,** 907409.

LOPEZ, O. L. 2011. The growing burden of Alzheimer's disease. *Am J Manag Care,* 17 Suppl 13**,** S339-45.

MAGISTRETTI, P. J. & L. PELLERIN. 1996. Cellular mechanisms of brain metabolism. Relevance to functional brain imaging and to neurodegenerative disorders. *Ann N Y Acad Sci,* 777, 380-7.

MAHESWARAN, S., BARJAT, H., BATE, S. T., ALJABAR, P., HILL, D. L., TILLING, L., UPTON, N., JAMES, M. F., HAJNAL, J. V. & RUECKERT, D. 2009a. Analysis of serial magnetic resonance images of mouse brains using image registration. *Neuroimage,* 44**,** 692-700.

MAHESWARAN, S., BARJAT, H., RUECKERT, D., BATE, S. T., HOWLETT, D. R., TILLING, L., SMART, S. C., POHLMANN, A., RICHARDSON, J. C., HARTKENS, T., HILL, D. L., UPTON, N., HAJNAL, J. V. & JAMES, M. F. 2009b. Longitudinal regional brain volume changes quantified in normal aging and Alzheimer's APP x PS1 mice using MRI. *Brain Res,* 1270**,** 19-32.

MALLETT, B. L. & N. VEALL. 1963. Investigation of cerebral bloof-flow in hypertension, using radioactive-xenon inhalation and extracranial recording. *Lancet,* 1, 1081-2.

MASSAAD, C. A., AMIN, S. K., HU, L., MEI, Y., KLANN, E. & PAUTLER, R. G. 2010. Mitochondrial superoxide contributes to blood flow and axonal transport deficits in the Tg2576 mouse model of Alzheimer's disease. *PLoS One,* 5**,** e10561.

MASSOUD T. F. & S. S. GAMBHIR. 2007. Integrating noninvasive molecular imaging into molecular medicine: an evolving paradigm. *Trends Mol Med,* 13, 183-91.

MCHENRY, L. C. Jr. 1964. Quantitative cerebral blood flow determination. Application of a krypton 85 saturation technique in man. *Neurology,* 14, 785-93.

MEYER, E. P., ULMANN-SCHULER, A., STAUFENBIEL, M. & KRUCKER, T. 2008. Altered morphology and 3D architecture of brain vasculature in a mouse model for Alzheimer's disease. *Proc Natl Acad Sci U S A,* 105**,** 3587-92.

MORENO, H., WU, W. E., LEE, T., BRICKMAN, A., MAYEUX, R., BROWN, T. R. & SMALL, S. A. 2007. Imaging the Abeta-related neurotoxicity of Alzheimer disease. *Arch Neurol,* 64**,** 1467-77.

MORRIS, J. C., STORANDT, M., MCKEEL, D. W., RUBIN, E. H., PRICE, J. L., GRANT, E. A. & BERG, L. 1996. Cerebral amyloid deposition and diffuse plaques in "normal" aging: Evidence for presymptomatic and very mild Alzheimer's disease. *Neurology,* 46**,** 707-19.

MOSCONI, L. & MCHUGH, P. F. 2011. FDG- and amyloid-PET in Alzheimer's disease: is the whole greater than the sum of the parts? *Q J Nucl Med Mol Imaging,* 55**,** 250-64.

MUCKE, L., MASLIAH, E., YU, G. Q., MALLORY, M., ROCKENSTEIN, E. M., TATSUNO, G., HU, K., KHOLODENKO, D., JOHNSON-WOOD, K. & MCCONLOGUE, L. 2000. High-level neuronal expression of abeta 1-42 in wild-type human amyloid protein precursor transgenic mice: synaptotoxicity without plaque formation. *J Neurosci,* 20**,** 4050-8.

MUEGGLER, T., BAUMANN, D., RAUSCH, M., STAUFENBIEL, M. & RUDIN, M. 2003. Age-dependent impairment of somatosensory response in the amyloid precursor protein 23 transgenic mouse model of Alzheimer's disease. *J Neurosci,* 23**,** 8231-6.

MUEGGLER, T., STURCHLER-PIERRAT, C., BAUMANN, D., RAUSCH, M., STAUFENBIEL, M. & RUDIN, M. 2002. Compromised hemodynamic response in amyloid precursor protein transgenic mice. *J Neurosci,* 22**,** 7218-24.

NICOLAKAKIS, N. & HAMEL, E. 2011. Neurovascular function in Alzheimer's disease patients and experimental models. *J Cereb Blood Flow Metab,* 31**,** 1354-70.

NIWA, K., KAZAMA, K., YOUNKIN, S. G., CARLSON, G. A. & IADECOLA, C. 2002a. Alterations in cerebral blood flow and glucose utilization in mice overexpressing the amyloid precursor protein. *Neurobiol Dis,* 9**,** 61-8.

NIWA, K., KAZAMA, K., YOUNKIN, L., YOUNKIN, S. G., CARLSON, G. A. & IADECOLA, C. 2002b. Cerebrovascular autoregulation is profoundly impaired in mice overexpressing amyloid precursor protein. *Am J Physiol Heart Circ Physiol,* 283**,** H315-23.

OBERG, J., SPENGER, C., WANG, F. H., ANDERSSON, A., WESTMAN, E., SKOGLUND, P., SUNNEMARK, D., NORINDER, U., KLASON, T., WAHLUND, L. O. & LINDBERG, M. 2008. Age related changes in brain metabolites observed by 1H MRS in APP/PS1 mice. *Neurobiol Aging,* 29**,** 1423-33.

OBRIST, W. D., THOMPSON, H.K. Jr, WANG, H.S., WILKINSON, W.E. 1975. Regional cerebral blood flow estimated by 133-xenon inhalation. *Stroke,* 6, 245-56.

OH, E. S., SAVONENKO, A. V., KING, J. F., FANGMARK TUCKER, S. M., RUDOW, G. L., XU, G., BORCHELT, D. R. & TRONCOSO, J. C. 2009. Amyloid precursor protein increases cortical neuron size in transgenic mice. *Neurobiol Aging,* 30**,** 1238-44.

ONGALI, B., NICOLAKAKIS, N., LECRUX, C., ABOULKASSIM, T., ROSA-NETO, P., PAPADOPOULOS, P., TONG, X. K., HAMEL, E. 2010. Transgenic mice overexpressing APP and transforming growth factor-beta1 feature cognitive and vascular hallmarks of Alzheimer's disease. *Am J Pathol,* 177, 3071-80.

OWEN-REECE, H., ELWELL, C. E., HARKNESS, W., GOLDSTONE, J., DELPY, D. T., WYATT, J. S., SMITH, M. 1996. Use of near infrared spectroscopy to estimate cerebral blood flow in conscious and anaesthetized adult subjects. *Br J Anaesth,* 76, 43-8.

PACHAI, C., ZHU, Y. M., GUTTMANN, C. R. G., KIKINIS, R., JOLESZ, F. A., GIMENEZ, G., FROMENT, J.-C., CONFAVREUX, C. & WARFIELD, S. K. Unsupervised and Adaptive Segmentation of Multispectral 3D Magnetic Resonance Images of Human Brain: A Generic Approach. Medical Image Computing and Computer-Assisted Intervention, 2001 The Nederlands. 1067-1074.

PALOP, J. J., JONES, B., KEKONIUS, L., CHIN, J., YU, G. Q., RABER, J., MASLIAH, E. & MUCKE, L. 2003. Neuronal depletion of calcium-dependent proteins in the dentate gyrus is tightly linked to Alzheimer's disease-related cognitive deficits. *Proc Natl Acad Sci U S A,* 100**,** 9572-7.

PARIS, D., QUADROS, A., HUMPHREY, J., PATEL, N., CRESCENTINI, R., CRAWFORD, F. & MULLAN, M. 2004. Nilvadipine antagonizes both Abeta vasoactivity in isolated arteries, and the reduced cerebral blood flow in APPsw transgenic mice. *Brain Res,* 999**,** 53-61.

PETERSON, E. C., WANG, Z., BRITZ, G. 2011. Regulation of cerebral blood flow. *Int J Vasc Med,* doi: 10.1155/2011/823525.

PIERCE, E. C. Jr, LAMBERTSEN, C. J., DEUTSCH, S., CHASE, P. E., LINDE, H. W., DRIPPS, R. D., PRICE, H. L. 1962. Cerebral circulation and metabolism during thiopental anesthesia and hyper-ventilation in man. *J Clin Invest,* 41, 1664-71.

QUASTEL, J. H. & A. H. WHEATLEY. 1932. Oxidations by the brain. *Biochem J,* 26, 725-44.

QUERBES, O., AUBRY, F., PARIENTE, J., LOTTERIE, J. A., DÉMONET, J. F., DURET, V., PUEL, M., BERRY, I., FORT, J. C., CELSIS, P. & INITIATIVE, A. S. D. N. 2009. Early diagnosis of Alzheimer's disease using cortical thickness: impact of cognitive reserve. *Brain,* 132**,** 2036-47.

REDWINE, J. M., KOSOFSKY, B., JACOBS, R. E., GAMES, D., REILLY, J. F., MORRISON, J. H., YOUNG, W. G. & BLOOM, F. E. 2003. Dentate gyrus volume is reduced before onset of plaque formation in PDAPP mice: a magnetic resonance microscopy and stereologic analysis. *Proc Natl Acad Sci U S A,* 100**,** 1381-6.

RIUDAVETS, M. A., IACONO, D., RESNICK, S. M., O'BRIEN, R., ZONDERMAN, A. B., MARTIN, L. J., RUDOW, G., PLETNIKOVA, O. & TRONCOSO, J. C. 2007. Resistance to Alzheimer's pathology is associated with nuclear hypertrophy in neurons. *Neurobiol Aging,* 28**,** 1484-92.

RODRÍGUEZ, J. J., OLABARRIA, M., CHVATAL, A. & VERKHRATSKY, A. 2009. Astroglia in dementia and Alzheimer's disease. *Cell Death Differ,* 16**,** 378-85.

ROSEN, B. R., BELLIVEAU, J. W., VEVEA, J. M. & BRADY, T. J. 1990. Perfusion imaging with NMR contrast agents. *Magn Reson Med,* 14**,** 249-65.

ROTH, C. 2011. *Fundamentals of Body MRI: Expert Consult,* USA, Elsevier.

RUBIO-PEREZ J. M. & J. M. MORILLAS-RUIZ. 2012. A review: inflammatory process in Alzheimer’s disease, role of cytokines. *ScientificWorldJournal,* 2012, 756357.

SAWCHENKO, P. E. & RISSMAN, R. A. 2007. *A possible mechanistic link between stress and the development of Alzheimer tangles* [Online]. Salk institute for biological studies. [Accessed December 6, 2012].

SCHIDT, L. 1950. The influence of vitamin E on cardiovascular disorders. *Med World,* 72, 296-8.

SCHUFF, N. & X. P. ZHU. 2007. Imaging of mild cognitive impairment and early dementia. *Br J Radiol,* Spec No2, s109-14.

SHENG, M., SABATINI, B. L. & SÜDHOF, T. C. 2012. Synapses and Alzheimer's disease. *Cold Spring Harb Perspect Biol,* 4.

SHIN, H. K., JONES, P. B., GARCIA-ALLOZA, M., BORRELLI, L., GREENBERG, S. M., BACSKAI, B. J., FROSCH, M. P., HYMAN, B. T., MOSKOWITZ, M. A. & AYATA, C. 2007. Age-dependent cerebrovascular dysfunction in a transgenic mouse model of cerebral amyloid angiopathy. *Brain,* 130**,** 2310-9.

SHIN, J., KEPE, V., SMALL, G. W., PHELPS, M. E. & BARRIO, J. R. 2011. Multimodal Imaging of Alzheimer Pathophysiology in the Brain's Default Mode Network. *Int J Alzheimers Dis,* 2011**,** 687945.

STEELE, M. L. & ROBINSON, S. R. 2012. Reactive astrocytes give neurons less support: implications for Alzheimer's disease. *Neurobiol Aging,* 33**,** 423.e1-13.

SYMMS, M., JÄGER, H. R., SCHMIERER, K. & YOUSRY, T. A. 2004. A review of structural magnetic resonance neuroimaging. *J Neurol Neurosurg Psychiatry,* 75**,** 1235-44.

TACHIBANA, H., MEYER, J. S., OKAYASU, H., SHAW, T. G., KANDULA, O., ROGERS, R. L. 1984. Xenon contrast CT-CBF scanning of the brain differentiates normal age-related changes from multi-infarct dementia and senile dementia of Alzheimer type. *J Gerontol,* 39, 415-23.

TAMPELLINI, D., CAPETILLO-ZARATE, E., DUMONT, M., HUANG, Z., YU, F., LIN, M. T. & GOURAS, G. K. 2010. Effects of synaptic modulation on beta-amyloid, synaptophysin, and memory performance in Alzheimer's disease transgenic mice. *J Neurosci,* 30**,** 14299-304.

THAL, D. R., CAPETILLO-ZARATE, E., LARIONOV, S., STAUFENBIEL, M., ZURBRUEGG, S. & BECKMANN, N. 2009. Capillary cerebral amyloid angiopathy is associated with vessel occlusion and cerebral blood flow disturbances. *Neurobiol Aging,* 30**,** 1936-48.

THAL, D. R., GRIFFIN, W. S., DE VOS, R. A. & GHEBREMEDHIN, E. 2008. Cerebral amyloid angiopathy and its relationship to Alzheimer's disease. *Acta Neuropathol,* 115**,** 599-609.

TONG, X. K., NICOLAKAKIS, N., KOCHARYAN, A. & HAMEL, E. 2005. Vascular remodeling versus amyloid beta-induced oxidative stress in the cerebrovascular dysfunctions associated with Alzheimer's disease. *J Neurosci,* 25**,** 11165-74.

VAN BEEK, A. H., LAGRO, J., OLDE-RIKKERT, M. G., ZHANG, R., CLAASSEN, J. A. 2012. Oscillations in cerebral blood flow and cortical oxygenation in Alzheimer’s disease. *Neurobiol Aging,* 33, 428.

VAN BROECK, B., VANHOUTTE, G., CUIJT, I., PERESON, S., JORIS, G., TIMMERMANS, J. P., VAN DER LINDEN, A., VAN BROECKHOVEN, C. & KUMAR-SINGH, S. 2008a. Reduced brain volumes in mice expressing APP-Austrian mutation but not in mice expressing APP-Swedish-Austrian mutations. *Neurosci Lett,* 447**,** 143-7.

VAN BROECK, B., VANHOUTTE, G., PIRICI, D., VAN DAM, D., WILS, H., CUIJT, I., VENNEKENS, K., ZABIELSKI, M., MICHALIK, A., THEUNS, J., DE DEYN, P. P., VAN DER LINDEN, A., VAN BROECKHOVEN, C. & KUMAR-SINGH, S. 2008b. Intraneuronal amyloid beta and reduced brain volume in a novel APP T714I mouse model for Alzheimer's disease. *Neurobiol Aging,* 29**,** 241-52.

VAN DYCK, C. H., LIN, C. H., SMITH, E. O., WISNIEWSKI, G., CELLAR, J., ROBINSON, R., NARAYAN, M., BENNETT, A., DELANEY, R. C., BRONEN, R. A., HOFFER, P. B. 1996. Comparison of technetium-99m-HMPAO and technetium-99m-ECD cerebral SPECT images in Alzheimer's disease. *J. Nucl Med,* 37, 1749-55.

WAERZEGGERS, Y., MONFARED, P., VIEL, T., WINKELER, A. & JACOBS, A. H. 2010. Mouse models in neurological disorders: applications of non-invasive imaging. *Biochim Biophys Acta,* 1802**,** 819-39.

WEIDENSTEINER, C., METZGER, F., BRUNS, A., BOHRMANN, B., KUENNECKE, B. & VON KIENLIN, M. 2009. Cortical hypoperfusion in the B6.PS2APP mouse model for Alzheimer's disease: comprehensive phenotyping of vascular and tissular parameters by MRI. *Magn Reson Med,* 62**,** 35-45.

WEISS, C., VENKATASUBRAMANIAN, P. N., AGUADO, A. S., POWER, J. M., TOM, B. C., LI, L., CHEN, K. S., DISTERHOFT, J. F. & WYRWICZ, A. M. 2002. Impaired eyeblink conditioning and decreased hippocampal volume in PDAPP V717F mice. *Neurobiol Dis,* 11**,** 425-33.

WIMO, A. & PRINCE, M. 2012. World Alzheimer Report 2010, The Global Economic Impact of Dementia. London, UK: Alzheimer's Disease International.

WU, E. X., TANG, H., ASAI, T. & YAN, S. D. 2004. Regional cerebral blood volume reduction in transgenic mutant APP (V717F, K670N/M671L) mice. *Neurosci Lett,* 365**,** 223-7.

ZELLER, J. B., HERRMANN, M. J., EHLIS, A. C., POLAK, T., FALLGATTER, A. J. 2010. Altered parietal brain oxygenation in Alzheimer's disease as assessed with near-infrared spectroscopy. *Am J Geriatr Psychiatry,* 18, 433-41.

ZERBI, V., JANSEN, D., DEDEREN, P. J., VELTIEN, A., HAMANS, B., LIU, Y., HEERSCHAP, A. & KILIAAN, A. J. 2012. Microvascular cerebral blood volume changes in aging APP(swe)/PS1 (dE9) AD mouse model: a voxel-wise approach. *Brain Struct Funct*.

ZHANG, Y., SCHUFF, N., CHING, C., TOSUN, D., ZHAN, W., NEZAMZADEH, M., ROSEN, H. J., KRAMER, J. H., GORNO-TEMPINI, M. L., MILLER, B. L. & WEINER, M. W. 2011. Joint assessment of structural, perfusion, and diffusion MRI in Alzheimer's disease and frontotemporal dementia. *Int J Alzheimers Dis,* 2011**,** 546871.

ZLOKOVIC, B. V. 2011. Neurovascular pathways to neurodegeneration in Alzheimer's disease and other disorders. *Nat Rev Neurosci,* 12**,** 723-38.

Appendix

The signed waivers as well as the copies of research ethics certificates have been included with the initial submission.